KTH Engineering Sciences

Studies on Domain Wall Properties and Dynamics in $KTiOPO_4$ and Rb-doped $KTiOPO_4$

Gustav Lindgren

Doctoral Thesis in Physics

Laser Physics
Department of Applied Physics
School of Engineering Science
KTH

Stockholm, Sweden 2017

Studies on Domain Wall Properties and Dynamics in $KTiOPO_4$ and Rb-doped $KTiOPO_4$

© Gustav Lindgren, 2017

Laser Physics
Department of Applied Physics
KTH – Royal Institute of Technology
106 91 Stockholm
Sweden

ISBN: 978-91-7729-598-3
TRITA-FYS: 2017:71
ISSN: 0280-316X
ISRN: KTH/FYS/--17:71-SE

Akademisk avhandling som med tillstånd av Kungliga Tekniska Högskolan framlägges till offentlig granskning för avläggande av teknologie doktorsexamen i fysik, fredagen 08 december 2017 kl. 10:00 i sal FA31, Albanova, Roslagstullsbacken 21, KTH, Stockholm. Avhandlingen kommer att försvaras på engelska.

Cover picture: Selectively etched domain wall structure in Rb-$KTiOPO_4$.

Printed by Universitetsservice US AB, Stockholm 2017.

Gustav Lindgren
Studies on Domain Wall Properties and Dynamics in $KTiOPO_4$ and Rb-doped $KTiOPO_4$
Department of Applied Physics, KTH – Royal Institute of Technology
106 91 Stockholm, Sweden
ISBN: 978-91-7729-598-3, TRITA-FYS:2017:71, ISSN: 0280-316X, ISRN: KTH/FYS/--17:71-SE

Abstract

$KTiOPO_4$ (KTP) and Rb-doped KTP (RKTP) are two of the most attractive nonlinear optical materials for engineering of periodically poled domain structures, commonly used as frequency-conversion devices for laser radiation via the quasi-phase matching (QPM) technique. These materials have excellent non-linearity, wide transparency windows and high resistance to optical damage. Furthermore their large domain-velocity anisotropy allows the fabrication of high aspect-ratio domain structures, needed for many QPM applications. To create highly efficient devices, precise control over the structure uniformity and duty-cycle is required. Constant improvement of the domain engineering techniques has allowed pushing the limits of the achievable domain aspect-ratio. For this development to continue, a deeper understanding of the formation dynamics and stability of the domain gratings is of utmost importance. As the domain-size in nanostructured devices decreases, the density of the domains walls (DWs) increases and their properties are ever more important for device performance. Indeed, more knowledge on the domain wall properties, and the means to engineer them, could enable new applications exploiting these properties.

This thesis presents studies on domain wall properties and dynamics in KTP and RKTP. The sub-millisecond dynamics of grating formation in RKTP under an applied electric field has been studied in the high-field regime using online second harmonic generation. The effects of different pulse shapes were compared and single triangular pulses were found to be superior in terms of the resulting grating quality.

The high-temperature stability of domain gratings was investigated. The domain wall motion induced by annealing was shown to be highly anisotropic along the *a*- and *b*-crystal axes, and dependent on the period of the grating period.

The local charge transportation at the domains and domain walls in KTP was characterized using atomic force microscopy, demonstrating a fourfold increase of conductivity at the walls. Voltage-cycling measurements revealed memristive-like characteristics, attributed to the effect of ionic motion and local charge accumulation. The enhanced conductivity of charged domain walls was used as an imaging tool, to study domain wall dynamics while inducing motion through the application of an external field.

Finally, the interplay between ionic motion, spontaneous polarization and polarization reversal was investigated, showing direct evidence of elastic modulus modification during local polarization switching.

Sammanfattning

I denna doktorsavhandling studeras domänväggarna i kaliumtitanylfosfat (KTiOPO4, KTP) och Rb-dopad KTP (RKTP). Dessa material är attraktiva för frekvenskonvertering av laserljus i periodiska domängitter, genom kvasi-fasanpassning (QPM). De har höga ickelinjäriteter, breda transparensintervall och höga skadetrösklar. Dessutom möjliggör deras anisotropa domänstruktur tillverkning av domängitter med korta perioder, även i relativt tjocka kristaller, vilket är en förutsättning för många tillämpningar. För att frekvenskonverteringens verkningsgrad ska vara hög krävs homogena domängitter med väldefinierade förhållanden mellan bredden på de inverterade och ickeinverterade domänerna. Detta medför tillverkningsproblem för gitter med korta perioder, som krävs för frekvenskonvertering till det blå och ultravioletta spektrat eller tillämpningar med motpropagerande ljus. Djupare förståelse av gittrens dynamik och stabilitet är nödvändig för att utvecklingen av mer avancerade domängitter, med kortare perioder och större aperturer ska kunna fortsätta.

När gittren blir allt tätare kommer domänväggarna att uppta en allt större andel av kristallen och deras egenskaper blir allt viktigare för provernas prestanda. Det har rentav föreslagits att domänväggarna själva skall kunna komma att användas som byggstenar i framtida nanoelektroniktillämpningar.

Här presenteras undersökningar av domänväggarnas stabilitet och dynamiska egenskaper i KTP och RKTP.

Genom att mäta den samtidiga frekvenskonverterade strålningens intensitet under polningsförloppet studerades domänutbredningen under höga elektriska fält. Med denna teknik visades det att domänutbretningen sker under en tidsrymd kortare än en millisekund. Effekten av att variera tidsprofilen och fältstyrkan på den elektriska pulsen utforskades. Resultaten visade att en solitär triangulär puls ger bäst gitterkvalitet.

Domänstabiliteten undersöktes vid höga temperaturer för ett flertal gitter med olika periodicitet och domänväggskvalitet. Det visades att stabiliteten är beroende av periodiciteten och väggarnas orientering relativt kristallaxlarna.

Med hjälp av konduktiv atomkraftsmikroskopi (AFM) utforskades domänväggarnas elektriska egenskaper; mätningarna visade att ledningsförmågan är fyra gånger högre vid väggarna än i de omkringliggande domänerna vilket är en konsekvens av lokal ansamling av kristalldefekter. Det demonstrerades, genom att mäta strömmen som funktion av en cykliskt varierande spänning, att KTP har memristiva egenskaper; resistiviteten avtar gradvis med ökande antal spänningscykler. Vidare undersöktes egenskaperna hos laddade domänväggar och det visades att de kan förflyttas med hjälp av en extern elektrisk spänning mellan AFM-spetsen och kristallen. Väggarnas rörelse visualiserades genom att samtidigt mäta konduktiviteten. Dessutom undersöktes ledningsförmågan och de dynamiska egenskaperna hos metastabila domänväggar.

Slutligen visades det att jondistributionen och jonledningen i KTPs ytskikt är polarisationsberoende och att materialets elasticitetsmodul kan kontrolleras genom en inducerad omförflyttning av kaliumjoner via ett externt elektriskt fält.

Preface

The research presented in this thesis has been performed in the Laser Physics group, at the Applied Physics department of the Royal Institute of Technology (KTH), in Stockholm from 2012 to 2017.

This work was funded by the Swedish Foundation for Strategic Research (SSF) and the Swedish Research Council (VR) through its Linnaeus Center of Excellence ADOPT.

Some of the work presented is the result of international collaborations: The investigation of high temperature stability of domain gratings was performed together with the Universite Grenoble Alpes and the CNRS Institute of Grenoble, France. The study of ionic migration during ferroelectric switching was the result of collaboration with the Center for Nanophase Materials Sciences at Oak Ridge National Laboratories, USA.

List of Publications

This thesis is based on the following journal articles:

I. **Lindgren**, **G**., Zukauskas, A., Pasiskevicius, V., Laurell, F., and Canalias, C. " Studies of sub-millisecond domain dynamics in periodically poled Rb-doped $KTiOPO_4$, using online in situ second harmonic generation ", Opt Express. 23, 20332 (2015).

II. **Lindgren, G.**, Peña, A., Zukauskas, A., Liljestrand, C. Menaert, B., Boulanger, B., and Canalias, C., "Thermal stability of ferroelectric domain gratings in Rb-doped KTP", Appl. Phys Lett. 107, 082906 (2015).

III. **Lindgren, G.** and Canalias, C., "Domain wall conductivity in $KTiOPO_4$ crystals", APL Mater. 5, 076108 (2017).

IV. **Lindgren, G.** and Canalias, C., "Conductive properties of charged domain walls in motion in $KTiOPO_4$", (Submitted)

V. **Lindgren, G.**, Canalias, C., Ievlev, A., Vasudevan, R., Ovchinnikova, O., Jesse, S., and Kalinin, S., "Direct evidence of ionic migration during local ferroelectric switching", (Manuscript)

Description of Author Contribution

My contributions to the original papers were the following:

Paper I

I performed the poling experiments together with the coauthors and participated in the discussions of the results and writing of the manuscript.

Paper II

I performed the annealing experiments and subsequent analysis together with the coauthors and participated in writing the manuscript.

Paper III

I performed the measurements and wrote the manuscript together with the coauthor.

Paper IV

I performed the measurements and wrote the manuscript together with the coauthor.

Paper V

I performed the AFM-based experiments together with the coauthors and participated in the subsequent analysis and writing of the manuscript.

Publications not Included in this Thesis

A. **Lindgren, G.**, Zukauskas, A., Pasiskevicius, V., Laurell, and Canalias, ., "Studies of Sub Millisecond Domain Dynamics in Rubidium Doped KTP, Using Real-Time In-Situ SHG", CLEO, San José, 2013

B. **Lindgren, G.**, Peña, A., Zukauskas, A., Liljestrand, C., Ménaert, B., Benoît, B., and Canalias, C., "Thermal stability of ferroelectric domain gratings in Rbdoped $KTiOPO_4$", Advanced Solid State Lasers, ASSL, Berlin, 2015

C. **Lindgren, G.** and Canalias, C., "Enhanced Domain Wall Conductivity and Memristivity in $KTiOPO_4$", IEEE, Darmstadt, 2016

D. **Lindgren, G.**, Peña, A., Zukauskas, A., Liljestrand, C., Ménaert, B., Benoît, B., and Canalias, C., "Thermal stability of ferroelectric domain gratings in Rbdoped $KTiOPO_4$", IEEE, Darmstadt, 2016

Acknowledgements

I have received a lot of help and support during these last years for which I am deeply grateful.
First of all I would like to thank my main supervisor Prof. Carlota Canalias for accepting me as a PhD student and for all the advice and assistance she has given me throughout this time. I have learnt a lot from her and had a lot of fun during the process.
I would also like to thank Prof. Fredrik Laurell and Prof. Valdas Pasiskevicius for accepting me into the Laser Physics Group and for their help and guidance.
I am grateful to my colleagues, Andrius Zukauskas and Charlotte Liljestrand; and to my international collaborators, Benoît Boulanger, Anton Ievlev, Stephen Jesse, Sergei Kalinin, Bertrand Ménaert, Olga Ovchinnikova, Alexandra Peña and Rama Vasudevan for fruitful collaborations.
To all my colleagues in the Laser Physics Group, present and former, I would like to express my gratitude. They have always helped me when I have needed it and have made this a fun and inspiring place to work.
Finally, work is not all there is to life; I am also deeply grateful to my family and friends for the support I have received throughout this endeavor.

1. Introduction

Since the invention of the laser in 1960 [1], the coherent, intense radiation from laser sources has found applications in almost every field of modern technology. Lasers are used in everything from consumer electronics, telecommunications, and information technology, to medicine, materials processing and spectroscopy. Most laser applications require a specific wavelength and spectral properties for optimal performance. However, not all wavelength regions of interest are directly accessible by lasers. Using nonlinear optics [2], the radiation from existing lasers can be frequency converted, extending the available spectral range, providing wavelength tunability and adding the capability of spectral management. In order for the conversion to be efficient, the relative phase between the fundamental and generated radiation must be constant. This is the case if the refractive indices of the interacting waves are equal, which can commonly be achieved in a birefringent material through the proper choice of beam polarization. Efficient conversion can also be achieved using the quasi phase matching (QPM) technique, that has been gaining prominence since the first demonstration of periodic domain reversal in a bulk ferroelectric, using electric field poling [3]. In the QPM scheme, the phase-mismatch is compensated by micro structuring the nonlinear medium; through a periodic inversion of the sign of the nonlinear susceptibility, the accumulated phase error is reset and high conversion efficiency is ensured. QPM has many advantages: the polarization of the interacting beams can be chosen in a way that corresponds to the highest nonlinear coefficient; the phase-matching can be tailored for use over an extensive wavelength range, eliminating the need to develop different materials for different applications; and finally it has the capacity to compensate the large phase-mismatches associated with interactions between counter-propagating waves [4]. However, efficient QPM requires periodic gratings with typical periodicities on the micrometer level over crystal thicknesses in the millimeter range. In some cases even shorter periods and thicker samples are required. This can be very challenging from an engineering perspective. Several techniques have been developed for creating QPM gratings such as electron-beam writing [5], chemical patterning in ferroelectrics [6], and orientation-patterning of semiconductors [7]. Nevertheless, electric field poling of ferroelectrics remains the most commonly used technique. It was first demonstrated in lithium niobate [3] which, together with the isomorphic lithium tantalate, is still the most widely used ferroelectric for QPM applications. However, other materials with superior properties for some applications have also been exploited extensively. One of the most attractive alternatives is the $KTiOPO_4$ (KTP) family of crystals. Their potential for nonlinear optical applications was discovered in the 1970's [8] and periodically domain inverted waveguides were demonstrated in 1990 [6]. Periodic poling of bulk KTP was first reported in 1993 [5] using electron-beam writing. Electric field poling was first demonstrated in 1994 [9] and has, since then, been the most used fabrication method. Recently an alternative technique, template growth of periodic KTP using a poled substrate, was reported [10].

KTP and its isomorphs offer several advantages. Firstly they have superior resistance to optical damage and excellent thermal and mechanical properties. Secondly they have a wide transparency range, from 360 to 4000 nm in the case of KTP and further into both the UV and

the IR in case of some of the isomorphs [11]. Thirdly, their lower coercive field allows the fabrication of large aperture devices. Finally, and perhaps most importantly, their crystal structure is particularly suitable for periodic poling of fine-pitch gratings: As opposed to lithium niobate and its isomorphs, KTP has an orthorhombic crystal structure and highly anisotropic domain propagation. This favors the formation of one-dimensional domain gratings with high aspect-ratios that are ideal for many QPM applications. Even though periodic poling in KTP isomorphs is relatively well developed, it still suffers from several drawbacks. Due to less benevolent growth properties, these materials are relatively expensive and are only available in moderate wafer sizes. Furthermore, their high ionic conductivity poses problems for electric field poling, since the ionic current screens the applied electric field and causes difficulties in achieving homogeneous gratings, especially for high aspect-ratios. The conductivity also complicates monitoring the domain reversal as it masks the current resulting from the polarization switching. The issues associated with the high conductivity can be mitigated by partially substituting Rb for K, forming RKTP [12]. Substitution rates as low as 0.3 percent result in two orders of magnitude reduced conductivity and lower susceptibility to photochromic damage [13] without affecting the nonlinearity. Together, these properties make RKTP a very attractive choice for QPM applications, especially those requiring large apertures [14] and fine-pitch gratings [15]. Nevertheless, engineering of fine pitch gratings with good homogeneity over large crystal apertures remains a major challenge. In order to further develop the poling techniques to enable the creation of even high aspect-ratio gratings, further research is needed. In particular, deeper knowledge of the dynamics and stability of the domain gratings is crucial to release the full potential of these materials.

As the periodicity of the gratings decreases, the density of domain walls increases and the wall properties become ever more important for device performance. Furthermore, ferroelectric domain walls are an interesting field of study in their own right. At the walls, the symmetry of the parent material is broken, allowing the walls to have distinctive, symmetry-forbidden, properties such as otherwise absent nonlinear coefficients [16] or to present electric conductivity in otherwise insulating materials [17]. Because of this combination of distinct properties and confinement to extremely small volumes, domain walls have attracted a lot of attention from the ferroelectrics research community [18]. Increased conductivity at ferroelectric domain walls has been demonstrated in a range of materials [19]. However, the mechanism behind this seemingly ubiquitous increase of conductivity at the domain walls is not known; explanations involving both the bulk and the interface have been suggested and the research field is currently under constant development. KTP is a unique material in this context as it is both a ferroelectric and a superionic conductor. Furthermore, as previously mentioned, the conductivity can be engineered through doping of the material making it an ideal system for investigating the connection between domain wall conductive properties, ion mobility and polarization reversal. A deeper understanding of these phenomena will aid further development of domain engineering techniques; this is of great importance, not only for nonlinear optics, but for all fields in which ferroelectric domain engineering already plays a key role. Furthermore, if the unique properties

of the domain walls can be understood, they may be harnessed for future nanoscale devices in which the walls themselves would be the active elements.

The work presented in this thesis had three main aims: The first aim was to study the domain formation dynamics in KTP isomorphs. The second aim was to investigate the high temperature stability of the domain walls. Finally, the third aim was to characterize the properties of the domain walls and to investigate the interplay between ionic conductivity and polarization in KTP.

The thesis is organized in the following manner. Chapter 2 gives an overview of basic concepts of nonlinear optics. Chapter 3 introduces necessary concepts of ferroelectricity. Chapter 4 reviews the properties of KTP and RKTP. Chapter 5 describes the experimental techniques that were used in this work. Chapter 6 presents the investigations of polarization dynamics and high temperature grating stability. Chapter 7 presents the studies of domain wall properties. Finally chapter 8 is a concluding chapter summarizing the findings and outlining remaining challenges.

References to Chapter 1

[1] T. H. Maiman, "Stimulated Optical Radiation in Ruby", Nature, **187**, 493 (1960).

[2] P. A. Franken, A. E. Hill, C. W. Peters, and G. Weinreich, "Generation of optical harmonics," Phys. Rev. Lett. **7**, 118 (1961).

[3] M. Yamada, N. Nada, M. Saitoh, and K. Watanabe, "First-order quasi-phase matched LiNbO3 waveguide periodically poled by applying an external field for efficient blue second-harmonic generation," Appl. Phys. Lett. **62**, 435 (1993).

[4] C. Canalias and V. Pasiskevicius, "Mirrorless optical parametric oscillator," Nature Photonics **1**, 459 (2007).

[5] M. C. Gupta, W. P. Risk, A. C. G. Nutt, and S. D. Lau, " Domain inversion in KTiOPO4 using electron beam scanning," Appl. Phys. Lett. **63**, 1167 (1993).

[6] C. J. van der Poel, J.D. Bierlein, J.B. Brown and S. Colak, "Efficient type I blue second-harmonic generation in periodically segmented $KTiOPO_4$ waveguides", Appl. Phys. Lett. **57** 2074 (1990).

[7] K. L. Vodopyanov, O. Levi, P. S. Kuo, T. J. Pinguet, J. S. Harris, M. M. Fejer, B. Gerard, L. Becouarn, and E. Lallier, "Optical parametric oscillation in quasi-phase-matched GaAs", Opt. Lett. **29** (16), 1912 (2004).

[8] F. C. Zumsteg, J. D. Bierlein, and T. E. Gier, "$K_xRb_{1-x}TiOPO_4$: A new nonlinear optical material," J. Appl. Phys. **47**, 4980 (1976).

[9] Q. Chen and W. P. Risk, "Periodic Poling of $KTiOPO_4$ Using an Applied Electric Field", Electron Lett. **30**, 1516 (1994).

[10] A. Peña, B. Menaert, B. Boulanger, F. Laurell, C. Canalias, V. Pasiskevicius, P. Segonds, C. Felix, J. Debray, and S. Pairis, "Template-growth of periodically domain-structured KTiOPO4", Opt. Mater. Express, **1**, 185 (2011).

[11] G. Hansson, H. Karlsson, S. Wang, and F. Laurell, "Transmission measurements in KTP and isomorphic compounds," Appl. Opt. **39**, 5058 (2000).

[12] Q. Jiang., P. A. Thomas, K. B. Hutton, and R. C. C. Ward, "Rb-doped potassium titanyl phosphate for periodic ferroelectric domain inversion", Journal of Applied Physics **92**, 2717 (2002).

[13] S. Tjörnhammar, V. Maestroni, A. Zukauskas, T. Kristijonas Uzdavinys, C. Canalias, F. Laurell, and V. Pasiskevicius, "Infrared absorption in KTP isomorphs induced with blue picosecond pulses", Opt. Mater. Express **5**, 2951 (2015).

[14] A. Zukauskas, N. Thilmann, V. Pasiskevicius, F. Laurell, and C. Canalias, "5 mm thick periodically poled Rb-doped KTP for high energy optical parametric frequency conversion", Opt. Mater. Express **1**, 201 (2011).

[15] A. Zukauskas, C. Liljestrand, A. Viotti, V. Pasiskevicius, and C. Canalias, "Highly-Efficient Cascaded Mirrorless OPO in Sub-μm Periodically Poled RKTP Crystals," in Conference on Lasers and Electro-Optics, OSA Technical Digest (online) (Optical Society of America, 2017)

[16] A. Fragemann, V. Pasiskevicius, and F. Laurell, "Second-order nonlinearities in the domain walls of periodically poled $KTiOPO_4$**",** Appl. Phys. Lett. **85**, 375 (2004).

[17] M. Schröder, A. Haußmann, A. Thiessen, E. Soergel, T. Woike and L.M. Eng, "Conducting domain walls in lithium niobate single crystals", Adv. Funct. Mater. **22**, 3936 (2012).

[18] G. Catalan, J. Seidel, R. Ramesh, and J. F. Scott, "Domain wall nanoelectronics", Rev. Mod. Phys. **84**, 119 (2012).

[19] R. K. Vasudevan, W. Wu, J. R. Guest, A. P. Baddorf, A. N. Morozovska, E. A. Eliseev, N. Balke, V. Nagarajan, P. Maksymovych, and S. V. Kalinin, "Domain Wall Conduction and Polarization-Mediated Transport in Ferroelectrics", Adv. Funct. Mater. **23**, 2592 (2013).

2. Nonlinear Optics

2.1 Nonlinear Polarization

When an electromagnetic wave interacts with a dielectric material it induces polarization in the material. This polarization response can be written as a power series in the electric field (E-field),

$$P = P^L + P^{NL} = \epsilon_0 \chi^{(1)} E(t) + \epsilon_0 \chi^{(2)} E^2(t) + \cdots = P^{(1)} + P^{(2)} + \cdots, \quad (2.01)$$

where ϵ_0 is the vacuum permittivity and $\chi^{(n)}$ is the *n:*th order optical susceptibility. Since the effect of the magnetic field is much weaker, it can usually be omitted. At low intensities, all but the first term can be neglected and the induced polarization has a linear dependence on the electric field. However, for intense radiation higher order terms must be taken into account [1]. Depending on the material symmetry, the first nonzero nonlinear polarization coefficient can be due to either second order susceptibility, $\chi^{(2)}$ or the third order susceptibility, $\chi^{(3)}$. This can be seen by changing the sign of the electric field. Changing the direction of the field should also change the sign of the nonlinear response:

$$P^2(t) = \epsilon_0 \chi^{(2)} E^2(t) \quad (2.02)$$

$$-P^2(t) = \epsilon_0 \chi^{(2)} (-E(t))^2 = \epsilon_0 \chi^{(2)} E^2(t) \quad (2.03)$$

For a centrosymmetric medium, $\chi^{(2)}$ is independent of this sign change, since the material remains unchanged after a rotation by 180°. Therefore the second order susceptibility must vanish in this case, making the third order tensor the lowest non-zero susceptibility. In this thesis, only second order interactions in non-centrosymmetric materials are considered.

2.2 The Second Order Nonlinear Coefficient

The nonlinear susceptibilities $\chi^{(n)}, (n > 1)$ are tensor quantities since they depend on the orientation of the all interacting E-fields and of the nonlinear medium. For instance, the second order nonlinear susceptibility $\chi^{(2)}$, involves two interacting waves and is therefore a third-rank tensor with 27 elements. For practical reasons, the $\chi^{(2)}$ tensor is usually re-written as the nonlinearity tensor, *d*:

$$d_{ijk} = \frac{1}{2} \chi^{(2)}_{ijk}, \quad (2.04)$$

where the three indices i, j and k, refer to the orientation of the material and the two interacting electric fields respectively. Because of the symmetry properties of this tensor, the indices *j* and *k* are interchangeable, $d_{ijk} = d_{ikj}$ and the following contracted notation, where the indices *j* and *k* are substituted by a single index *l* is usually adopted.

Indices j, k :	Index l:
1,1	1
2,2	2
3,3	3
2,3; 3,2	4
3,1; 1,3	5
1,2; 2,1	6

Table 2.1: Indices of the nonlinear matrix

This way the nonlinear tensor d_{ijk} becomes the nonlinear matrix, d_{il}. If the wavelengths involved are sufficiently far below any absorption peaks of the material it can be approximated as lossless and Kleinman symmetry applies [1]. This substantially lowers the number of independent coefficients in the nonlinearity matrix from 18 to 10, and the nonlinear matrix becomes:

$$d_{il} = \begin{bmatrix} d_{11} & d_{12} & d_{13} & d_{14} & d_{15} & d_{16} \\ d_{16} & d_{22} & d_{23} & d_{24} & d_{14} & d_{12} \\ d_{15} & d_{24} & d_{33} & d_{23} & d_{13} & d_{14} \end{bmatrix} \tag{2.05}$$

By using this notation, the second order polarization can be written as,

$$\begin{bmatrix} P_x^{(2)}(\omega_3) \\ P_y^{(2)}(\omega_3) \\ P_z^{(2)}(\omega_3) \end{bmatrix} = 2\epsilon_0 K \begin{bmatrix} d_{11} & d_{12} & d_{13} & d_{14} & d_{15} & d_{16} \\ d_{16} & d_{22} & d_{23} & d_{24} & d_{14} & d_{12} \\ d_{15} & d_{24} & d_{33} & d_{23} & d_{13} & d_{14} \end{bmatrix} \begin{bmatrix} E_x(\omega_1)E_x(\omega_2) \\ E_y(\omega_1)E_y(\omega_2) \\ E_z(\omega_1)E_z(\omega_2) \\ E_y(\omega_1)E_z(\omega_2) + E_z(\omega_1)E_y(\omega_2) \\ E_x(\omega_1)E_z(\omega_2) + E_z(\omega_1)E_y(\omega_2) \\ E_x(\omega_1)E_y(\omega_2) + E_y(\omega_1)E_x(\omega_2) \end{bmatrix} \tag{2.06}$$

where K is a degeneracy factor that assumes the value $\frac{1}{2}$ for SHG and optical rectification and the value 1 for the other processes.

2.3 Second Order Nonlinear Processes

Consider the effect of the second order susceptibility, χ^2, on two fields at different frequencies ω_1 and ω_2. For simplicity the fields are approximated as monochromatic plane waves. This assumption allows the combined electric field to be written as:

$$E(t) = E_1 e^{-i\omega_1 t} + E_2 e^{-i\omega_2 t} + c.c., \tag{2.07}$$

where *c.c.* indicates the complex conjugate. Inserting this expression into the power series expansion for the nonlinear polarization gives the following expression for the second order term:

$$P^2(t) = \epsilon_0 \chi^{(2)}\big([E_1^2 e^{-2i\omega_1 t} + E_2^2 e^{-2i\omega_2 t} + 2E_1 E_2 e^{-i(\omega_1+\omega_2)t} + 2E_1 E_2^* e^{-i(\omega_1-\omega_2)t} + c.c.\big] + 2(E_1 E_1^* + E_2 E_2^*)\big) \tag{2.08}$$

The induced polarization has frequency components at the sum and difference of the input frequencies, as well as at frequencies corresponding to twice each input frequencies and a non-varying term. The different frequency components can be used to generate electromagnetic waves at the corresponding frequencies and are all used for different applications in nonlinear optics. The frequency independent term corresponds to a phenomenon known as *optical rectification,* corresponding to the creation of a quasi-static electric field across the crystal. An important special case of second order interactions is when one of the fields is static, i.e. $\omega_1 = 0$ *or* $\omega_2 = 0$. This static field can change the charge distribution in the medium, altering the refractive index experienced by the varying field, a phenomenon known as the *electro optic* or *Pockels* effect [2]. A schematic of processes involving the second order nonlinear susceptibility is shown in figure 2.1. These nonlinear processes are all *parametric*, i.e. the quantum state of the material remains unchanged, the total photon-energy is conserved and no net energy is transferred to the medium.

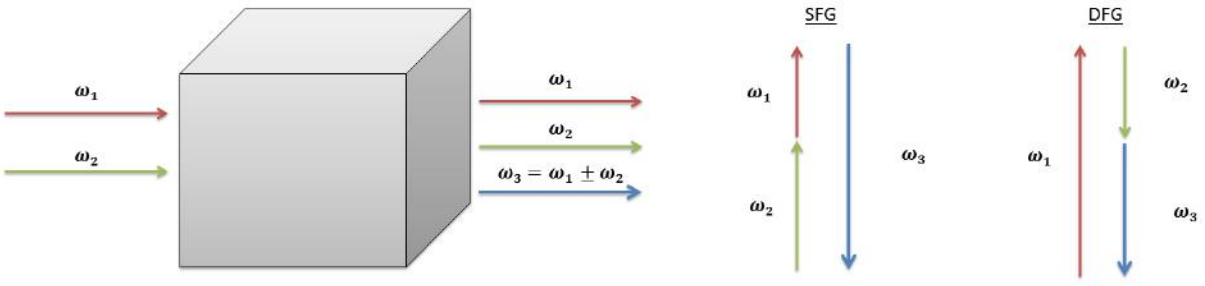

Figure 2.1: Illustration of nonlinear optical interactions involving the second order nonlinear susceptibility

The two schemes illustrated in figure 2.1 to generate radiation at the sum and difference of the waves ω_1 and ω_2 are known as *sum frequency generation* (SFG) and difference frequency generation (DFG). DFG is the basis of *optical parametric oscillation* (OPO) [3]. In an OPO, the nonlinear medium is placed in a cavity in which one or several of the waves resonate, allowing for the efficient generation of radiation. Since there is a wide range of wavelengths that can fulfill

the condition $\omega_1 = \omega_2 + \omega_3$, the output of the OPO can be tuned over this range by modifying the phase matching condition. OPOs have found widespread use for generating coherent radiation in wavelength ranges not directly accessible by lasers such as the mid IR region. The work presented in this thesis is concerned with the degenerate version of SFG when both fields have the same frequency, i.e. $\omega_1 = \omega_2$, and a response is generated at twice this frequency. This process is known as *second harmonic generation* (SHG) and will be further discussed shortly

2.4 Coupled Wave Equations

Maxwell's equations for a nonmagnetic dielectric medium, without free charges or currents, can be re-written into a wave equation,

$$\nabla^2 E - \frac{\epsilon}{c^2}\frac{\partial^2 E}{\partial t^2} = \frac{1}{\epsilon_0 c^2}\frac{\partial^2 P}{dt^2}, \tag{2.09}$$

where E is the electric field, P is the polarization, c is the speed of light and ϵ_0 and ϵ are the permittivity of vacuum and the relative permittivity of the material respectively. For monochromatic waves, the E-field and the corresponding polarization can be written as:

$$E(r,t) = \frac{1}{2}\sum_n (\hat{E}_n(r)e^{i\omega t} + c.c.) \tag{2.10}$$

$$P^{NL} = \frac{1}{2}\sum_n (\hat{P}_n{}^{NL}(r)e^{i\omega t} + c.c.) \tag{2.11}$$

Substituting these expressions into the wave equation yields a separate equation for each amplitude component:

$$\nabla^2 \hat{E}_n(r) + \frac{\epsilon\omega_n^2}{c^2}\hat{E}_n(r) + \frac{\omega_n^2}{\epsilon_0 c^2}\hat{P}_n^{NL}(r) = 0 \tag{2.12}$$

Assigning the direction of propagation as the z-axis, the E-field and nonlinear polarization can be written as,

$$\hat{E}_n(r) = \tilde{E}_n(z)e^{-ik_n z}, \tag{2.13}$$

$$\hat{P}_n^{NL}(r) = \tilde{P}_n^{NL}(z)e^{-ik_n z}, \tag{2.14}$$

where the identities, $k = \frac{n\omega}{c}$ and $\epsilon = n^2$ have been used.

Assuming that the amplitude of the E-field varies slowly along the direction of propagation [1],

$$\left|\frac{\partial^2 \tilde{E}}{\partial z^2}\right| \ll \left|\frac{k\partial \tilde{E}}{\partial z}\right|, \tag{2.15}$$

the equation simplifies to:

$$\frac{\partial}{\partial z}\tilde{E}_n(z) = -\frac{i\omega_n}{2c\epsilon_0 n_n}\tilde{P}_n^{NL}(z) \tag{2.16}$$

2.5 Second Harmonic Generation

In the case of SHG, there are only two interacting waves at frequencies ω_1 and $\omega_2 = 2\omega_1$ and the expression for the E-field becomes:

$$E(z,t) = \frac{1}{2}\sum_{n=1}^{2}\tilde{E}_n(z)e^{i(\omega_n t - k_n z)} + c.c. \tag{2.17}$$

Inserting this expression into the simplified wave equation and identifying the corresponding frequency terms of the nonlinear polarization gives a set of coupled wave equations:

$$\frac{\partial}{\partial z}\tilde{E}_1(z) = -\frac{i\omega_1}{cn_1}d\tilde{E}_2(z)\tilde{E}_1^*(z)e^{-i\Delta kz} \tag{2.18}$$

$$\frac{\partial}{\partial z}\tilde{E}_2(z) = -\frac{i\omega_1}{2cn_2}d\tilde{E}_1(z)\tilde{E}_1(z)e^{i\Delta kz} \tag{2.19}$$

In these expressions, the *phase-mismatch*, Δk, between the waves is defined as:

$$\Delta k = k_2 - 2k_1 = \frac{2(n_2 - n_1)\omega_1}{c} \tag{2.20}$$

If it is assumed that no radiation is lost to absorption, then $\chi^{(2)} = \chi^{SHG}$ in both equations, and:

$$\frac{dI_1}{dz} = -\frac{dI_2}{dz}, \tag{2.21}$$

implying energy conservation as expected under the assumption of a lossless medium. If the proportion of the fundamental that is converted into SHG is low enough, the intensity of the pump is approximately constant, allowing the second equation to be integrated and squared to give the intensity,

$$I_2 = \frac{1}{2}c\epsilon_0 n_2|E_2|^2 = \frac{2{\omega_1}^2 d^2 I_1^2 z^2}{\epsilon_0 c^3 n_2 n_1^2}sinc^2\left(\frac{\Delta kz}{2}\right) \tag{2.22}$$

While the assumption of low conversion efficiency simplifies the mathematical treatment, conversion efficiencies as high as 95 % can be achieved through engineering of the interaction [4].

As seen from eq. (2.22), the generated intensity is proportional to the square of the pump intensity (I_1) and the distance (z). However it also depends on the phase-mismatch, which should be zero for maximum output intensity.

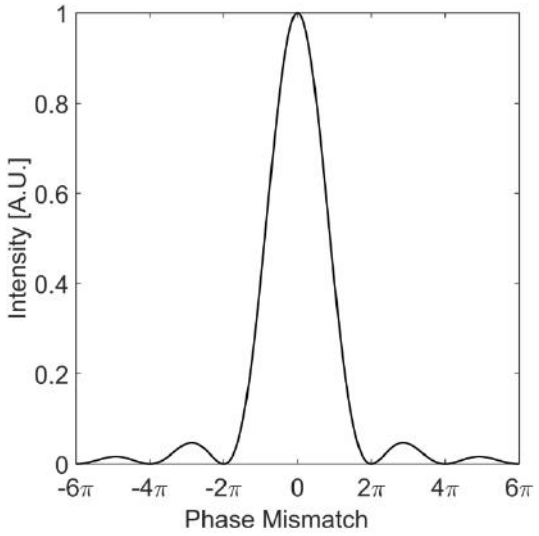

Figure 2.2: SHG output intensity versus the phase-mismatch

When the phase mismatch is non-zero, the phase-velocities of the fundamental and the second harmonic will differ and energy will be transferred from the fundamental to the second harmonic only for a certain distance before the process is reversed and the energy flows back to the fundamental wave. The distance over which the maximum energy transfer occurs is called the *coherence length*, L_c, defined as:

$$L_c = \frac{\pi}{\Delta k} \tag{2.23}$$

If the phase mismatch is eliminated, the phases of the second harmonic generated at each point along the beam add up constructively and the second harmonic field grows continuously. This is achieved through a process known as *phase matching.* Two different phase matching techniques are commonly used: *birefringent phase matching* (BPM) and *quasi-phase matching* (QPM).

2.6 Phase Matching

2.6.1 Birefringent Phase Matching

BPM uses the fact that, in some materials, the refractive index is dependent on the polarization of the incident light waves, so called *birefringence*. This effect is exploited by orienting the polarization of the interacting waves so that the refractive indices of the incoming and the generated waves coincide. In a *uniaxial* birefringent material, the index of refraction depends on the angle between the polarization of the wave and the *optical axis* of the medium. A *biaxial* crystal has three refraction indices corresponding to the three *principal axes* and the index of refraction for a given polarization depends on the angle between these axes and the direction of polarization of the wave. There are two types of BPM, *noncritical* BPM, in which the waves are polarized along one of the axes of the index ellipsoid and temperature tuning is used to equalize the indices of refraction; and *critical* BPM, where the electric fields are at different angles to the axes of the index ellipsoid in order to exploit the angular dependence of the index of refraction. Noncritical BPM is favorable in comparison to critical phase-matching as the latter case causes the Poynting-vector to deviate from the propagation vector, limiting the interaction length and thus the conversion efficiency. The BPM technique poses several disadvantages. The polarization orientations must be chosen so that the phase-matching condition is fulfilled which may conflict with the choice of polarization that would result in the highest nonlinear coefficient, resulting in lower conversion efficiency. Secondly, since strong birefringence is needed to compensate for large phase-mismatches, the wavelength range that can be phase-matched may be limited. Finally, high temperature may be needed to compensate the phase-mismatch.

2.6.2 Quasi-Phase Matching

The QPM scheme uses a different approach. As discussed above, in the absence of phase-matching, the energy of the second harmonic increases for one coherence length after which the energy is transferred back to the fundamental over the subsequent coherence length. In QPM this is counteracted by reversing the phase of the induced polarization every coherence length by periodically changing the sign of the nonlinear coefficient.

This periodic modification can be described by a function $g(x)$, with a period, Λ, and a value alternating between +1 and -1. By expanding $g(x)$ as a Fourier series, the following expression is obtained [5]:

$$g(z) = \Sigma_{m=-\infty}^{\infty} G_m \exp(-ik_m z), \tag{2.24}$$

where $k_m = \frac{2\pi m}{\Lambda}$, is the magnitude of the m:th harmonic of the grating vector. The Fourier coefficients G_m are given by the expression,

$$G_m = \frac{2}{\pi m} sin(\pi m D) \qquad (m = 1, 2, 3 \ldots), \tag{2.25}$$

where, $D = \frac{l}{\Lambda}$, is the *duty cycle*, i.e. the proportion l of each period Λ that has a positive sign of the nonlinear coefficient. This way, the effective nonlinear coefficient can be written:

$$d_{eff}(z) = d_{il} \cdot g(z) \tag{2.26}$$

When the expression for $d(z)$ is inserted into the coupled wave equations, the terms where the grating vector, k_m, compensates the phase-mismatch, Δk, will dominate the Fourier expansion, i.e. terms where,

$$\Delta k - K_m = 0, \tag{2.27}$$

which is the case if the period, Λ, satisfies the equation,

$$\Lambda = \frac{2\pi m}{\Delta k} \tag{2.28}$$

This way, the effective nonlinear coefficient is reduced to $d_{eff} = G_m d_{ijk}$ and assumes its maximum value for $m = 1$, and duty cycle $D = 0.5$. The duty cycle is a key parameter when fabricating QPM-gratings; deviation from the optimal duty-cycle leads to lower conversion efficiency as seen in figure 2.3(a), showing the value of the coefficients G_m as a function of D.

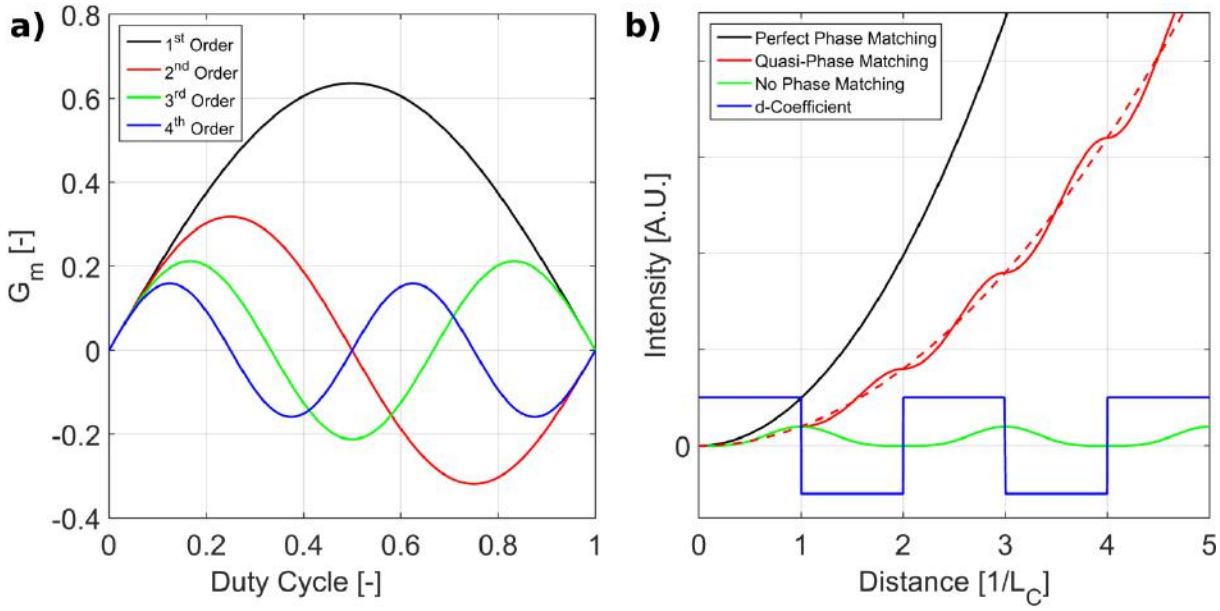

Figure 2.3: (a), Variation of the G coefficients as a function of the duty cycle, (b), Intensity variation vs distance for perfect phase matching (black), first order QPM (red), no phase matching (green) and the spatial modulation of the Nonlinear coefficient (blue).

The effect of the QPM scheme can be seen in figure 2.3(b) where the intensity is plotted as a function of the distance in the case of: no phase-matching, perfect phase matching and first order QPM with 0.5 duty cycle. The spatial modulation of the nonlinear coefficient in the QPM scheme is also shown. As seen in the figure, the scheme does give a continuously increasing SHG intensity, but the resulting output is lower than what would be achieved by perfect phase matching under the same conditions. In practice however, the conditions are not the same, QPM has several advantages compared to BPM: First, the process does not depend on the birefringence meaning that any choice of polarization for the interacting waves can be chosen. In particular, all waves can be polarized along the same direction which means that the largest component of the nonlinear tensor can be used and phase-matching can be achieved even in non-birefringent materials [6]. Secondly, the freedom of choosing the orientation direction also means that the Poynting-vector walk-off can be eliminated by propagating the beams along a crystal axis. Finally, since the phase-matching structure can be tailored, the same medium can be used for an extensive range of interactions, eliminating the need to find new materials with suitable characteristics for every new application. This flexibility can be further extended to for instance make gratings with a chirped period that phase-match more than one wavelength [7]; to make gratings with a transversal chirp that allow the phase-matching wavelength to be tuned through a lateral translation of the crystal [8]; or to enable interactions where the phase-mismatch is too large to be compensated for by birefringence [9].

References to Chapter 2

[1] P. N. Butcher and D. Cotter, "The elements of nonlinear optics", Cambridge University Press (1990).

[2] V. K. Wadhawan, "Introduction to ferroic materials", Gordon and Breach Science Publishers (2000).

[3] J. A. Giordmaine and R. C. Miller, "Tunable coherent parametric oscillation in $LiNbO_3$ at optical frequencies", Phys. Rev. Lett. **14** (24), 973 (1965).

[4] S. Ast, R. M. Nia, A. Schönbeck, N. Lastzka, J. Steinlechner, T. Eberle, M. Mehmet, S. Steinlechner, and R. Schnabel, "High-efficiency frequency doubling of continuous-wave laser light," Opt. Lett. **36**, 3467–3469 (2011).

[5] L. E. Myers, R. C. Eckardt, M. M. Fejer, R. L. Byer, W. R. Bosenberg, and J. W. Pierce, "Quasi-phase-matched optical parametric oscillators in bulk periodically poled $LiNbO_3$", Opt. Soc. Am. B, **12**, 2102 (1995).

[6] K. Devi, P. G. Schunemann, and M. Ebrahim-Zadeh, "Continuous-wave, multimilliwatt, mid-infrared source tunable across 6.4–7.5 μm based on orientation-patterned GaAs", Opt. Lett. **39**, 6751 (2014).

[7] M. A. Arbore, O. Marco, and M. M. Fejer, "Pulse compression during second-harmonic generation in aperiodic quasi-phase-matching gratings", Opt. Lett. **22**, 865 (1997).

[8] A. M. Schober, G. Imeshev, and M. M. Fejer, "Tunable-chirp pulse compression in quasi-phase-matched second-harmonic generation", Opt. Lett. **27**, 1129 (2002).

[9] C. Canalias, V. Pasiskevicius, M. Fokine, and F. Laurell, "Backward quasi-phase-matched second-harmonic generation in submicrometer periodically poled flux-grown $KTiOPO_4$", Appl. Phys. Lett. **8,** 181105 (2005).

3. Ferroelectrics

Ferroelectrics are part of a general class of materials known as *ferroics* that includes ferromagnets, ferroelectrics and ferroelastics. Common to these materials is that they have a physical quantity (magnetization, polarization or strain) that is stable in the absence of applied fields and whose direction can be switched through the application of an external field along certain axes of the material. In the case of *multiferroics,* ordering of more than one of these quantities occurs in the same material. Because of these properties ferroics find widespread use in applications such as computer memories, electronics and sensors.

3.1 Crystal Classes and Ferroelectricity

The properties of crystalline materials are to a large extent defined by the symmetry properties of their lattices [1]. Consequently materials can be classified into symmetry groups, defined by their invariance under spatial transformations such as rotations and reflections. Any such operation that leaves the crystal lattice unchanged must also leave its properties unchanged; this limits which structures are compatible with ferroelectricity. In total there are 32 crystal classes or *point groups*, defined by the symmetry operations that leave their lattice points invariant. Out of the 32 crystal classes, 11 are centrosymmetric, meaning that the charge is symmetrically arranged around some point, precluding spontaneous polarization. Of the remaining 21 groups 20 are piezoelectric, i.e. they display the *piezoelectric effect* [5].

If a piezoelectric material is subjected to stress along certain directions, the resulting deformation of the lattice causes a polarization proportional to the applied stress to develop. Conversely, if an electric field is applied along those same directions, the material becomes strained or deformed through the *inverse piezoelectric effect*.

Out of the 20 piezoelectric symmetry groups, 10 are polar, meaning that they display spontaneous polarization. In all polar crystals the *pyroelectric effect* is observed; since the polarization is temperature dependent, heating or cooling of the materials causes a change in the spontaneous polarization. This change causes a redistribution of the screening charges leading to charge accumulation on the crystal surfaces. Ferroelectric crystals are the subset of the polar crystals in which the spontaneous polarization can be switched by the application of an electric field.

3.2 Ferroelectric Concepts and Definitions

3.2.1 Polarization and Spontaneous Polarization

Ferroelectric materials can be represented as an assembly of point charges. If the centers of positive and negative charge do not coincide, the material has a nonzero polarization, $\boldsymbol{P}$, defined as:

$$\boldsymbol{P} = \frac{1}{V}\int_V \boldsymbol{r}\rho(\boldsymbol{r})dV, \tag{3.0 1}$$

where V is a representative volume containing all the species of interest and $\boldsymbol{r}$ is the position [2]. In all *dielectrics*, polarization can be induced through the application of an external electric field, **E**, according to:

$$\frac{\partial \boldsymbol{P}}{\partial \boldsymbol{E}} = \epsilon_0 \chi^{(1)} \tag{3.0 2}$$

for a low-field, linear, response (as discussed in chapter 2). In materials with *spontaneous polarization*, P_S, the polarization remains, even in the absence of an external field.

3.2.2 Piezoelectric Effect

The polarization can change in response to mechanical forces; when external stress is applied to a piezoelectric material the polarization changes according to the *piezoelectric effect*,

$$\frac{\partial P_i}{\partial X_{jk}} = d_{ijk} \tag{3.0 3}$$

where d is the piezoelectric tensor. Conversely, if an electric field is applied, strain is induced according to the *converse piezoelectric effect*,

$$\frac{\partial S_{jk}}{\partial E_i} = d_{ijk} \tag{3.04}$$

3.2.3 Pyroelectric Effect

The spontaneous polarization generally changes with changing temperature, a phenomenon known as the *pyroelectric effect.* In materials displaying this effect a charge will develop on the polar faces in response to a temperature change. Pyroelectricity can be measured by depositing externally connected electrodes on the polar faces and measuring the current flow between them as a function of the temperature change. The *pyroelectric coefficient,* $\boldsymbol{p}$, is a measure of the degree of polarization change with changing temperature:

$$\boldsymbol{p} = \frac{\partial \boldsymbol{P}}{\partial T} \tag{3.0 5}$$

Two different phenomena contribute to the pyroelectric effect; the *spurious* or *secondary* pyroelectric effect is due to thermal expansion or contraction of the crystal resulting in deformation while the *true* or *primary* pyroelectric effect occurs even when the material is prevented from expanding and is due to a redistribution of charges in response to the changing temperature [1].

3.2.4 Depolarization Field and Depolarization Energy

The electric displacement field is defined as [1],

$$D_i = \epsilon_0 E_i + P_i \tag{3.0 6}$$

where the polarization is the combined spontaneous and induced polarization. If the field is sufficiently weak, then the induced polarization can be written as,

$$P_i = \epsilon_0 \chi_{ij} E_j + P_{S,i} \tag{3.0 7}$$

At points where the displacement field is discontinuous, such as the surfaces of a finite crystal or at defects in the crystal structure, charge will accumulate according to the Poisson equation,

$$\rho = \nabla \cdot \boldsymbol{D} \tag{3.0 8}$$

Inserting the expression from eq. (3.06) above, the charge density can be written as,

$$\rho = \epsilon \nabla \cdot \boldsymbol{E} + \nabla \cdot P_S \tag{3.0 9}$$

where $\epsilon = \epsilon_0(1 + \chi)$. In the interior of a perfect crystal, the spontaneous polarization is constant and therefore $\nabla \cdot P_S = 0$, however, at points where the crystal structure is interrupted, e.g. due to defects or at the crystal surface, there is an abrupt change in polarization resulting in charge accumulation. The field associated with this charge accumulation is called the *depolarization field*, since it counteracts the field of the spontaneous polarization. The charge accumulation has a non-zero formation energy, the *depolarization energy*, which can be calculated from the resulting charge distribution, according to [3],

$$U_d = \frac{1}{2} \int \int \frac{\rho_1 \rho_2}{\epsilon r_{12}} dV_1 dV_2 \,, \tag{3.10}$$

where $\rho_1$and ρ_2 are the charge densities in volumes V_1 and V_2, separated by a distance r_{12}. This energy is lowered if the volume is divided into domains with alternating polarization orientation.

If the material is conductive, the depolarization field will induce a current resulting in charge accumulation on the polar surfaces in a way that counteracts the depolarization field, so called *internal screening*. In an insulating ferroelectric, the depolarization field will attract ambient

charges to the polar surfaces until the field is compensated through *external screening.* In practice, intermediate cases also occur, the speed of each process determining which screening type is dominant.

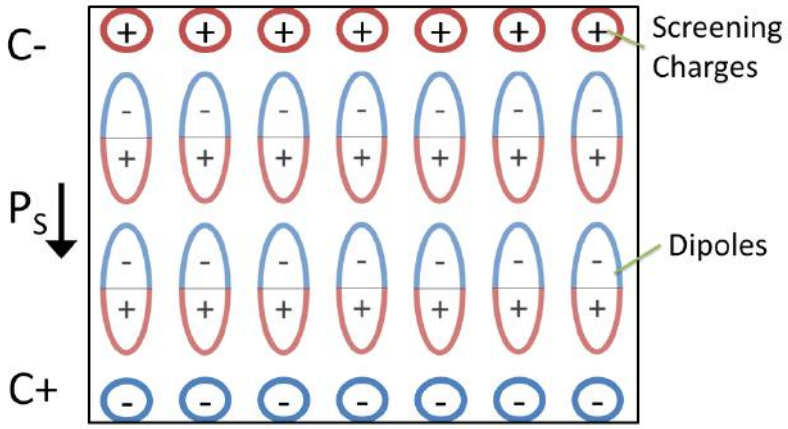

Figure 3.1: The spontaneous polarization and screening charges

3.3 Thermodynamic Description

The ferroelectric state of a material has a low degree of symmetry and occurs at lower temperatures. It is generally related to a high symmetry paraelectric state occurring at high temperature through the loss of one or several symmetry elements [1] via a *phase transition.* The temperature at which this transition occurs is called the *Curie temperature*, T_C. Depending on the origin of the polarization ferroelectrics are classified as either *order-disorder* type, meaning that the spontaneous polarization arises from the ordering of dipoles present in the material, or *displacive* type, meaning that the centers of positive and negative charge are displaced, causing the spontaneous polarization. These categories can be considered limiting cases and transitions involving both elements are also possible.

Phase-transitions can be understood within the framework of Landau theory [5]. The basis of this theory is that, near the transition temperature, the free energy of the system can be expanded in a power series in an *order parameter,* a measure representative of the degree of ordering. For a *proper ferroelectric* the order parameter is the spontaneous polarization, P_S. In *improper ferroelectrics,* ferroelectricity arises as a consequence of a phase-transition driven by some other physical quantity [4]. The series expansion of the Landau theory must respect the symmetry of the material, meaning that only even powers of P_S are to be included (otherwise a rotation of the material or the coordinate system would change its energy, a physical impossibility). The series expansion can be written as,

$$G(P,T) = G_0 + \frac{1}{2}\beta(T - T_c)P^2 + \frac{1}{4}\gamma P^4 + \frac{1}{6}\delta P^6 \tag{3.11}$$

for the Gibbs free energy, G. Here, G_0 is the background energy and the coefficients in Greek letters (β, γ and δ) are taken as positive constants, assigning all the temperature dependence to the second term. In principle, the other terms may also be temperature dependent, and the series may include further terms, however, the expression above captures the essential features of a paraelectric-ferroelectric phase-transition and is sufficient for the present discussion [5]. Figure 3.2 shows the free energy obtained by eq. (3.11) for temperatures below, at and above the Curie temperature. Above T_C the material is unordered and there is no spontaneous polarization; as the temperature is lowered, the potential curve gradually flattens and below T_C the energy minimum at zero polarization loses stability and two symmetric minima with nonzero spontaneous polarization appear.

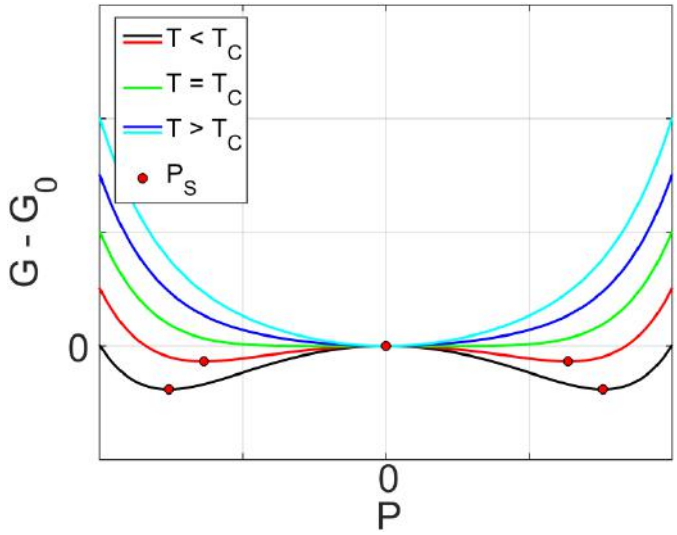

Figure 3.2 Free energy as a function of spontaneous polarization, above, at, and below the Curie temperature T_C

The analysis above is valid in the absence of external electric fields. If an external field, E, is present, a field-dependent term must be added to the expression for the free energy:

$$G(P,T) = G_0 + \frac{1}{2}\beta(T - T_c)P^2 + \frac{1}{4}\gamma P^4 + \frac{1}{6}\delta P^6 - PE \tag{3.12}$$

corresponding to a tilted free-energy curve, with two unequal minima, as shown in figure 3.3(a). At equilibrium the system is at rest and, $\partial G/\partial P = 0$. By inserting the expression for the Gibbs free energy of eq. (3.12), the following expression for relationship between the external field and the polarization is obtained:

$$E = \beta(T - T_c)P + \gamma P^3 + \delta P^5 \tag{3.13}$$

At temperatures below T_C, eq. (3.13) defines a hysteresis-loop shown in figure 3.3(b). The hysteretic PE-curve is an important feature of ferroelectrics: At high electric fields the behavior is that of an ordinary dielectric, a change in the electric field causes a response in the form of induced polarization. At field strengths close to and below a critical field, known as the *coercive field,* the behavior is different: For each value of the electric field there are two different polarization states; in particular, at zero applied field these two unequal states of nonzero polarization remain. If a field higher than the coercive field is applied in a direction contrary to the spontaneous polarization, that polarization orientation loses stability and the polarization switches to the opposite orientation. By applying an AC-bias with sufficient amplitude, the hysteresis loop can be measured, yielding a PE-curve, like that shown in figure 3.3(c).

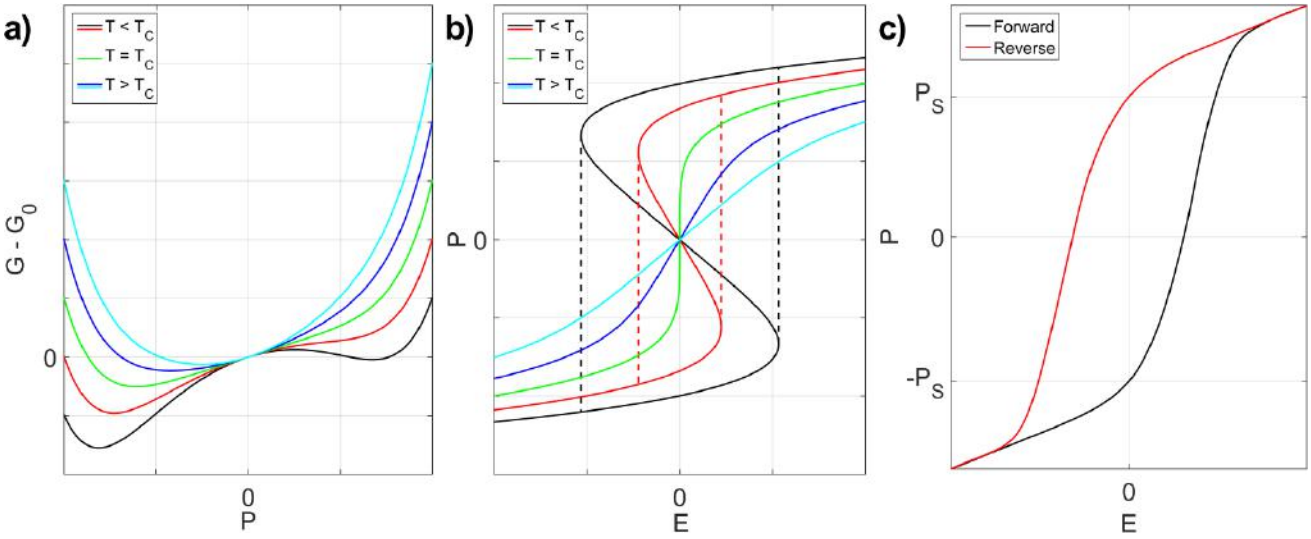

Figure 3.3 (a) Free energy as a function of spontaneous polarization in the presence of an external field, (b) Ferroelectric hysteresis loops as described by eq. (3.12), (c) Typical ferroelectric hysteresis loop, adapted from [1]

In practice, the value of the E_c depends on the temperature, the temporal shape of the field used to switch the polarization and the material of the electrodes used to contact the ferroelectric. It also depends on the direction of switching due to the *internal field* that arises from the distribution of nonstoichiometric defects in the crystal [6]. When the polarization switches, the screening charges are displaced, and the corresponding charge, which has to be supplied through the electrodes to switch a given area, A, is given by:

$$Q_{Switching} = 2P_S A \tag{3.14}$$

Polarization reversal has many applications such as memory devices and transistors [7]; piezoelectric actuators [8]; and nonlinear optics [9]. For many of these applications, its usefulness lies in the fact that the polarization is not necessarily homogeneous throughout the material, but separated into different regions with uniform polarization orientation, so called *ferroelectric domains*; the delineations between the domains are known as *ferroelectric domain walls* (DWs).

3.4 Polarization Reversal

Since polarization reversal in ferroelectrics has many important applications, it has been an intensively studied topic for several decades. A generally accepted model of the process was suggested by Merz and has later been further developed [10, 11]. In this model, domain reversal starts through the formation of domain nuclei at the sample interface. The lowest energy configuration for such nuclei is a *dagger shape*, elongated along the polar axis with a minuscule base area, thus minimizing the depolarization energy. The nuclei then expand along the polar axis, maintaining the favorable elongated shape. In its initial formulation, the theory predicted unreasonably low probabilities for nucleation due to the high energy associated with each nucleus [12]. This subsequently led to the realization that the sample interface and crystal defects play a key role in the switching process, by lowering the nucleation energy [13]. Furthermore the choice of electrode material can have a big impact on the nucleation probability.

Once the nuclei have grown through the full thickness of the sample, sideways expansion and domain coalescence begins. Lateral motion of the domain walls has inaccessibly high activation energy, and therefore, domain sideways expansion occurs via preferential nucleation along the edges of existing domains [3]. These nuclei will also have the energetically favored dagger shape, as sketched for two different cases in figure 3.4. Since nucleation at a domain wall incurs a lower net change of domain surface area then nucleation in the absence of a wall, the corresponding energy is also lower. Furthermore, the energy associated with nucleation of growth steps at an existing wall also depends on the local shape of the wall; walls with ledges and irregularities have larger surfaces and consequently a higher energy. Nucleation at such walls, (e.g. at point “1” in figure 3.4) will incur a smaller net change of the wall surface area than nucleation at smooth walls (point “2”). Since the wall energy is dependent on its surface area, nuclei at ledges will have lower formation energy and consequently rough domain walls are more mobile than their regular counterparts [14]. In general, the speed of the domain wall lateral motion depends on the nucleation rate of these growth steps. Since the nucleation rate is exponentially dependent on the applied field strength; the speed of the poling process is also exponentially dependent on the field strength in the so-called *low field regime*. As the field increases the growth speed of the steps becomes the limiting process and the polarization switching enters the *high field regime* with linear field dependence [15].

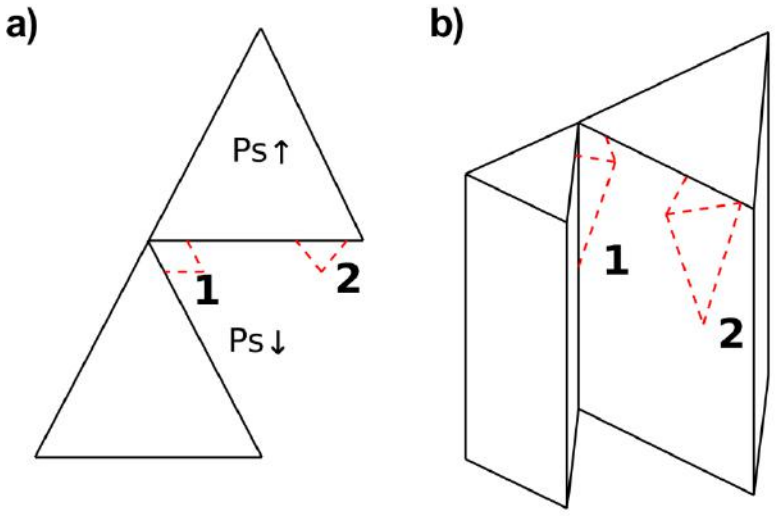

Figure 3.4: Sideways domain expansion through preferential nucleation at domain walls, adapted from [14]

3.5 Ferroelectric Domains and Domain Walls

A separation of a ferroelectric into a heterogeneous aggregate of domains can occur as the result of a phase-transition from a higher symmetry phase [1] or through domain engineering by the application of an external field as previously discussed. The different domains have the same crystal structure, but differ in orientation. At the domain wall, the orientation changes from one state to another.

The stability of the domain structure depends on the formation energy of the DWs in relation to the depolarization energy. The depolarization energy is lowered by splitting the crystal into smaller domains of opposite polarization, thus lowering the potential energy of the screening charges [16]. However, the formation energy of the DW is positive [17] and so the energy-preferred domain structure becomes a balance between these two contributions. The depolarization energy for a periodic domain structure can be calculated by from the following expression [5],

$$W_E = \frac{\epsilon^* d P_0^2 V}{t}, \tag{3.15}$$

where d is the domain width, t is the crystal thickness, P_0 is the polarization at the center of the domain, V is the crystal volume and ϵ^* is a constant dependent on the dielectric constants of the ferroelectric.

If the DW is assumed to have an energy per unit area, σ, then the total energy of the walls is,

$$W_W = \frac{\sigma V}{d} \tag{3.16}$$

Minimizing the total energy, $W_E + W_W$ gives the equilibrium domain width,

$$d = \left(\frac{\sigma t}{\epsilon^* P_0^2}\right)^{\frac{1}{2}}, \tag{3.17}$$

known as the Kittel law. The domain widths predicted by eq. (3.17) are commonly observed in spontaneously formed domain structures [18]. However, the calculation does not take the effect of crystallographic defects into account: Domain walls can lower their energy by interacting with crystal defects, a phenomenon known as *pinning* [19]. This allows for periodically poled structures with much higher aspect-ratios than what would be predicted by eq. (3.17) to be created.

In ferroelectrics, the DW energy is dominated by the strong coupling between polarization and strain; therefore, contrary to the case of ferromagnetic DWs, the structural changes tend to occur over distances of a few unit cells [20, 21, 22].

The properties of a domain wall are to a large extent governed by its geometry; walls are often categorized by the angle between the polarization vectors of the domains they separate. Depending on the material, there may be several polarization states at various angles allowing for a range of possible wall orientations, termed 90° walls, 180° walls etc. In improper ferroelectrics, the symmetry lowering is not due to the spontaneous polarization itself and any angle can be achieved [23]. KTP is a proper ferroelectric with two possible polarization states and consequently 180° walls are the only possibility. For 180° domain walls, the polarization on both sides of the wall is always antiparallel; however, the angle of the wall itself can vary, influencing the wall stability and charge-transport properties. In particular, walls can have an angle to the spontaneous polarization, as shown in figure 3.5.

At domain walls at an angle to the spontaneous polarization, the polarization is discontinuous at the wall,

$$\nabla \cdot \boldsymbol{P_S} \neq 0 \tag{3.18}$$

producing bound charge at the wall. This bound charge will increase the wall energy. If mobile charges are present in the crystal, the bound charge can be neutralized, and a screening charge density,

$$\sigma = 2\mathrm{P_s}\sin(\alpha), \tag{3.19}$$

where α is the wall angle will develop.

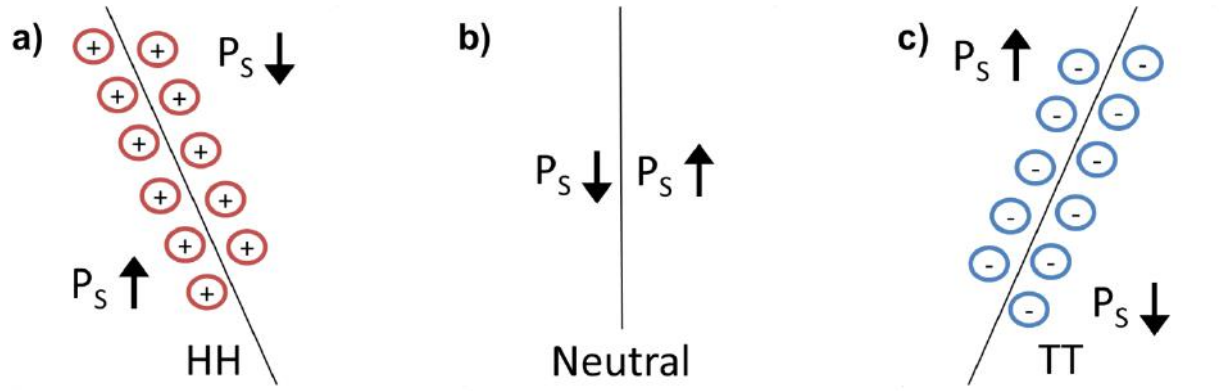

Figure 3.5: Screening-charge accumulation at (a) head-to-head, (b) electrically neutral and (c) tail-to-tail domain walls

Such charged walls are usually characterized as *head-to-head* (HH) or *tail-to-tail* (TT) depending on the angle between the wall and the spontaneous polarization. At HH walls, the spontaneous polarization vectors on opposite sides of the wall face each other and positive screening charges will accumulate. At a TT wall, the polarization vectors face away from each other and a negative charge develops. The domain walls are situated inside the material and consequently they cannot be externally screened. Since unscreened charged walls have high formation energy [24], the availability of mobile screening charges determines the probability of charged domain wall formation. In KTP, the high mobility of the K ions readily screen the polarization and inclined domain walls in the HH configuration are commonly observed. At the DW, the crystal structure changes from one polarization state to another state with the same symmetry but a different orientation. This change must somehow be incorporated into the crystal structure; in ferroelectrics the structural transition occurs over a short distance, sometimes as little as a single unit cell [25]. However, the strain induced by the lattice mismatch at the wall affects the crystal symmetry some distance away. This means that close to the wall, the symmetry can differ from that of the parent material and that otherwise forbidden properties can occur at the wall. As an example, symmetry-forbidden nonlinear optical coefficients have been observed at the domain walls of KTP [26].

Another feature of interest is the conductive properties of DWs [27]. Domain walls can lower their energy through defect pinning; in a similar manner mobile defects may be attracted to the walls. In many materials, defects are associated with free electrical carriers, causing the defect aggregations to act as conductive channels through the material. This phenomenon was first demonstrated in WO_3 where Na ions, introduced into the material through a vapor reaction, were demonstrated to accumulate at domain walls, indicating preferential transportation along the wall [28]. Later, Seidel et al, demonstrated increased conductivity at the domain walls in undoped $BiFeO_3$ [29]. Following these discoveries, enhanced domain wall conductivity has been reported in many ferroelectrics such as $Pb(Zr_xTi_{1-x})O_3$ [30], $ErMnO_3$ [31], $HoMnO_3$ [32] and $LiNbO_3$ [33]. When measuring the conductivity along the polar direction of a ferroelectric, the interface between the external electrode and the polar face of the ferroelectric influences the result. It has

been shown that the polarization state at the interface can affect the local band structure, thus changing the height of the tunneling barrier between the electrode and the ferroelectric [34]. Similarly, charged species accumulating at the DW can affect the tunneling barrier and contribute to the local conductivity enhancement at the walls [35].

References to Chapter 3

[1] V. K. Wadhawan, "Introduction to ferroic materials", Gordon and Breach Science Publishers (2000).

[2] ANSI/IEEE std. 180-1986, "IEEE Standard Definitions of Primary Ferroelectric Terms", The Institute of Electrical and Electronics Engineers, Inc. (New York, 1986).

[3] R. C. Miller and G. Weinreich, "Mechanism for the Sidewise Motion of 180° Domain Walls in Barium Titanate", Phys. Rev. **117**, 1460-1466 (1960).

[4]A. P. Levanyuk and D. G Sannikov, "Improper ferroelectrics", Sov. Phys. Usp. **17,** 199 (1974).

[5] M. E. Lines and A.M. Glass, "Principles and Applications of Ferroelectrics and Related Materials", Oxford University Press (1977).

[6] V. Gopalan, T. E. Mitchell, Y. Furukawa, and K. Kitamura, "The role of nonstoichiometry in 180° domain switching of $LiNbO_3$ crystals", Appl. Phys. Lett. **72**, 1981 (1998).

[7] J. F. Scott, "Prospects for Ferroelectrics: 2012 – 2022", ISRN Mater. Sci., 187313 (2013).

[8] T. Higuchi, K. Suzumori, and S. Tadokoro, "Next-Generation Actuators Leading Breakthroughs", Springer-Verlag (2010).

[9] M. Yamada, N. Nada, M. Saitoh, and K. Watanabe, "First order quasiphase matched LiNbO3 waveguide periodically poled by applying an external field for efficient blue second harmonic generation", Appl. Phys. Lett. **62**, 435 (1993).

[10] W. J. Merz, "Domain Formation and Domain Wall Motions in Ferroelectric $BaTiO_3$ Single Crystals," Phys. Rev. **95**(3), 690-698 (1954).

[11] E. Fatuzzo and W. J. Merz, "Switching Mechanism in Triglycine Sulfate and Other Ferroelectrics," Phys. Rev. **116**, 61-68 (1959).

[12] R. Landauer, "Electrostatic Considerations in BaTiO3 Domain Formation During Polarization Reversal", J. Appl. Phys. **28**, 227 (1957).

[13] G. Gerra, A.K. Tagantsev, and N. Setter, "Surface-Stimulated Nucleation of Reverse Domains in Ferroelectrics", Phys. Rev. Lett. **94**, 107602 (2005).

[14] V. Gopalan and T.E. Mitchell, "In Situ Video Observation of 180° Domain Switching in $LiTaO_3$ by Electro-Optic Imaging Microscopy", J. Appl. Phys. **85**, 2304 (1999).

[15] C. Canalias, J. Hirohashi, V. Pasiskevicius, and F. Laurell, "Polarization-Switching Characteristics of Flux-Grown $KTiOPO_4$ and $RbTiOPO_4$ at room temperature", J. Appl. Phys., **97**, 124105 (2005).

[16] A. K. Tagantsev, L.E. Cross, and J. Fousek, ”Domains in Ferroelectric Crystals and Thin Films”, Springer (2010).

[17] G. Catalan, J. Seidel, R. Ramesh, and J. F. Scott, “Domain wall nanoelectronics”, Rev. Mod. Phys. **84**, 119 (2012).

[18] G. Catalan, H. Bea, S. Fusil, M. Bibes, P. Paruch, A. Barthelemy, and J. F. Scott, “Fractal Dimension and Size Scaling of Domains in Thin Films of Multiferroic $BiFeO_3$”, Phys. Rev. Lett., **100**, 027602 (2008).

[19] T. J. Yang, V. Gopalan, P. J. Swart, and U. Mohideen, “Direct Observation of Pinning and Bowing of a Single Ferroelectric Domain Wall”, Phys. Rev. Lett., **82**, 4106, (1999).

[20] B. Meyer and D. Vanderbilt, ”Ab initio study of ferroelectric domain walls in PbTiO3”, Phys. Rev. B., **65**, 104111 (2002).

[21] C., Jia, S., Mi, K., Urban, I., Vrejoiu, M., Alexe and D., Hesse, “Atomic-scale study of electric dipoles near charged and uncharged domain walls in ferroelectric films”, Nat. Mater. **7**, 57 (2007).

[22] Catalan, G., Scott, J., Schilling, A., Gregg, J. M., “Wall Thickness Dependence of the Scaling Law for Ferroic Stripe Domains”, J. Phys.: Condens. Matter **19**, 022201 **(**2007).

[23] D. Meier, J. Seidel, A. Cano, K. Delaney, Y. Kumagai, M. Mostovoy, N. A. Spaldin, R. Ramesh, and M. Fiebig, “Anisotropic conductance at improper ferroelectric domain walls”, Nat. Mater. **11**, 284 (2012).

[24] M. Y. Gureev, A. K. Tagantsev, and N. Setter,” Head-to-head and tail-to-tail 180° domain walls in an isolated ferroelectric”, Phys. Rev. B **83**, 184104 (2012).

[25] P. Pernot-Rejmankova, P. A. Thomas, P. Cloetens, T. Lyford, and J. Baruchel, “Structural matching of ferroelectric domains and associated distortion in potassium titanyl phosphate crystals,” J. Phys.: Condens. Matter **15**, 1613 (2003).

[26] A. Fragemann, V. Pasiskevicius, and F. Laurell, “Second-order nonlinearities in the domain walls of periodically poled $KTiOPO_4$**”,** Appl. Phys. Lett. **85**, 375 (2004).

[27] R. K. Vasudevan, W. Wu, J. R. Guest, A. P. Baddorf, A. N. Morozovska, E. A. Eliseev, N. Balke, V. Nagarajan, P. Maksymovych, and S. V. Kalinin, ”Domain Wall Conduction and Polarization-Mediated Transport in Ferroelectrics”, Adv. Funct. Mater. **23**, 2592 (2013).

[28] A. Aird and E. K. H. Salje, “Sheet superconductivity in twin walls: experimental evidence of WO_{3-x}“, J. Phys.: Condens. Matter **10,** L377 (1998).

[29] J. Seidel, L. W. Martin, Q. He, Q. Zhan, Y. H. Chu, A. Rother, M. E. Hawkridge, P. Maksymovych, P. Yu, M. Gajek, N. Balke, S. V. Kalinin, S. Gemming, F. Wang, G. Catalan, J. F. Scott, N. A. Spaldin, J. Orenstein, and R. Ramesh, "Conduction at domain walls in oxide multiferroics ", Nat. Mater. **8**, 229 (2009).

[30] J. Guyonnet, I. Gaponenko, S. Gariglio, and P. Paruch, "Conduction at Domain Walls in Insulating $Pb(Zr_{0.2}Ti_{0.8})O_3$Thin Films", *Adv. Mater.*, **23**, 5377 (2011).

[31] D. Meier, J. Seidel, A. Cano, K. Delaney, Y. Kumagai, M. Mostovoy, N. A. Spaldin, R. Ramesh, M. Fiebig, "Anisotropic conductance at improper ferroelectric domain walls", Nat. Mater., **11**, 284 (2012)**.**

[32] W. Wu, Y. Horribe, N. Lee, S. W. Cheong and J. R. Guest, "Conduction of Topologically Protected Charged Ferroelectric Domain Walls", Phys. Rev. Lett., **108**, 077203 (2012).

[33] M. Schröder, A. Haußmann, A. Thiessen, E. Soergel, T. Woike, L. M. and Eng, "Conducting Domain Walls in Lithium Niobate Single Crystals", Adv. Funct. Mater., **22**, 3936 (2012).

[34] P. W. M. Blom, R. M. Wolf, J. F. M. Cillessen, and M. P. C. M. Krijn, "Ferroelectric Schottky Diode", Phys. Rev. Lett. **73**, 2107 (1994).

[35] S. Farokhipoor and B. Noheda. "Conduction through 71◦ domain walls in $BiFeO_3$ thin films", Phys. Rev. Lett., **107**(12):127601 (2011).

4. KTP and Rb-doped KTP

4.1 Crystal Structure

KTP is one of the compounds of the $MTiOXO_4$ family, where M is K, Rb, Tl, NH_4 or Cs and X is either P or As [1]. These isomorphs share the same crystal structure but can vary substantially in terms of optical and conductive properties. Intermediate forms, where one of the elements is partially substituted for another one, are also possible. Of particular interest here is $Rb_{1-x}K_xTiOPO_4$ (RKTP), were a small portion of the K has been substituted for Rb (in the RKTP crystals used in this thesis x was 0.003). Even such low substitution rates of K for Rb, drastically lowers the ionic conductivity and the susceptibility to photochromic damage while leaving most other properties unchanged. In this section, as well as in the rest of the chapter, the archetypical KTP will be used as an example. In cases were the statements do not apply to RKTP, the RKTP specific properties will be explicitly described.

KTP has an orthorhombic crystal structure and belongs to the point group mm2 (space group $pna2_1$) [1]. Each primitive cell contains eight formula units of KTP and the lattice constants are, a = 12.819 Å, b = 6.399 Å and c = 10.584 Å. The rigid structure consists of two main building blocks: TiO_6 octahedra and PO_4 tetrahedra. The octahedra form chains along the $[011]$ and $[01\bar{1}]$ axes that are held together by transversal tetrahedra bridges. The TiO_6 octahedra are not symmetric but distorted so that one Ti-O bond is shorter and another longer than the remaining four of intermediate length [2]. The bond-distortion causes a net polarization of 0.24 C/m^2 along the c-axis [3]. The asymmetric Ti-O bonds also contribute to the high optical nonlinearity of KTP; a study on the isomorphic $KSnOPO_4$ in which the Sn-O bonds are much less distorted than their Ti-O counterparts in KTP, revealed a 98 % reduction of SHG intensity as compared to KTP [4]. However, based on calculations of the contributions from each chemical bond in the structure, it has also been claimed that the K-O bonds and PO_4 tetrahedra are the main source of the nonlinearity [5].

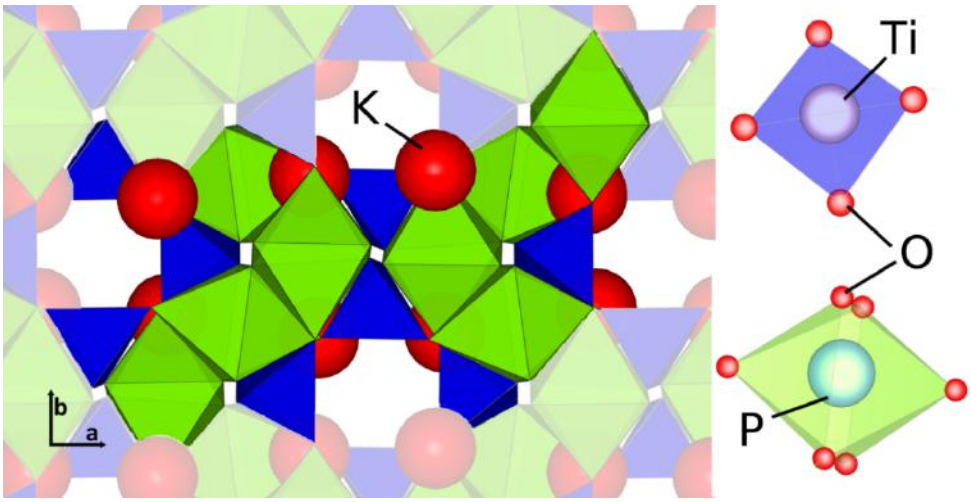

Figure 4.1: The crystal structure of KTP

The K ions sit in voids within the TiO_6- PO_4 network; there are two different such positions, one 8-coordinated (K1) and one 9-coordinated (K2). The ionic conductivity in KTP is due to the K ions hopping between neighboring sites. The two nonequivalent K sites are the result of a phase-transition from a high temperature, centrosymmetric phase, where all K ion sites are equivalent [6, 7]. During this transition the K ions are displaced along the c-axis, lowering the crystal symmetry. Each K site is related by pseudosymmetry to a corresponding *hole site*, the corresponding lattice position in a hypothetical crystal structure rotated by 180°.

It has been proposed that during polarization reversal, a displacement of the K ions, similar to the paraelectric-ferroelectric phase transition occurs whereby the 8-coordinated K ion shifts to its pseudosymmetric 9-coordinated position, while the 9-coordinated K shifts into an 8-coordinated position followed by a relaxation of the surrounding oxygen atoms, in which the long and short Ti-O bonds are interchanged [8]. In RKTP, where K is partially substituted with Rb, the Rb ions preferentially occupy the K(2) site [4]; the preferential occupation of the K(2) site was 78 % for doping concentrations as high as 44 %. For the much lower Rb concentration of the RKTP crystals used in this work, the preferential occupation is therefore expected to be close to 100 %.

In KTP, the domain walls preferentially form parallel to the *a*-plane, since this orientation results in a minimal rotation of the PO_4 tetrahedra and do not intersect the Ti-O chains of the crystal structure [9]. X-ray analyses of domain walls in KTP have shown that the continuity of the PO_4-TiO_6 chains are maintained across walls parallel to the *a*-plane and the structural transition across the wall occurs through rotation of the PO_4 tetrahedra [10].

4.2 Crystal Synthesis

KTP and its isomorphs melt incongruently (for pure KTP, melting occurs at 1150 °C [1]) and therefore cannot be grown using melt techniques such as Czochralski growth [11], that are commonly used when possible due to their relative simplicity and low cost. Instead, solution-growth techniques must be employed. Two different methods are commonly used, hydrothermal growth and flux growth.

The hydrothermal technique is the best technique to achieve high quality KTP. It consists in sealing an aqueous solution of the constituents in an inert container under high temperature and high pressure (500 – 900°C, 70 – 180 Mpa) [12]. A temperature gradient is created across the container, allowing crystallization at the cool end while convection from the hot end transports fresh material to the crystallization area. A seed-crystal, i.e. a small piece of single-crystal, is usually placed in the crystallization point to avoid random nucleation as this tends to result in poor crystal quality [11]. While the hydrothermal method produces crystals of very high quality, the high pressures and temperatures needed complicates the growth of large crystals. Combined with the low growth-rates inherent to the method this makes such crystals far more expensive than those grown using the flux-technique.

The major advantage of the flux growth technique is that crystal growth can be achieved under ambient pressure. This eliminates the need for a pressurized growth chamber, drastically lowering complexity and cost while allowing bigger crystals to be grown. For this reason most commercially available KTP isomorphs are grown using this technique. The method consists in dissolving the crystal constituents in a solvent, or *flux* in crystal growing terminology, and the growth takes place at elevated temperature (750 – 1150 °C) in an inert atmosphere to avoid contamination. The crystallization is started by gradually cooling the flux while ensuring constant mixing of the reactants by rotating the seed crystal and the crucible. Since the different crystal faces grow at different rates and with different properties, the seed orientation can be used to control the final result [13]. The properties of each crystal face also depend on the growth temperature, stirring conditions and exact contents of the flux; and the ideal conditions are a compromise between the desired crystal quality and growth rate [14]; in particular, the crystal stoichiometry is greatly dependent on the growth temperature [15].

The commercially available RKTP crystals used for the experiments presented here, were grown by the flux growth technique using a flux were 1.5 % of the K is substituted for Rb [16], resulting in a substitution rate of 0.3 % in the final crystal [17]. Other proportions of Rb to K have previously been reported using the same growth technique [6].

In a recent modification of the flux-growth technique, a crystal with a periodic domain grating was used as a seed [18]. This way a periodic structure can be grown from the template, allowing the volume of the domain structure to be scaled. The growth process takes place at 732 °C, below the Curie and roughening temperatures, preserving the crystal morphology and domain structure.

Using this technique, high-quality gratings with 38.86 μm were grown with thickness of up to 225 μm on each polar face.

4.3 Conductive Properties

KTP is an ionic conductor at room temperature, due to the high mobility of K ions along its polar axis. As mentioned previously, the K ions sit in voids in the surrounding TiO_6- PO_4 network. Since they are loosely bound to this network, they are free to move between adjacent sites through a vacancy hopping mechanism. This ability is closely related to the occupancy number of the K sites since the ions can only move to neighboring sites that are unoccupied. The DC conductivity of KTP was shown to obey a Poole-Frenkel relationship [19]:

$$\sigma = \sigma_0 \exp\left(\left(\frac{e^3 E}{\epsilon_0 \epsilon_r}\right)^{\frac{1}{2}} \cdot \frac{1}{k_B T}\right), \tag{4.01}$$

Where, σ_0, is the field-independent conductivity component, ϵ, is the high-field dielectric constant and. The temperature variation of the conductivity can be described as the sum of two Arrhenius terms,

$$\sigma(T) = A\, exp\left(-\frac{E_{a,h}(dc)}{k_B T}\right) + B \exp\left(-\frac{E_{a,l}(dc)}{k_B T}\right), \tag{4.02}$$

where *A* and *B* are constants, *T* is the temperature, k_B is the Boltzman constant and $E_{a,h}$ and $E_{a,l}$ are the activation-energies for ion-hopping in the high- and low- temperature regime respectively [20]. At temperatures below 180 K the superionic conductivity freezes in. The conductivity is highly anisotropic, varying by four orders of magnitude from its highest value parallel to the c-axis to the much lower conductivity perpendicular to this axis [3]. The reason for this anisotropy can be found in a similar anisotropy of the conductive paths in the crystal structure. The paths connecting the vacant K sites consist of series of *bottlenecks* in the crystal structure. Furusawa et al [21] analyzed these bottlenecks and found that motion along either crystal axis occurs in a meandering fashion and involves passage through two out of total four bottlenecks present in the structure; depending on the direction of motion the ions must pass through different combinations of these bottlenecks. The activation energy of each bottleneck was evaluated, using the assumption that it is determined by the ratio of the ionic radius of the K ion and the physical size of the opening in the crystal lattice. As found by their analysis, motion along the c-axis can be achieved through a combination of the two widest bottlenecks, corresponding to a much lower activation energy than any combination required for motion in the ab-plane.

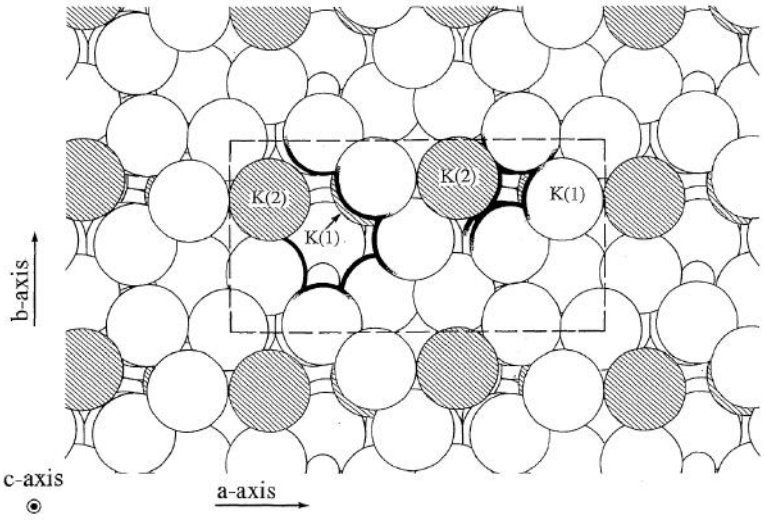

Figure 4.2: Bottlenecks in the KTP structure [21]

The correlation between the ionic radius and the activation energy for motion through the crystal lattice also explains the effect of partially substituting K for Rb. The ionic radius of Rb is greater than that of K, increasing its activation energy for hopping and consequently a much lower conductivity is measured in RKTP [22]. The effect persists even at very low doping concentrations; as pointed out by Wang et al [23], due to the quasi-one dimensional nature of the ionic motion, a single rubidium ion may impede the motion of a large number of K ions. Flux grown KTP and RKTP presents nonstoichiometric defects on the K and O sublattices [15]. At elevated temperatures, oxygen atoms are expulsed from the crystal causing an increased concentration of K vacancies, needed to maintain charge neutrality. Therefore, the number of vacancies depends strongly on the range of temperatures used during the growth-process and consequently the conductivity varies by several orders of magnitude between crystals grown at different temperatures.

The vacancy concentration also varies spatially across the crystal as a consequence of temperature gradients or changing flux composition during the crystal growth process. This can be seen by measuring the conductivity along the c-axis across a crystal slab. Figure 4.3 shows such a measurement performed over the c-face of a KTP crystal with dimensions 30x18x1 mm^3 along the a-, b-, and c- axes respectively in figure 4.3(a) and an RKTP crystal of dimensions 25x20x1 mm^3 in figure 4.3(b). For both materials, the conductivity has a rather flat profile along the a-axis but varies substantially along the b-axes; in KTP the variation is threefold from 40 μS/m at the edge to 120 μS/m at the center while for RKTP it is even greater, from 0.5 μS/m to 2.5 μS/m in the center. These measurements clearly show the large impact of even a very low dopant concentration of Rb; in the RKTP crystal of figure 4.3(b) only 0.3% of the K was substituted for Rb, resulting in 2 orders of magnitude lower conductivity.

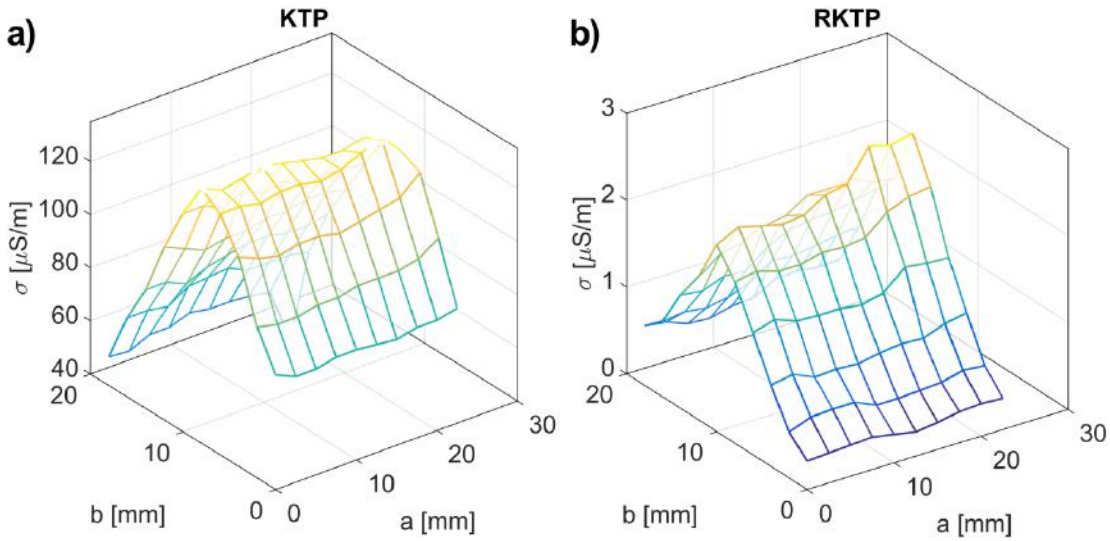

Figure 4.3: Conductivity along the c-axis of (a) KTP, and (b) RKTP

4.4 Optical Properties

The KTP family of materials offers high damage thresholds for photorefractive damage at room temperature as well as good resistance to surface damage [24]. Since the damage threshold varies with material quality, wavelength, and pulse duration; the reported levels vary from around 1 GW/cm^2 to 3 GW/cm^2 at room temperature [25] for KTP. This compares favorably to the damage threshold of the commonly used congruent lithium niobate (0.19 GW/cm^2) and lithium tantalate (0.61 GW/cm^2) [26].

Furthermore, KTP isomorphs are normally operated at room temperature while commonly available, congruently melting, crystal-compositions of the LN family generally need high temperatures (>100°C) to avoid excessive damage [27].

However, these crystals are susceptible to so called *gray tracking* when exposed to radiation in the visible range. Absorption induced injection of free carriers leads to formation of color centers in the crystal bulk with broad absorption bands in the visible and near IR spectra. While these centers are reversible, the increased absorption may result in permanent photo-refractive damage.

It has been shown that the color centers are stabilized by mobile stoichiometric defects such as V_K^- and V_O^{2+} [28]. By lowering the defect mobility the stability of the color centers can be lowered; indeed because of its much lower ionic conductivity RKTP is far less susceptible to gray-tracking.

The nonlinear-optical tensor for materials of the mm2 class has five nonzero elements; these coefficients were reported for KTP by Bierlein and Vanherzeele for frequency doubling at 1.06 μm [29]:

$$d = \begin{bmatrix} 0 & 0 & 0 & 0 & d_{15} & 0 \\ 0 & 0 & 0 & d_{24} & 0 & 0 \\ d_{31} & d_{32} & d_{33} & 0 & 0 & 0 \end{bmatrix} = \begin{bmatrix} 0 & 0 & 0 & 0 & 6.1 & 0 \\ 0 & 0 & 0 & 7.6 & 0 & 0 \\ 6.5 & 5.0 & 13.7 & 0 & 0 & 0 \end{bmatrix} \text{(pm/V)},$$

As seen from the table, the major nonlinearity corresponds to the coefficient d_{33}, i.e. with all interacting waves polarized along the crystal c-axis, and consequently this geometry is most commonly used for frequency conversion. The d coefficients have not been measured for RKTP, however, due to the low substitution rates used for the RKTP crystals in this thesis, they are expected to be very similar to those of KTP. The transmission spectrum of KTP spans from 360 nm to 4000 nm [30] allowing it to be used for frequency conversion applications covering the entire visible and part of the infrared spectrum. In the isomorphic KTA where the phosphate is substituted by arsenic, the transparency window is extended to around 5200 nm, reaching further into the infra-red region.

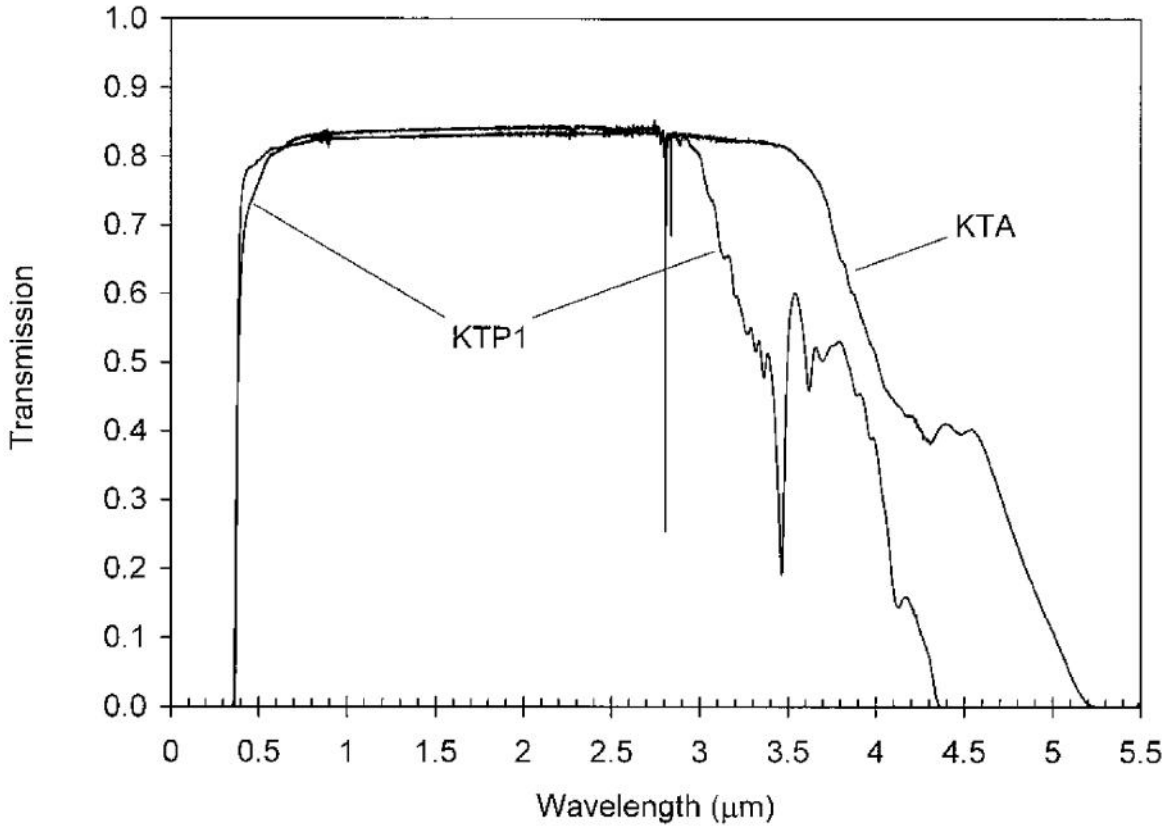

Figure 4.4: Transparency range of KTP [30]

The electro-optic coefficients of KTP were measured by Bierlein and Arweiler [3]:

$$r = \begin{bmatrix} 0 & 0 & r_{13} \\ 0 & 0 & r_{23} \\ 0 & 0 & r_{33} \\ 0 & r_{42} & 0 \\ r_{51} & 0 & 0 \\ 0 & 0 & 0 \end{bmatrix} = \begin{bmatrix} 0 & 0 & 9.5 \\ 0 & 0 & 15.7 \\ 0 & 0 & 36.3 \\ 0 & 7.3 & 0 \\ 9.3 & 0 & 0 \\ 0 & 0 & 0 \end{bmatrix} \text{(pm/V)},$$

In order to calculate the periodicity of the grating needed for a certain QPM application, the variation of the refractive index as a function of the wavelength and the temperature needs to be known. The index of refraction can be calculated for using the Sellmeier equations:

$$n^2 = A + \frac{B}{1 - C\lambda^{-2}} - D\lambda^2 \tag{4.03}$$

where suitable coefficients A-D for wavelengths below 1 µm were reported by Fan et al [31] with a temperature correction with coefficients reported by Wiechmann [32] et al on the form:

$$\frac{dn}{dT} = \frac{a}{\lambda^3} + \frac{b}{\lambda^2} + \frac{c}{\lambda} + d \tag{4.04}$$

For wavelengths above 1 µm, the data reported by Fradkin et al [33] with corrections by Eamanuelli and Arie [34] are more suitable. Due to the structural similarity between KTP and RKTP the same coefficients apply well to both materials.

References to Chapter 4

[1] L.K. Cheng, L.T. Cheng, J. Galperin, P.A. Morris Hotsenpiller, and J.D. Bierlein, "Crystal growth and characterization of $KTiOPO_4$ isomorphs from the self-fluxes", Cryst. Growth., **137**, 107 (1994).

[2] F. C. Zumsteg, J. D. Bierlein, and T. E. Gier, "$K_xRb_{1-x}TiOPO_4$: A new nonlinear optical material," J. Appl. Phys. **47**, 4980 (1976).

[3] J. D. Bierlein and C. B. Arweiler, "Electro-optic and dielectric properties of KTiOPO4", Applied Physics Letters, **49**, 917 (1986).

[4] P. A. Thomas, A. M. Glazer, and B. E. Watts, "Crystal Structure and Nonlinear Optical Properties of $KSnOPO_4$ and their Comparison with $KTiOPO_4$", Acta Cryst., **B46**, 333 (1990).

[5] D. Xue and S. Zhang, "The origin of nonlinearity in KTiOPO4," Appl. Phys. Lett. **70**, 943 (1997).

[6] P. A. Thomas, S. C. Mayo, and B. E. Watts, "Crystal structures of $RbTiOAsO_4$, $KTiO(P_{0.58},As_{0.42})O_4$, $RbTiOPO_4$ and $(Rb_{0.465},K_{0.535})TiOPO_4$ and analysis of pseudosymmetry in crystals of the $KTiOPO_4$ family", Acta Crystallogr., **B48**, 401 (1992).

[7] P. A. Thomas and A. M. Glazer, "Potassium titanyl phosphate, $KTiOPO_4$. II. Structural interpretation of twinning, ion exchange and domain inversion", J. Appl. Cryst., **24**, 968 (1991).

[8] R. A. Stolzenberger and M. P. Scripsick, "Recent advancements in the periodic poling and characterization of RTA and its isomorphs," Proc. SPIE **3610**, 23 (1999).

[9] J. D. Bierlein and F. Ahmed, "Observation and poling of ferroelectric domains in $KtiOPO_4$", Applied Physics Letters **51**, 1322 (1987).

[10] P. Pernot-Rejmankova, P. A. Thomas, P. Cloetens, T. Lyford, and J. Baruchel, "Structural matching of ferroelectric domains and associated distortion in potassium titanyl phosphate crystals," J. Phys.: Condens. Matter **15**, 1613 (2003).

[11] T. Nishinga and P. Rudolph, "Handbook of Crystal Growth", Elsevier (2011).

[12] R. A. Laudise, R. J. Cava, and A. J. Caporaso, "Phase relations, solubility and growth of potassium titanyl phosphate, KTP," J. Crystal Growth, **74**, 275 (1986).

[13] N. Angert, M. Tseitlin, E. Yashchin, and M. Roth, "Ferroelectric phase transition temperatures of KTiOPO4 crystals grown from self-fluxes", Appl. Phys. Lett., **67**, 1941 (1995).

[14] P. F. Bordui, R. Blachman, and R. G. Norwood, "Improved optical transmission of KTiOPO4 crystals through cerium-doping and oxygen annealing", Appl. Phys. Lett., **61**, 1369 (1992).

[15] P. A. Morris, ”Impurities in Nonlinear Oxide Crystals”, Cryst. Growth., **106**, 76 (1990).

[16] P. A. Thomas, S. C. Mayo, and B. E., Watts, “Crystal Structures of $RbTiOAsO_4$, $KTiO(P_{o.ss},As_{o.4})O_4$, $RbTiOPO_4$ and $(Rb_{o.46},K_{o.3})TiOPO_4$, and Analysis of Pseudosymmetry in Crystals of the $KTiOPO_4$ Family”, Acta Crvst. **B48**, 401 (1992).

[17] F. Masiello, T. A. Lafford, P. Pernot, J. Baruchel, D. S. Keeble, P. A. Thomas, A. Zukauskas, G. Strömqvist, F. Laurell, and C. Canalias, "Investigation by coherent X-ray section topography of ferroelectric domain behavior as a function of temperature in periodically poled Rb:KTP," J. Appl. Cryst. **44**, 462 (2011).

[18] A. Peña, B. Menaert, B. Boulanger, F. Laurell, C. Canalias, V. Pasiskevicius, P. Segonds, C. Felix, J. Debray, and S. Pairis, “Template-growth of periodically domain-structured $KTiOPO_4$“, Opt. Mater. Express, **1**, 185 (2011).

[19] Q. Jiang, M. N. Womersley, P. A. Thomas, J. P. Rourke, K. B. Hutton, and R. C. C. Ward, “Ferroelectric, conductive, and dielectric properties of $KTiOPO_4$ at low temperature”, Phys. Rev. B **66**, 094102 (2002).

[20] P. Urenski, N. Gorbatov, and G. Rosenman, ” Dielectric relaxation in flux grown $KTiOPO_4$ and isomorphic crystals”, J. Appl. Phys. **89**, 3, 1851 (2001).

[21] S. Furusawa, H. Hayasi, Y. Ishibashi, A. Miyamoto, and T. Sasaki, ”Ionic Conductivity of Quasi-One-Dimensional Superionic Conductor KtiOPO4 (KTP) Single Crystal”, J. Phys. Soc. Jpn. **62**, 183 (1993).

[22] Q. Jiang., P. A. Thomas, K. B. Hutton, and R. C. C. Ward, ”Rb-doped potassium titanyl phosphate for periodic ferroelectric domain inversion”, Journal of Applied Physics **92**, 2717 (2002).

[23] S. Wang, V. Pasiskevicius, and F. Laurell, ”High-efficiency frequency converters with periodically-poled Rb-doped KTiOPO4”, Optical Materials, **30**, 594 (2007).

[24] M. Peltz, U. Bader, A. Borsutzky, R. Wallenstein, J. Hellström, H. Karlsson, V. Pasiskevicius, F. Laurell, “Optical parametric oscillators for high pulse energy and high average power operation based on large aperture periodically poled KTP and RTA”, Appl. Phys. B: Lasers and Optics **73**, 663 (2001).

[25] F. Ahmed, “Laser damage threshold of KTiOPO4,” Appl. Opt. **28**, 119 (1989).

[26] D. S. Hum, R. K. Route, G. D. Miller, V. Kondilenko, A. Alexandrovski, J. Huang, K. Urbanek, R. L. Byer, and M. M. Fejer, “Optical properties and ferroelectric engineering of vapor-transport-equilibrated, near-stoichiometric lithium tantalate for frequency conversion”, Journal of Applied Physics **101**, 093108 (2007).

[27] D. S. Hum and M. M., Fejer, ”Quasi-phasematching”, C. R. Physique **8**, 180 (2007).

[28] S. Tjörnhammar, V. Maestroni, A. Zukauskas, T. Kristijonas Uzdavinys, C. Canalias, F. Laurell, and V. Pasiskevicius, *“*Infrared absorption in KTP isomorphs induced with blue picosecond pulses*”,* Opt. Mater. Express **5**, 2951 (2015).

[29] H. Vanherzeele and J. D. Bierlein, “Magnitude of the nonlinear-optical coefficients of KTiOPO4,” Opt. Lett. **17**, 982 (1992).

[30] G. Hansson, H. Karlsson, S. Wang, and F. Laurell, ”Transmission measurements in KTP and isomorphic compounds”, Appl. Opt. **39**, 5058 (2000).

[31] T. Y. Fan, C. E. Huang, B. Q. Hu, R. C. Eckardt, Y. X. Fan, R. L. Byer, and R. S. Feigelson, ”Second harmonic generation and accurate index of refraction measurements in flux-grown KTiOPO4,” Appl. Opt. **26**, 2390 (1987).

[32] W. Wiechmann, S. Kubota, T. Fukui, and H. Masuda, “Refractive-index temperature derivatives of potassium titanyl phosphate”, Opt. Lett. **18**, 1208 (1993).

[33] K. Fradkin, A. Arie, A. Skliar, and G. Rosenman, “Tunable midinfrared source by difference frequency generation in bulk periodically poled KTiOPO4”, Appl. Phys. Lett. **74**, 914 (1999).

[34]S. Emanueli and A. Arie, “Temperature-Dependent Dispersion Equations for KTiOPO4 and KTiOAsO4,” Appl. Opt. **42**, 6661 (2003).

5. Characterization Techniques

Several characterization techniques have been used for the work presented in this thesis. The techniques can be divided into two categories: macroscopic techniques, that visualize domain structures down to the micrometer level, and nanoscale techniques, that show domain-features smaller than the wavelength of visible light. This chapter will give an overview of the techniques used in this thesis and describe their working principles.

5.1 Macroscopic Techniques

5.1.1 Selective Etching

Etching is the process of exposing a material to a liquid *etchant*, a chemical compound that gradually dissolves the material. The etchant is usually heated to speed up the process. In order for the process to be useful as a domain visualization tool, the etching must be selective, i.e. the etch-rate must differ between different polar faces of the material. When the etching process is terminated, the sample surface will display a relief-structure, with trenches corresponding to the regions with the higher etch-rates, allowing the different regions to be seen, using an optical microscope or an atomic force microscope. The selectivity may occur for various reasons; in the case of ferroelectrics, opposite polar faces have opposite charges; because of the electrostatic interactions, many etchants can be found that attack one polar face while leaving the opposite face untouched, thus causing selectivity. For example, hydrofluoric acid is commonly used to selectively etch various ferroelectrics such as $BaTiO_3$ [1] and $LiNbO_3$ [2]. For KTP, Laurell et al [3] reported that salts with hydroxide groups mainly affect the *c*- face. In the studies presented here, a solution of KOH and KNO_3 at 100 °C has been used for all selective etching. As demonstrated by Miller and Savage [4], selective etching can be used as a tool measuring domain wall motion. In this technique the sample is first etched to reveal the initial domain structure. Subsequently, domain wall motion is induced through the application of an external stimulus of interest, e.g. thermal annealing or the application of an electric field. Then a second etch is performed, creating a double-relief structure, showing both the initial and the final domain walls. An example of such a structure is shown in figure 5.1.

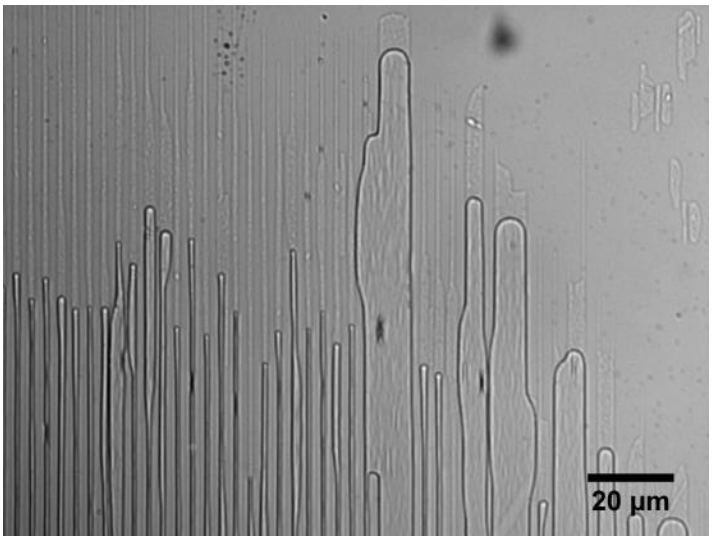

Figure 5.1: Double-relief structure in KTP

Selective etching has the advantage of being a fast way of visualizing domain structures; within a few minutes an entire crystal face spanning several square millimeters can be surveyed if the features are large enough to be seen optically.

5.1.2 SHG Mapping

SHG mapping can be used for assessing the quality of a QPM grating. In this technique a laser beam at the fundamental wavelength of the grating is launched along the crystal *a*-axis and the resulting second harmonic (SH) is detected. By measuring the power of the generated SH, the quality of the grating along the beam path can be calculated. Two different versions of this technique have been used in this thesis.

In the first version, a single-frequency laser beam is scanned across the *a*-face of a poled crystal and the resulting SH power maps out the quality of the grating. This technique is commonly employed *in situ* at the poling setup after the application of an electric pulse in order to assess the quality of the resulting grating. The advantage of this technique is its ability of directly showing the phase-matching efficiency of the grating without destroying the polar faces. However, the method only provides information integrated along the beam path rather than the state of individual domains.

In a modified version of the SHG mapping technique (*Online SHG)*, the laser beam is launched through the crystal during periodic poling, providing live monitoring of the polarization reversal. This technique was used in paper I to study domain dynamics. Since an electric field of several kV/mm is applied to the crystal, the electro-optic effect causes a shift in the refractive indices. This causes a shift in the phase-matching wavelength by 0.11 nm/kVmm^{-1}, resulting in 0.55 nm at a typical peak electric field of 5 kV/mm. To ensure efficient phase-matching throughout the

poling process, a mode-locked Ti:Sapphire laser was used as the pump-source for these experiments. The laser had a central wavelength of 842 nm, corresponding to first order SHG for the domain grating with a period of 4 μm, with a FWHM bandwidth of 6 nm and emitted 170 fs pulses at 76 MHz repetition rate.

The collimated laser beam with a 1/e2 radius of 30 μm was polarized along the crystal c-axis and launched along the crystal a-axis at an equal distance from both the c-faces. The generated SH at 421 nm and the remaining pump-beam were separated and each was measured using photodetectors with 14 ns temporal resolution allowing the fast dynamics of polarization reversal to be visualized.

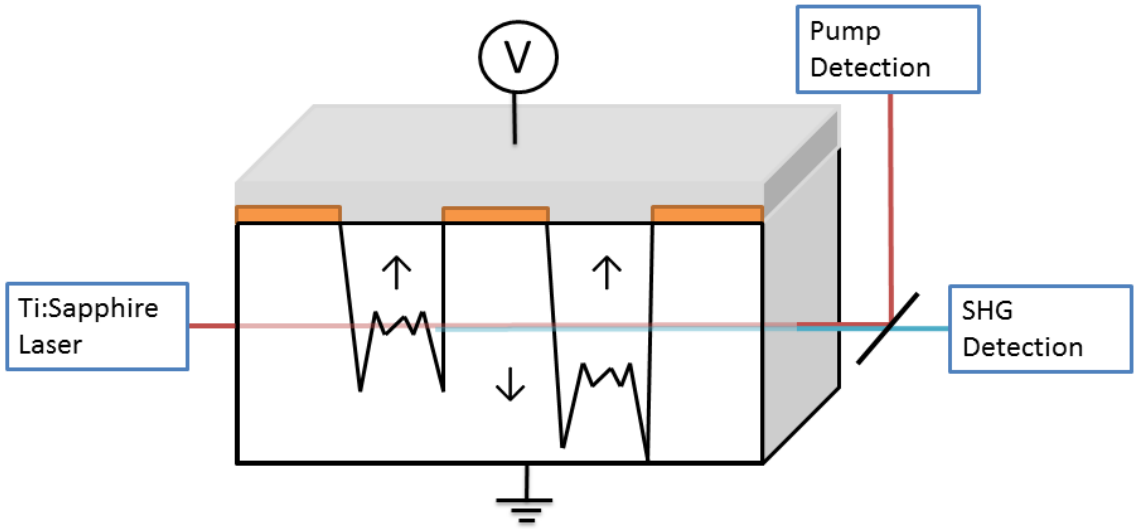

Figure 5.2: Online SHG experimental setup

5.2 Nanoscale Techniques

5.2.1 Atomic Force Microscopy

Since the invention of the scanning tunneling microscopy in 1982 [5], the concept of scanning probe microscopy was further developed, leading to the creation of *atomic force microscopy* (AFM) [6]. Through detection of short-range forces, AFM enables mapping the surface of essentially any material with nanometer resolution and has become a well-established and widely used technique for investigating surface properties of a multitude of materials in fields such as materials science, biology and chemistry. The working principle of an AFM is relatively simple: a sharp probe with a radius of a few nm at the tip is scanned over the sample surface, and the forces between the probe and the sample are registered, providing a topographical map of the sample with nanometer resolution.

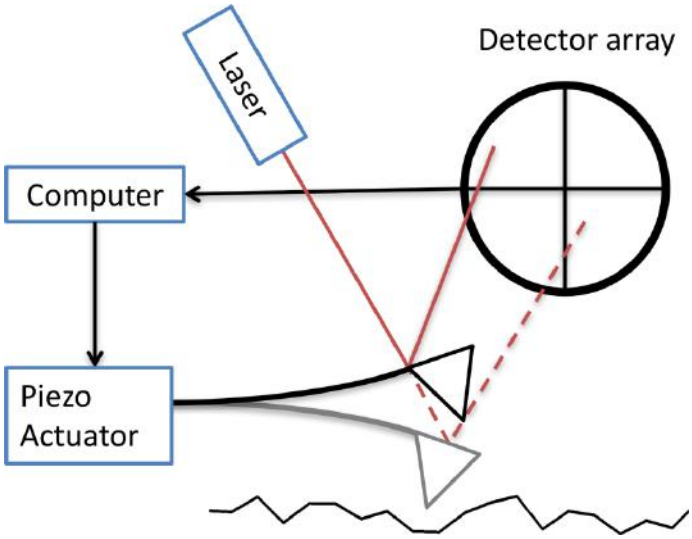

Figure 5.3: Working principle of AFM

The tip sits at the end of a cantilever and the motion of either the cantilever or the sample is controlled by a piezo-actuator. As the tip interacts with the sample, the cantilever bends, causing the reflection of a laser beam focused on the cantilever, to move across a detector array. The motion of the piezo-actuator is driven by a feedback loop using the tip deflection, as the control signal. In basic operation, the force acting on the tip is kept constant and the control signal sent to the actuator maps out the sample topography. Since a minuscule deflection of the tip translates into measurable motion of the reflected laser beam, and the piezo actuators have very high spatial resolution [7], AFMs can routinely detect topography variations on the nanometer level and below [8].

In this work, two modes of AFM operation have been used: *piezo-force microscopy* (PFM) and *tunneling AFM* (TUNA). All the experiments have been carried out under ambient conditions in air.

5.2.2 Piezoresponse Force Microscopy

Piezoresponse force microscopy (PFM) is an AFM technique for visualizing ferroelectric domain structures [9]. In PFM, a conductive tip is used and an AC-bias is applied between the tip and the sample. The bias induces strain into the material through the converse piezoelectric effect causing deflection of the tip. The deflection is measured using a lock-in amplifier and the amplitude and phase of the deflections are registered. As in normal AFM operation, the sample topography is mapped in parallel. Since the sign of the piezoelectric coefficient differs between domains of opposite polarization, a bias with a given polarity will cause one domain type to contract while the other expands. Therefore, the AC-bias will make the two domains oscillate with different phase, allowing the domain structure to be visualized in a phase-map. In theory the phase-shift should be 180° between domains while the amplitude should remain constant. In practice however, the tip-sample interaction is also affected by other factors, in particular electrostatic forces from charges at the sample surface. Because of these forces the domain-domain phase difference often deviates from 180° and there may be contrast in the amplitude signal [10].

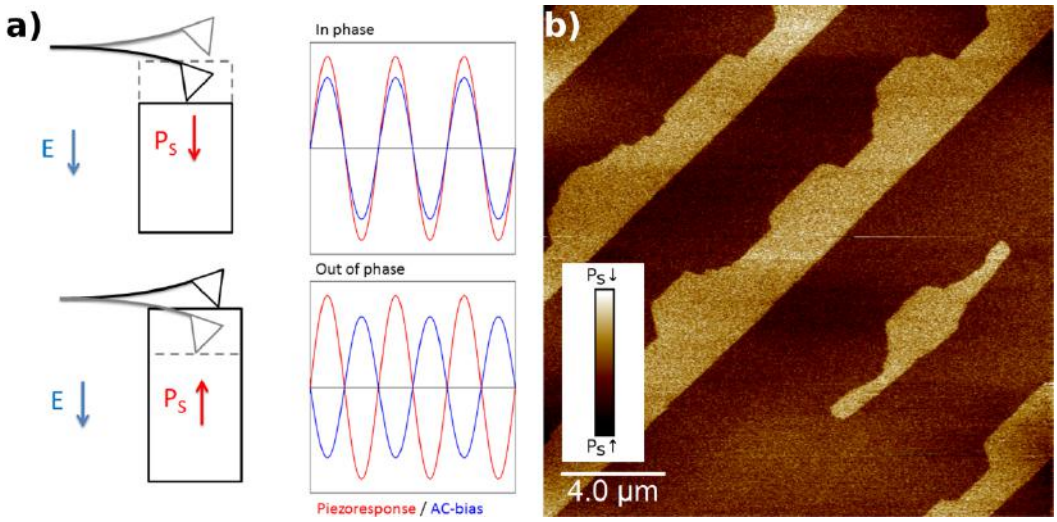

Figure 5.4: (a) Working principle of PFM, (b) PFM-phase Map

The PFM amplitude depends both on the converse piezoelectric effect and on electrostriction; by superimposing a DC bias on the AC-voltage and measuring the resulting amplitude using a lock-in amplifier the electrostrictive contribution can be filtered out, providing a direct measurement of the local d_{33} coefficient. However, since the electric field generated by the sharp tip is very inhomogeneous, the signal is only collected form an unknown sample volume close to the surface and therefore quantitative analysis is very difficult [11].

5.2.3 Tunneling AFM and Conductive AFM

Tunneling AFM (TUNA™) is one of several *conductive AFM* (CAFM) techniques in which a DC bias is applied between the sample and a conductive tip while the current passing through the probe is measured as the tip is scanned across the surface. This way, a map of the local conductivity is acquired alongside the topography. The defining feature of TUNA as compared to other CAFM techniques is its low-noise current amplifier capable of measuring electrical currents of less than 1 pA with better than 100 fA precision [12]. Since the measurement resolution of CAFM is very high, both in terms of current and spatial dimensions the technique allows investigating correlations between spatial and electrical properties of materials with very high precision. In particular, it has allowed the detection of increased conductivity at domain walls [13] and nano domains [14] in various ferroelectrics. The technique also enables the study of current-voltage (IV) characteristics at specific points such as domain walls; by maintaining the tip stationary and ramping the DC-bias, current-voltage curves are obtained.

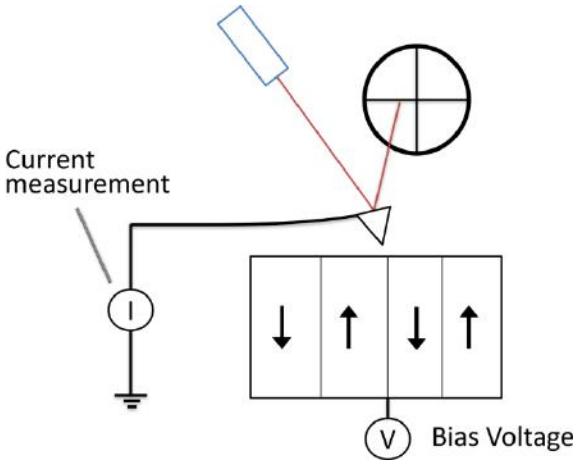

Figure 5.5 Working principle of CAFM

However, several things must be taken into account when analyzing the results, both in qualitative and quantitative terms. Firstly, the area of contact between the tip and the sample is only a few tens of square nm, making the quality of the electrical contact sensitively dependent on the local sample topography. Furthermore, since conductive AFM tips are normally non-conductive silicon tips with a conductive coating, the state of the coating has a high impact on the measured conductivity [15]. As the tip is scanned across the surface, the coatings tend to wear off and care must be taken to ensure that the coating is of sufficient quality throughout each measurement. Nevertheless, as this gradual deterioration is difficult to track, quantitative comparison between different measurements is complicated.

Secondly, the conductivity is highly sensitive to surface conditions and surfaces adsorbates can severely impair the measurements. Contaminants come in many forms; a first source of contamination is the ambient atmosphere during the measurements. Since in this case, the TUNA-scans were performed in air, there is always a water meniscus forming around the tip [16]. The meniscus affects the charge-transfer between the tip and the sample. Depending on the material, this transfer can include complicated electrochemistry that varies with the ambient conditions and the applied bias-voltage which means that the experimental results can vary depending on the relative humidity and temperature [17, 18, 19].

Another consideration is the surface quality. Because of the high sensitivity of the measurements, any contamination present on the surface can have a large impact on the results. To minimize this influence, all samples were thoroughly cleaned in acetone and isopropanol before each AFM-session. Despite these efforts, surface contamination could frequently be seen to affect the measurements and a substantial portion of the gathered data had to be discarded for this reason.

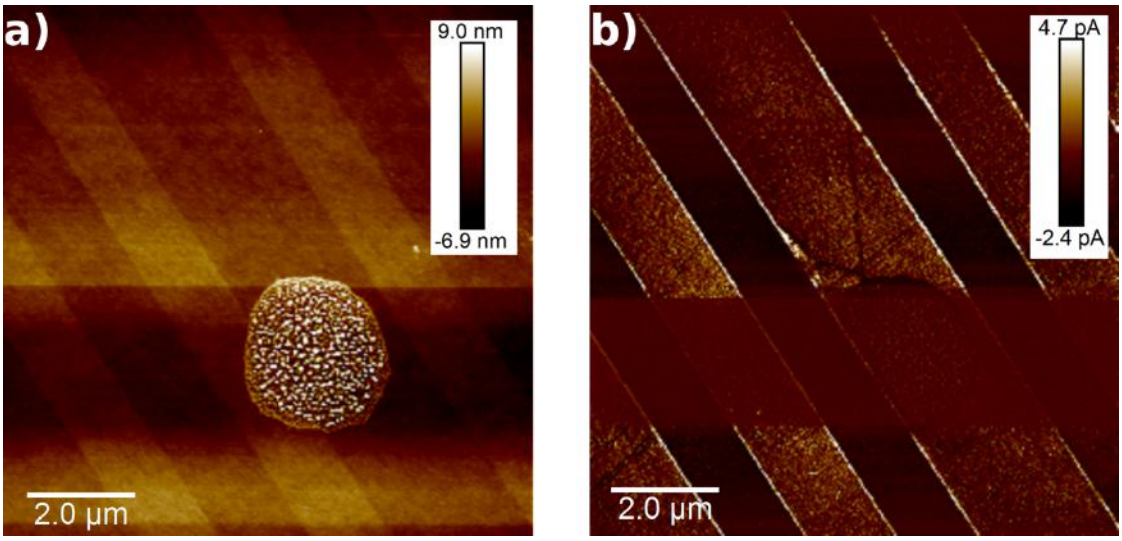

Figure 5.6: (a) Topography and, (b) TUNA maps showing the influence of sample contamination

Still another source of errors is electrical noise from the environment. The conducting tip acts as an antenna picking up electromagnetic radiation in the background, particularly 50 Hz noise from unshielded electronics. To minimize the noise the TUNA measurements were carried out inside a metal chamber, working as a Faraday cage. However, despite this precaution, electrical noise with 50 Hz frequency could be seen in most measurements.

When analyzing CAFM measurements, care must be taken to account for the capacitance of the cantilever [20]. As the bias between the tip and the sample varies, this capacitance will contribute to the measured current according to,

$$I_{capacitance} = C \cdot \frac{dV}{dt} \tag{5.01}$$

where C is the tip capacitance, commonly in the pF range. At a typical sweep-rate of around 1 V/s the capacitive contribution is thus on the pA level, a significant contribution to the measured current. The capacitance can be calculated by acquiring IV-ramps and measuring the offset between the trace ($\frac{dV}{dt} > 0$) and the retrace ($\frac{dV}{dt} < 0$) giving $C = \frac{\Delta I}{2} \cdot \left(\left| \frac{dV}{dt} \right| \right)^{-1}$. The known capacitance can then be used to compensate subsequent IV-curves.

5.2.4 Band Excitation PFM

In conventional PFM the frequency of the AC-bias is maintained constant, and the response is studied in a preset range around the resonance frequency. In order to study phenomena where the resonance frequency varies, a more advanced method is required. This thesis includes work with *band-excitation* (BE) PFM. The work was performed in collaboration with the Center for Nanophase Materials Sciences at Oak Ridge National Laboratories (USA) where the technique was first developed in 2007 [21]. The strength of the BE method is its ability to quickly record the system-response over an extended frequency-range. At each measurement point the tip is excited by a waveform containing a range of frequency components around the resonance frequency and the system-response is recorded. By fitting the measurement to a harmonic oscillator model, the frequency and amplitude response can be extracted, providing information on the local mechanical characteristics over the probed frequency-range. The ability to acquire a large number of measurements in a limited amount of time means that the effect of a slowly varying external parameter, such as an electric bias, can be studied by acquiring a series of BE responses. BE-PFM spectroscopy has been used to, among many other things, detect phase transitions at the nanoscale [22], study domain wall dynamics in ferroelectric bilayers [23], and investigate elasticity-modulation in proton conductors [24]. In the experiments reported in paper V this tool was used to study the variation of the resonance frequency, and thus the elastic modulus, induced by an external DC bias.

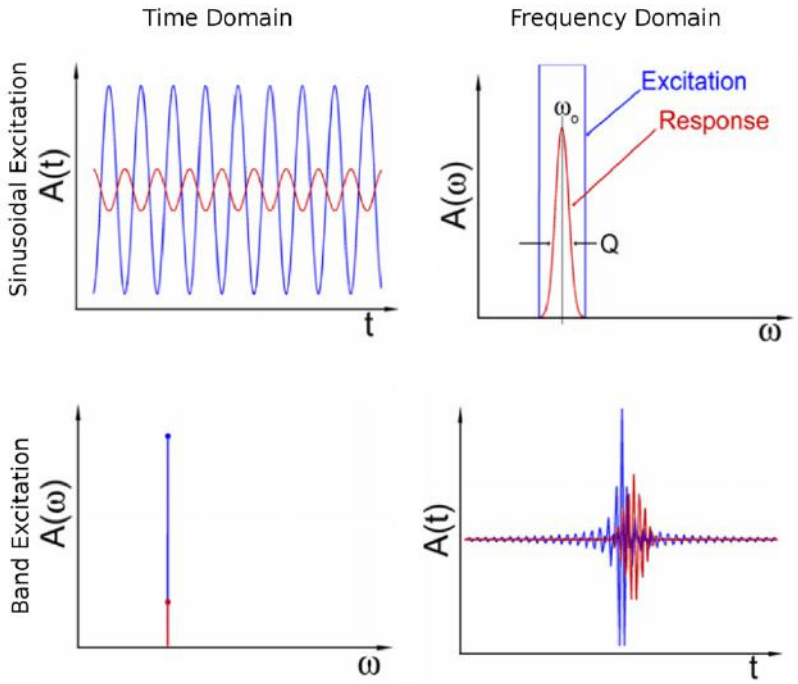

Figure 5.7: Working principle of the BE technique [21]

5.2.5 Time of Flight Scanning Ion Mass Spectrometry

While AFM-based methods provide ample information on the mechanical properties of the studied system, it is difficult to such methods to discern which chemical species are involved in a particular interaction. For this purpose, time-of-flight scanning ion mass-spectrometry (ToF-SIMS) [25], which is a highly sensitive chemical analysis technique, was used together with BEPS in order to get detailed information on the ionic and defect distribution in KTP. ToF-SIMS can provide molecular density mapping over a surface with a lateral resolution of around 100 nm. Since the method is capable of detecting the concentrations of many different species in parallel it is an ideal tool for finding spatial correlations and is used in many different fields from biology [25] to materials science [26].

In this technique a focused ion beam is scanned across the sample surface causing emission of secondary ions and clusters. The masses and quantities of the secondary ions are analyzed by comparing their time-of-flight through a series of electrostatic analyzers. Once the masses are known, the chemical contents of each ion or cluster can be determined by comparison with spectroscopic reference-data and a map of the concentration of each species can be obtained from the intensity of the signal at each point. By using the ion beam to sputter the material, the concentration can also be mapped as a function of the depth enabling the acquisition of 3D maps with a sub-nanometer vertical resolution. The ToF-SIMS measurements presented here were acquired at the Oak Ridge National Laboratories, using their ToF-SIMS system with integrated PFM capabilities in the same vacuum chamber, allowing the chemical data to be matched with PFM maps of the domain structure.

References to Chapter 5

[1] R. C. Miller and A. Savage, "Velocity of Sidewise 180° Domain-Wall Motion in $BaTiO_3$, as a Function of the Applied Electric Field", Phys. Rev. **112** (1958).

[2] K. Nassau, H. J. Levinstein, and G. M. Loiacono, "Ferroelectric Lithium Niobate. 1. Growth, Domain Structure, Dislocations and Etching", J. Phys. Chem. Solids, **27**, 983 (1966).

[3] F. Laurell, M. G. Roelofs, W. Bindloss, H. Hsiung, A. Suna, and J. D. Bierlein, "Detection of ferroelectric domain reversal in KTiOPO4 waveguides," J. Appl. Phys. **71**, 4664 (1992).

[4] R. C. Miller and A. Savage, "Velocity of Sidewise 180° Domain-Wall Motion in BaTiO3 as a Function of the Applied Electric Field," Phys. Rev. **112**, 755 (1958).

[5] G. Binnig, H. Rohrer, Ch. Gerber, and E.Weibel, "Surface Studies by Scanning Tunneling Microscope", *Phys. Rev. Lett.* **49**,57, (1982).

[6] G. Binnig, C. F. Quate, and Ch. Gerber, "Atomic Force Microscope", *Phys. Rev. Lett.* **56**, 930 (1986).

[7] J. Shim and D. Gweon, "Piezo-driven metrological multiaxis nanopositioner", Review of Scientific Instruments **72**, 4183 (2001).

[8] Y.Gan,"Atomic and subnanometer resolution in ambient conditions by atomic force microscopy", Surf. Sci. Rep. **64**, 99–121 (2009).

[9] A. Gruverman, O. Auciello, and H. Tokomuto, "Scanning force microscopy for the study of domain structure in ferroelectric thin films", J. Vac. Sci Technol. **14**, 602 (1996).

[10] T. Jungk, Á. Hoffmann, and E. Soergel, "Quantitative analysis of ferroelectric domain imaging with piezoresponse force Microscopy", Appl. Phys. Lett. **89**, 163507 (2006).

[11] S. Kalinin and A. Guverman,"Scanning Probe Microscopy: Electrical and Electromechanical Phenomena at the Nanoscale", Springer (2007).

[12] Bruker, "PeakForce TUNA Nanoelectronical Application Module", (2010).

[13] J. Seidel, L.W. Martin, Q. He, Q. Zhan, Y.H. Chu, A. Rother, M.E. Hawkridge, P. Maksymovych, P. Yu, M. Gajek, N. Balke, S.V. Kalinin, S. Gemming, F. Wang, G. Catalan, J.F. Scott, N.A. Spaldin, J. Orenstein, and R. Ramesh,"Conduction at domain walls in oxide multiferroics", Nat. Mater. **8** (3), 229 (2009).

[14] P. Maksymovych, A.N. Morozovska, P. Yu, E.A. Eliseev, Y.H. Chu, R. Ramesh, A.P. Baddorf, and S.V. Kalinin, "Tunable Metallic Conductance in Ferroelectric Nanodomains", Nano Lett. **12**, 209 (2012).

[15] H.S. Huang , H.M. Cheng, L.J. Lin, ”Coating tips used in electrical scanning probe microscopy with W and AuPd”, Appl. Surf. Sci., **252**, 2085 (2005).

[16] S. Rozhok, P. Sun, R. Piner, M. Lieberman, and C. A. Mirkin, “AFM Study of Water Meniscus Formation between an AFM Tip and NaCl Substrate”, J. Phys. Chem. B, **108**, 7814 (2004).

[17] L. Aguilera, W. Polspoel, A. Volodin, C. Van Haesendonck, M. Porti, W. Vandervorst, M. Nafria, and X. Aymerich, ”Influence of vacuum environment on conductive atomic force microscopy measurements of advanced metal-oxide-semiconductor gate dielectrics”, J. Vac. Sci. Technol. B, **26**, 1445 (2008).

[18] E. Strelcov, S.M. Yang, S. Jesse, N. Balke, R.K. Vasudevan, and S.V. Kalinin, “Solid-state Electrochemistry on the Nanometer and Atomic Scales: the Scanning Probe Microscopy Approach”, Nanoscale, **8**, 13838 (2016).

[19] S.V. Kalinin, A.N. Morozovska, L.Q. Chen, and B.J. Rodriguez, “Local polarization dynamics in ferroelectric materials”, Rep. Prog. Phys **73**, 056502 (2010).

[20] M. Rommel, J. D. Jambreck, M. Lemberger, A. J. Bauer, L. Frey, K. Murakami, C. Richter, and P. Weinzierl, “Influence of Parasitic Capacitances on Conductive AFM I-V Measurements and Approaches for its Reduction”, J. Vac. Sci. Technol., B: Nanotechnol. Microelectron.: Mater., Process., Meas., Phenom. **31**, 01A108 (2013).

[21] S. Jesse, S. V. Kalinin, R. Proksch, A. P. Baddorf, B. J. Rodriguez, “The band excitation method in scanning probe microscopy for rapid mapping of energy dissipation on the nanoscale”, Nanotechnology, **18,** 43, 435503 (2007).

[22]R. K. Vasudevan , H. Khassaf , Y. Cao , S. J. Zhang , A. Tselev , B. Carmichael, M. B. Okatan, S. Jesse, L. Q. Chen, S. P. Alpay, S. V. Kalinin, and N. Bassiri-Gharb, “Acoustic Detection of Phase Transitions at the Nanoscale”, Adv. Funct. Mater. **26**(4), 478 (2016).

[23] V. Anbusathaiah, S. Jesse, M.A. Arredondo, F.C. Kartawidjaja, O.S. Ovchinnikov, J. Wang, S.V. Kalinin, V. Nagarajan, “Ferroelastic Domain Wall Dynamics in Ferroelectric Bilayers”, Acta Mater. **58**, 5316 (2010).

[24] A. Papandrew, Q. Li, M. Okatan, S. Jesse, C. Hartnett, S. Kalinin, and R. Vasudevan, ”Electrocatalysis-Induced Elasticity Modulation in a Superionic Proton Conductor Probed by Band-Excitation Atomic Force Microscopy”, Nanoscale **7**(47), 20089 (2015).

[25] L.A. McDonnell and R.M.A. Heeren, “Imaging mass spectrometry”, Mass Spectrom. Rev. **26**, 606 (2007).

[26] A. V. Ievlev, P. Maksymovych, M. Trassin, J. Seidel, R. Ramesh, S. V. Kalinin, and O. S. Ovchinnikova, ”Chemical state evolution in ferroelectric films during tip-induced polarization and electroresistive switching”, ACS Appl. Matt. Interf. **8**, 29588 (2016).

6. Optimization of Periodic Poling

6.1 Periodic Poling

6.1.1 Processing Steps

The steps involved in fabrication of periodically poled QPM gratings are illustrated in figure 6.1. The as purchased wafers are typically 1 mm thick along the polar axis with a surface area of 30 x 30 mm^2. Before processing, the wafers are cut into smaller parts in order to ensure homogeneous conductivity over the whole surface of each sample. Since the preferential orientation of the domain walls in KTP isomorphs is in the crystal *a*-plane, the grating-vector and the direction of light propagation are also chosen along this axis. Therefore, the wafers are cut into rectangular samples with the longer edge along the *a*-axes; typical dimensions are 12 x 7 x 1 mm^3 along the *a*-, *b*- and *c*- axes respectively. The *a*-faces are then polished to allow distortion-free light propagation.

Standard contact photolithography is used to create a periodic photoresist pattern with the desired periodicity on the crystal c- face. Subsequently, a metal layer is deposited on top of the photo-resist, forming a periodic electrode where the photoresist serves as an electric insulator. Finally, the sample is contacted to the poling circuit using liquid KCl electrodes and one or several electric field pulses are applied across the sample, causing polarization inversion in the electrically contacted area.

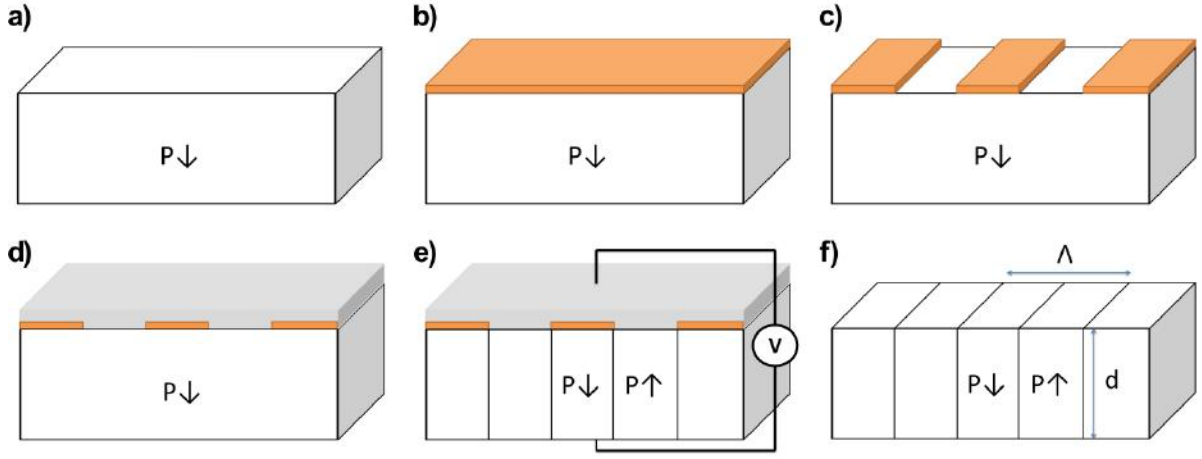

Figure 6.1: Overview of the periodic poling process, (a) the crystal wafer is cut into samples of suitable size, (b) photo-resist spinning, (c) UV-lithography, (d) metal-deposition, (e) polarization reversal, (f) mask removal

While a homogeneous and defect-free electrode structure is necessary, the main challenge is usually the poling step. The *aspect ratio*, i.e. the quota between the crystal thickness *d* and the grating period Λ, approaches 1000 for typical domain periods in the micrometer range and a

standard crystal thickness of 1 mm. In order to achieve a high quality grating, the sideways domain expansion must therefore be minimal in comparison to the forward growth.

6.1.2 Polarization Reversal Under Periodic Electrodes

When using periodic electrodes, the field is not homogeneous across the polar face. The sharp delineations between the conductive aluminum stripes and the insulating photoresist cause *fringing fields* to appear; the field is locally enhanced in the polar direction while at the same time acquiring an otherwise absent component in the *a*-direction [1]. The enhancement of the vertical field causes preferential nucleation along the electrode edge. The transversal field component contributes to charge injection under the photo-resist insulator, causing *domain broadening*, i.e. an unwanted deviation from the desired duty-cycle due to the lateral expansion of the inverted region.

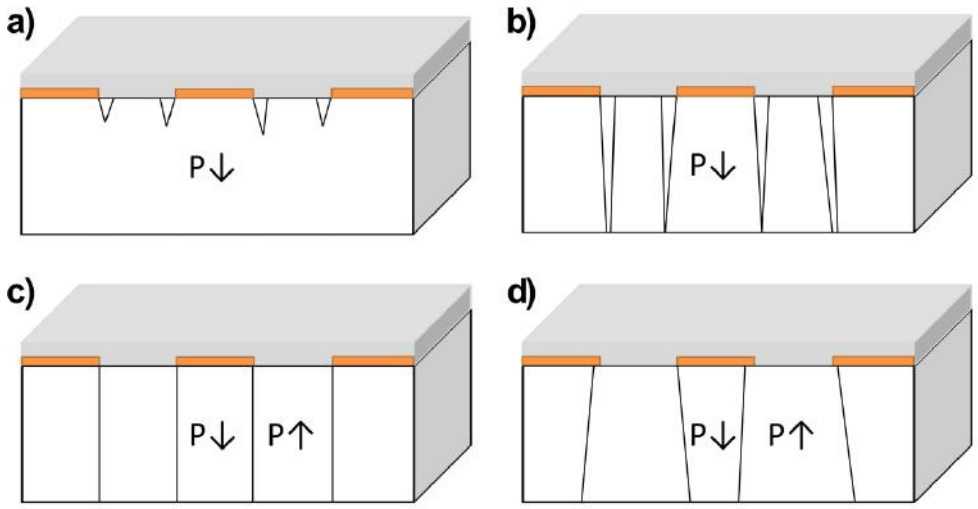

Figure 6.2: Domain nucleation and growth in periodic poling

The ideal periodic poling conditions thus become a balance between achieving sufficient domain coalescence to avoid the domain structure settling in the state of figure 6.2 b, known as *underpoling*, while at the same time avoiding excessive broadening leading to *overpoling* as shown in figure 6.2 d. Further complicating the matter, a spatially varying crystal stoichiometry or electrode-quality may lead to different parts of the sample reaching the different stages at different times.

6.2 Polarization Reversal Dynamics

As discussed in chapter 4, RKTP has excellent periodic poling properties. Therefore, this isomorph was chosen for a series of experiments investigating the domain formation dynamics. The online SHG technique, describe in chapter 5 was used to visualize the domain growth in the high field regime, that is known to give the best results in KTP isomorphs [2]. Therefore, a pulse-length of 5 ms was used throughout the experiment and periodic poling was performed with two basic pulse shapes: symmetrical triangular and square pulses. As a first example, the results of varying pulse-magnitude resulting in *underpoling*, *grating-poling* and *overpoling* are shown in figure 6.3.

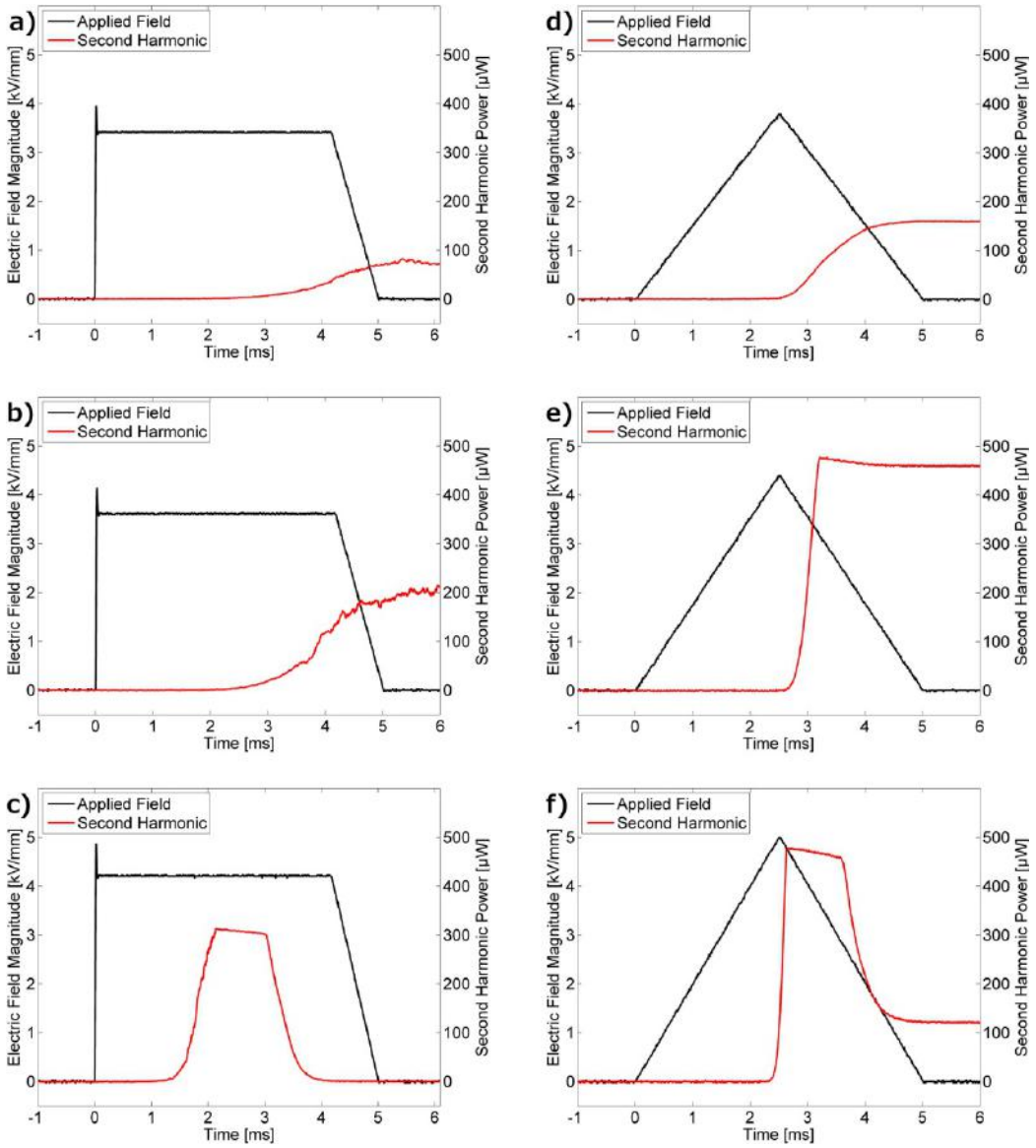

Figure 6.3: Applied E-field (black curves) and second harmonic traces (red curves) for the cases of (a) underpoling, (b) grating poling, and (c) overpoling, using square pulses, and (d) underpoling, (e) grating poling, and (f) overpoling, using triangular pulses.

As seen in the figure, several features are common to all the poling events. First, there is a certain "incubation time", (t_i), where the SH signal stays at the noise level. We define t_i as the time from the start of the voltage pulse until the SH signal reaches 5% of its peak value. The SH signal growth is represented by the "rise time" (t_r) and is defined in our experiments as the time it takes for SH signal to rise from 5% to 90% of its peak value. For the *overpoling* cases, two additional features can be observed: a "dwell time" (t_d) – here defined as the time, while the SH signal stays above 95% of its peak value, followed by the "fall time" (t_f), defined as the time it takes for SH signal to decrease to below 5% of its peak value.

Table 6.1 summarizes representative values obtained in *underpoled*, *grating-poled* and *overpoled* crystals using single, 5 ms-long square or triangular E-field pulses corresponding to figure 6.3(a)-6.3(f). As can be seen from the table, all poling cases studied here display incubation times in the range of a few ms. The *rise times* obtained using triangular pulses are much shorter than those corresponding to square pulses; particularly for the case of *grating poling*. The dwell times on the order of one ms with sub-ms fall times are observed in *overpoled* samples both for square and triangular pulses.

Pulse type	Poling regime	Peak poling field, $kVmm^{-1}$	t_i, ms	t_r, ms	t_d, ms	t_f, ms	Maximum SH power, μW
Square	*Underpoling*	3.4	2.73	2.19	-	-	82
	Grating-poling	3.6	2.79	2.07	-	-	220
	Overpoling	4.2	1.46	0.60	0.99	0.68	313
Triangular	*Underpoling*	3.8	2.62	1.41	-	-	161
	Grating-poling	4.2	2.56	0.34	-	-	459
	Overpoling	5.0	2.41	0.19	0.98	0.73	478

Table 6.1: Comparison of typical characteristics for varying pulse-shape and peak E-field

The different features of the SH traces reflect different stages of the poling process discussed in section 6.2 as will be shown below.

Incubation time

In order to understand the physical meaning of the incubation time and its apparent weak dependence on the electric pulse shape, we poled several crystals with E-field pulses shorter than the expected incubation time. This was done for both square and triangular pulses, using pulse lengths of up to 90% of the expected incubation times. The voltage was turned off rapidly at the end of each pulse. For all cases, a rectifying diode was added to the poling circuit in order to prevent possible domain back-switching. Finally, the crystals were selectively etched.

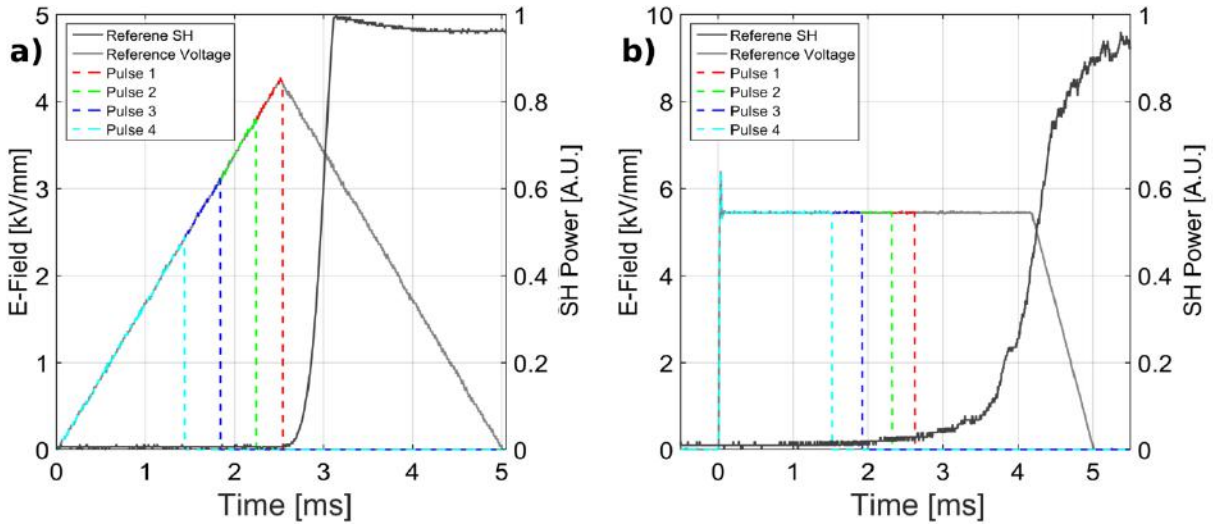

Figure 6.4: Pulse shapes used for studying the incubation time for (a) triangular pulse-shape and (b) square pulse-shape.

No domain nucleation on the polar surfaces of the etched crystals could be observed for any of the investigated crystals. Therefore, we conclude that the incubation time can be attributed to the time needed to form critical domain nuclei, which will then stabilize and grow only if the field continues to be applied. The existence of an incubation time has been previously reported for several other materials such as lithium tantalate [3] and KTP [4], and was similarly attributed to critical-nuclei formation and stabilization time.

Although we do not have enough statistical data to determine the exact dependence of the incubation time on the E-field, it is obvious that the incubation time decreases when increasing the E-field magnitude, being as short as 1.46 ms for a square pulse of 4.2 $kVmm^{-1}$. For triangular pulses, we also see a sharp decrease in incubation time when we increase the ramp rate. For instance, ramping up the voltage at 1.52 $kVmm^{-1}ms^{-1}$ resulted in 2.62 ms incubation time (corresponding to 3.6 kV/mm field strength); when the ramp rate was increased to 2.0 $kVmm^{-1}$ ms^{-1} the incubation time decreased to 2.41 ms (at 4.8 kV/mm field strength). For triangular pulses, the interpretation of the incubation time is somewhat more complicated as the E-field varies, and since measurable SH is often first detected after the peak E-field. In both cases, it can be attributed to an increase in nucleation probability at larger E-fields. Nevertheless, it is worth noting that the incubation time *per se* seems to have little influence on the quality of the QPM structure.

Rise time

The detection of SH signal during poling begins when a sufficient amount of reversed domains crosses the probe beam path in the crystal, and reaches maximum when the QPM grating has the optimal duty-cycle. The following observations can be made: (1) Both for square and triangular pulses, the rise time decreases when the E-field magnitude is increased (see table I); (2) For *grating poling*, the rise times for triangular pulses are in the sub-ms regime and an order of magnitude shorter than for square pulses: The rise time for square pulses ranges between 1.12 ms and 2.87 ms (the variation in rise time is 1.75 ms) when the E-field varies from 5 $kVmm^{-1}$ to 3.6 $kVmm^{-1}$, whereas for triangular pulses the rise time changes from 0.22 ms to 0.40 ms (0.18 ms variation) when the ramping rate changes from 2.08 $kVmm^{-1}ms^{-1}$ to 1.76 $kVmm^{-1}ms^{-1}$. (3) Poling with triangular pulses gives QPM gratings of higher quality than poling with square pulses, as can be seen in figure 6.5, showing etched domain patterns corresponding to the poling events in figure 6.3(a-f).

Moreover, this fact is also confirmed by the significantly higher normalized conversion efficiencies obtained in PPRKTP crystals poled with triangular pulses, compared to those obtained in the crystals poled with square pulses, (see Table 6.1), and in good agreement with previous reports [5].

All these observations can be interpreted in the following way: Since no domain formation occurs during the incubation time, the rise time should account for most of the polarization–switching process; domain nucleation, propagation in the polar direction and coalescence under the metal electrodes. The SH signal increases when there is growth of new periodic domains in the sampled volume. Thus, a long rise time indicates that the formation of individual domains is more spread out in time, i.e., some domains are still in the nucleation stage, while others have already been formed and propagated through the sample. On the other hand, a short rise time suggests a more uniform formation of the QPM structure; i.e., most domains nucleate and grow at the same pace.

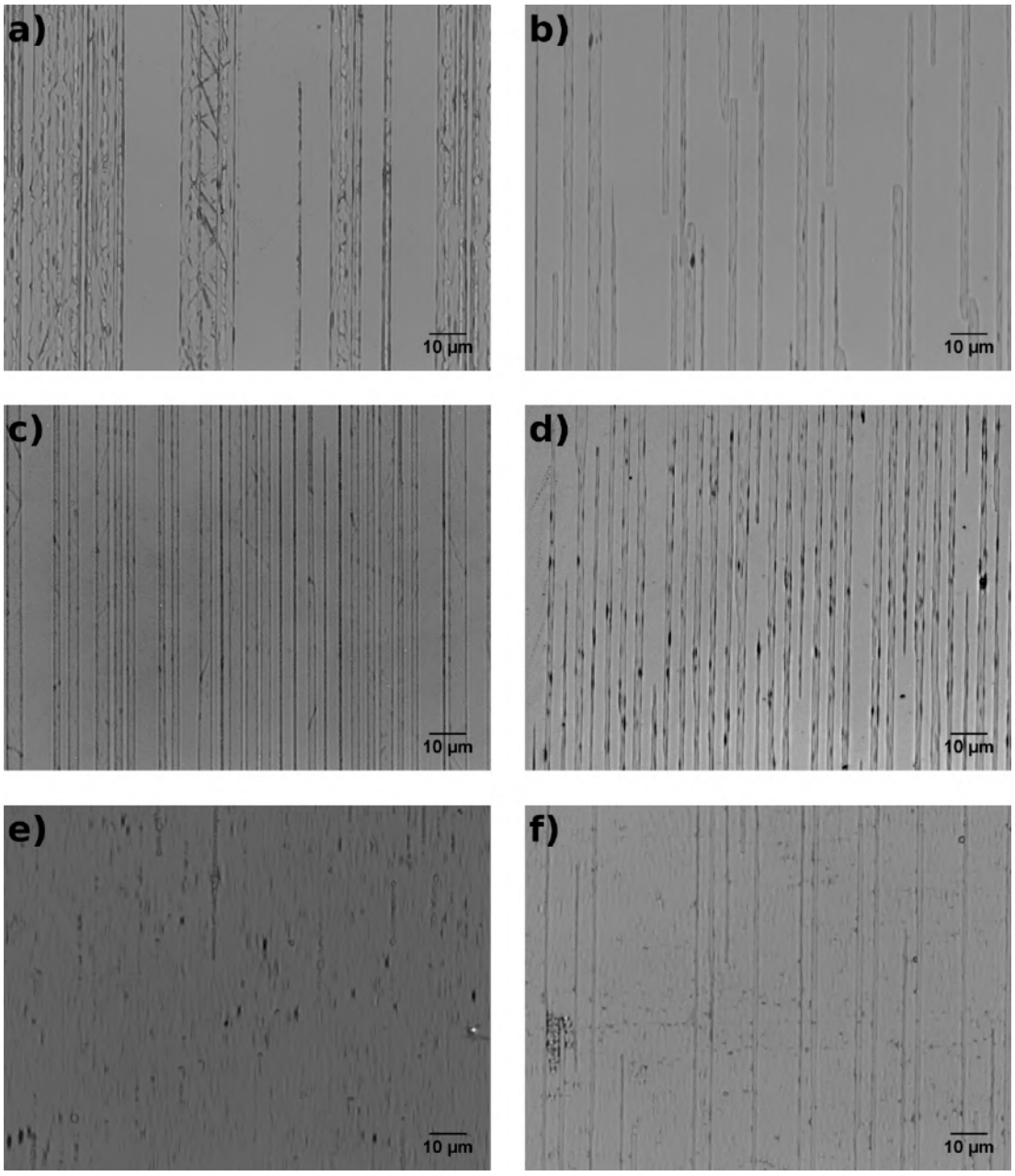

Figure 6.5: Chemically etched domain structures on the original c+ face, corresponding to the poling events of figure 6.3

As mentioned at the beginning of this chapter, the switching process is nucleation-limited in the low field regime (i.e., E-fields below the coercive field), while at high fields (i.e., higher than the coercive field), the nucleation is not a limiting factor any more, and the switching is governed by the domain wall motion [6]. For triangular pulses, the majority of domain nucleation takes place at the vicinity of the peak of the pulse (high-field regime), where the nucleation rate is the highest, followed by growth of these simultaneously nucleated domains. In addition, the non-constant field ensures nucleation in the regions of the crystals that, due to deviation from

stoichiometry and/or defects might have slightly larger coercive field. Moreover, since sideways domain expansion occurs via nucleation and growth of step-like domains adjacent to already existing domain walls [7], domain broadening is only likely to occur within the short time near the peak of the E-field pulse. Consequently, a more uniform QPM grating is formed, which is well-reflected by a relatively short SH rise time. On the other hand, for square pulses, constant E-field throughout the duration of the pulse provides constant nucleation probability; however, regions within the crystal with slightly different coercive field will have different nucleation rates. Thus, nucleation of individual domains is spread in time during the pulse, resulting in overall less homogeneous QPM grating, which is reflected by an order of magnitude longer rise time, compared to triangular pulses.

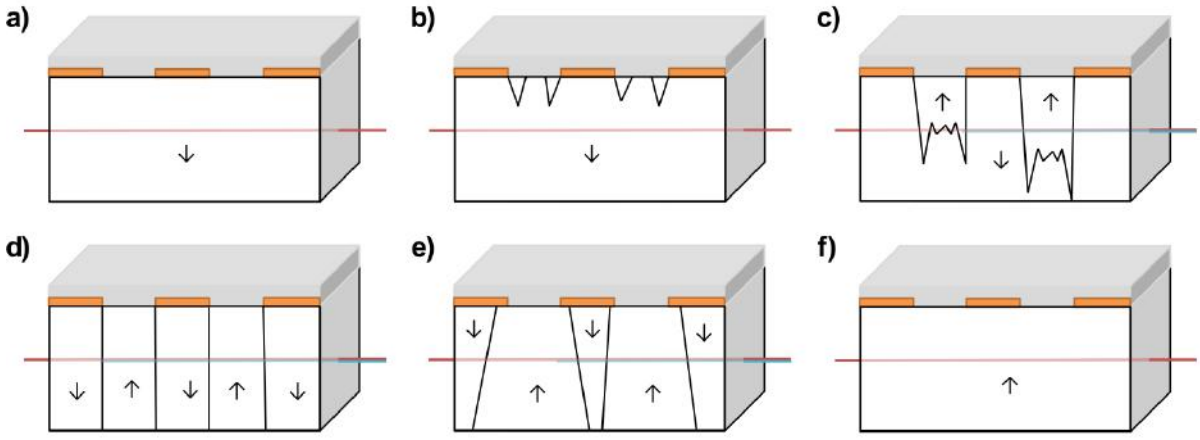

Figure 6.6: Stages of domain reversal and their relation to the SH traces

Dwell and fall times

In the case of *overpoled* crystals, there is a certain "dwell time", a period of around one millisecond during which the SH signal stays at its maximum value, indicating that there is no domain broadening during this time, at least in the sampled volume. The dwell time can be attributed to the time needed to nucleate new domains under the photoresist, which will naturally be slower due to the limited charge injection under the insulating photoresist layer. If the applied field is not switched off after the SH reached its peak value, domain nucleation, growth and merging under the insulating photoresist layer eventually occurs, causing deviations from the ideal duty cycle in the QPM grating, with the corresponding decline of SH signal. The SH fall time indicates how fast the transition from a periodic domain structure to an almost single domain state occurs.

Multiple Pulses

We also studied the switching behavior when poling was performed using multiple pulses. Figure 6.7(a) shows the results of using multiple square pulses with 3.4 $kVmm^{-1}$ peak magnitude (low-field regime). The waiting time between pulses was 1 min. The first applied pulse resulted in an incubation time of 3.32 ms, while the SH signal was rising instantly with the beginning of the subsequent pulse. The maximum SH output power reached 263 μW in this case.

An example of the SH signal evolution when using multiple triangular pulses is shown in figure. 6.7(b). The peak of each pulse was set to 3.8 $kVmm^{-1}$, with 1 min waiting time between pulses. Although there is always some incubation time in the beginning of each applied pulse, the field at which the SH signal begins to change, decreases with each subsequent pulse. In this case, the maximum SH output power reached 48 μW, before decreasing to approximately half. While the examples shown in figure 6.7 are achieved with three pulses, experiments with lower E-field magnitude and more pulses lead to qualitatively the same results.

In terms of QPM grating quality and conversion efficiency, these results indicate that there is essentially no difference between poling with single and multiple square pulses. The fact that the incubation time can be observed only during the first applied square pulse suggests that the polarization switching within a subsequent applied pulse resumes from the state it has reached when the previous pulse has ended. This is in good agreement with previous studies on KTP [4] and differs substantially from the behavior of lithium tantalate; where there is always certain incubation time, needed to unpin the existing domain walls [7].

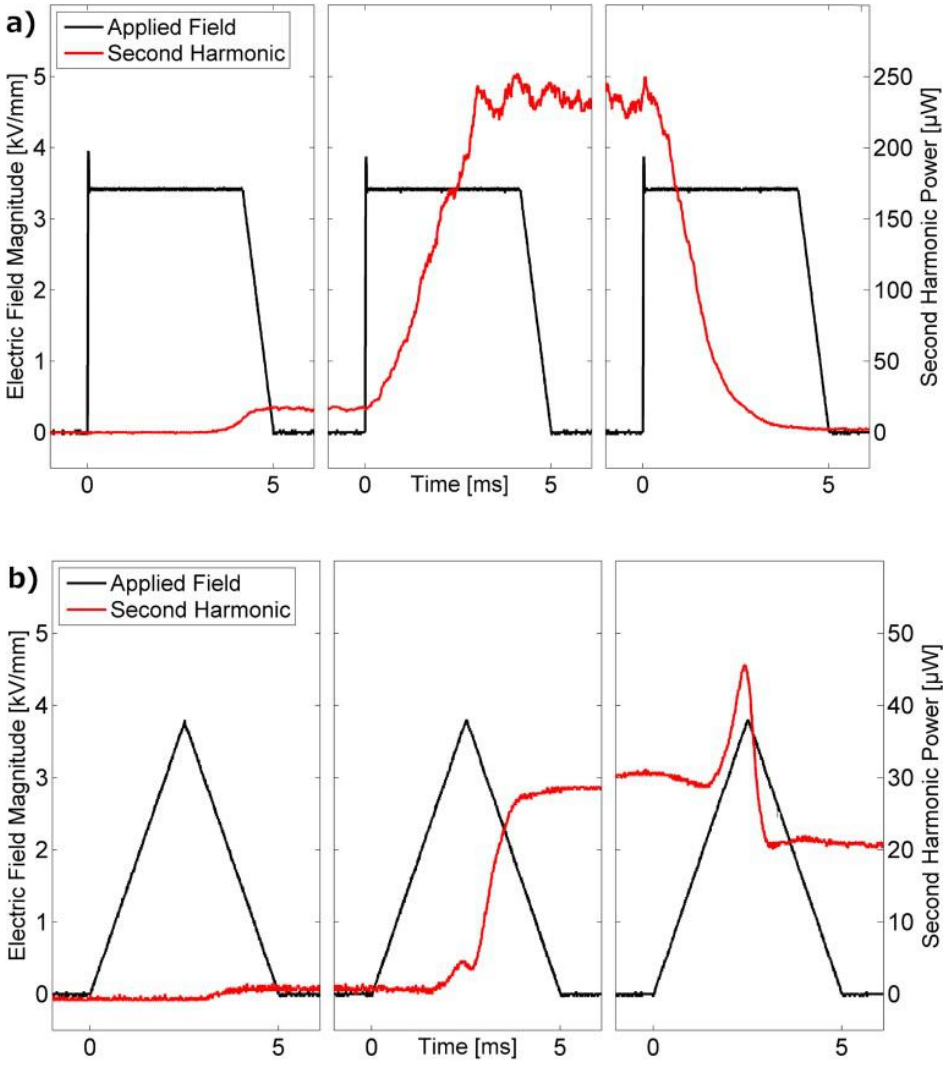

Figure 6.7: Second harmonic signal evolution (red) and applied E-field (black) during periodic poling with multiple square (a) and triangular (b) pulses.

In contrast, periodic poling with multiple triangular pulses results in less homogeneous domain structures and lower conversion efficiency, compared to poling with a single triangular pulse. In this case, the polarization switching takes place in the low-field nucleation-limited regime. In addition, even though the domain nucleation rate is still highest at the peak of the triangular E-field pulse, now the domain formation is divided between multiple triangular pulses, promoting new domain nucleation in unwanted regions and leading to domain broadening, and therefore, the benefit of using the triangular pulse shape is lost.

Estimation of the domain velocity along the polar axis

It is known that the domain propagation speed along the polar axis is much higher than in any direction in the ab-plane. However, determining this speed in the high-field regime is difficult, due to the short timescales involved. Canalias et al [8] used the Miller and Savage technique to determine domain speed in KTP along the *a*-, *b*-, and *c*-axes at fields up to 2.2 kV/mm, corresponding to the high-field regime for the samples used. They found that in this field-range, the speed along the polar axis is at least 2 orders of magnitude higher than in any perpendicular direction. Along the polar axis, the speed was determined to be approximately 0.23 m/s at 2.2 kV/mm. However, as they pointed out this figure is to be understood as a lower bound, due to the technique used.

In order to estimate the domain propagation speed along the polar axis in RKTP, two pairs of crystals were poled while launching the probe beam close to one of the polar faces. To ensure that the material characteristics were as similar as possible, each pair consisted of two crystals cut from the same part of the wafer along its *b*-axis and next to each other along the *a*-axis. Within each pair both crystals were poled using the exact same peak field and pulse length, orienting the probe beam close to the patterned face in one crystal and close to the un-patterned face in the other. Figure 6.8 shows the electric field pulses and the resulting SH traces. It should be noted that crystals from a different boule, with a higher coercive field, were used for the remainder of the experiments.

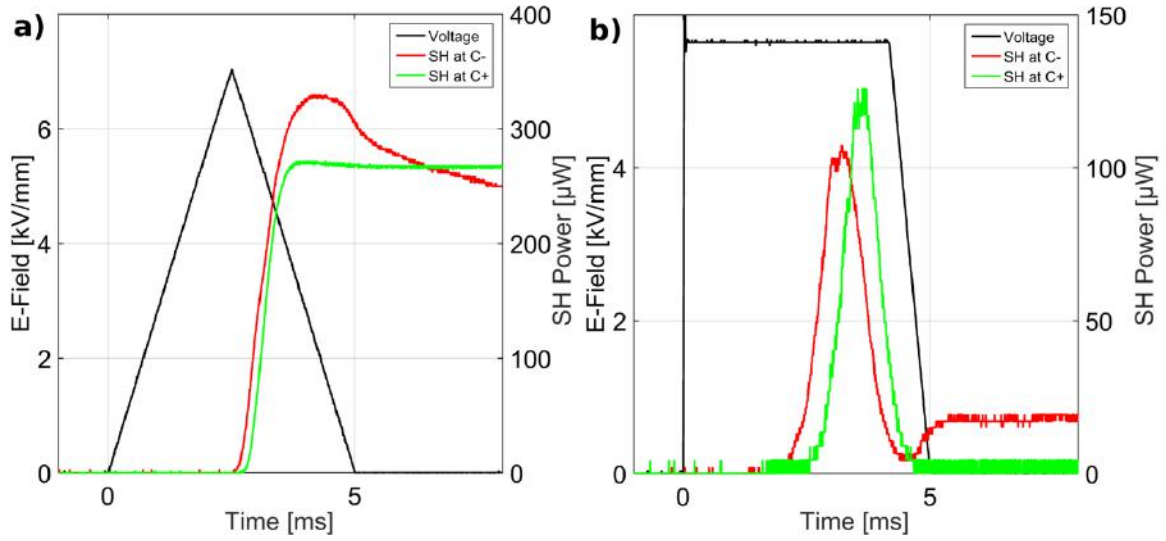

Figure 6.8: Applied E-field (black curves), second harmonic traces close to the patterned face (red curves) and second harmonic traces close to the un-patterned face (green curves) for (a) triangular pulse shape and (b) square pulse shape

For the triangular pulses of figure 6.8(a), an E-field pulse with 7.0 kV/mm peak magnitude, expected to result in high quality gratings was chosen in order to maximize the detected signal. As expected the SH was detected earlier close to the *c*- face; the average difference measured

during the part of the traces corresponding to the rise-time was 0.14 ms. The center-points of the beams were separated by 0.88 mm giving an estimated domain propagation speed of 6.3 m/s. For the second measurement, a square pulse shape with a magnitude of 5.6 kV/mm was used. This time the pulse magnitude was chosen to cause substantial overpoling with the aim of getting well-defined SH pulses with steep leading edges. The average temporal separation between the two traces of figure 6.8(b) was 0.44 ms; together with the measured spatial separation of 0.86 mm this gives an estimated domain propagation speed of 1.96 m/s.

The speed obtained using triangular pulses is three times higher than that of the square pulses. This can be attributed to the different field strengths used in these two cases. As discussed earlier, the majority of the time before any SHG is registered corresponds to the time needed to form stable nuclei on the patterned face. The subsequent forward growth is a much faster process. In the case of the triangular pulses, the forward growth occurs close to the peak field and is therefore expected to be much faster than in the case of the square pulses, as the growth speed is highly dependent on the field strength [8].

For both cases, the speeds measured here are an order of magnitude higher than the previously reported lower bounds reported for KTP. While it is clear from this study that domain propagation along the polar axis is very fast, it is difficult to determine the velocity with exactitude; the present measurement is dependent on the two crystals of each pair having sufficiently similar characteristics, both in terms of crystal stoichiometry and of electrode quality. However, the measurement does demonstrate the strength of this technique when it comes to detection speed. In a future improved study, two parallel beams could be employed, allowing much more precise detection.

A surprising feature of figure 6.8 is the evolution of the SH traces during the latter parts of the applied pulses. In case of the trace at *c*- in figure 6.8(a), there is a gradual decline of the signal after the pulse has ended. Similarly in figure 6.8(b) the trace obtained at *c*- declines to a low value towards the end of the pulse and then partially recovers. This could be attributed to wavelength instability from the pump-source.

6.3 Investigation of Grating Stability at High Temperature

It is clear that the proper choice of poling conditions can mitigate the problems associated with domain propagation, enabling the creation of QPM devices with high-quality domain gratings. However, as mentioned in the chapter 4, there is also a newly developed alternative approach in which a domain grating is inscribed in the crystal upon growth through the use of a periodically poled seed crystal or *template*. This technique still requires a periodically poled template; however the template can be thin, thus lowering the aspect ratio of the grating that needs to be fabricated using periodic poling. While this greatly simplifies the poling, the template growth takes place at high temperature and the thermal stability of the domain grating of the template and in the growth region becomes crucial to ensure homogeneous growth. There has been a few studies on the grating stability in KTP [9, 10], however, they were performed close to the Curie temperature (940° C) whereas the template growth takes place between 700° C and 750° C. Furthermore, because of its superior optical and periodic poling properties, RKTP is an interesting candidate for template growth of periodic gratings. High temperature treatment of periodic gratings is also interesting for other post-poling fabrication processes such as the creation of waveguides through ion exchange or for removing gray tracks.

Therefore, we investigated the high temperature stability of the domain structures in RKTP, in the temperature range of interest for template growth. Several gratings with different period and grating homogeneity were annealed for varying amounts of time. Most of the experiments took place at 730 °C, since this is the temperature used for epitaxial growth using a periodically poled crystal as a template. Furthermore, for crystals with a 9 μm period annealed for 4.5 h, no changes of the domain structure were observed for temperatures below 550 °C. Gratings annealed at 800 °C and above showed severe backswitching and were therefore not suitable for understanding domain-wall dynamics.

Figure 6.9 shows a representative example of the domain wall motion in a grating with 9 μm resulting from 4.5 h annealing at 730 °C. Figures 6.9(a and b) show optical microscope images of double-relief structures obtained by selective etching on the former *c*- and *c*+ faces respectively. The pre-annealing DWs are seen as slightly dimmer lines, while the post-annealing walls appear sharper. The topography of figure 6.9(a) imaged by AFM, together with a higher magnification inset, can be seen in figure 6.9(c) and its corresponding PFM image in figure 6.9(d). Note that in the PFM image there is some topography cross-talk.

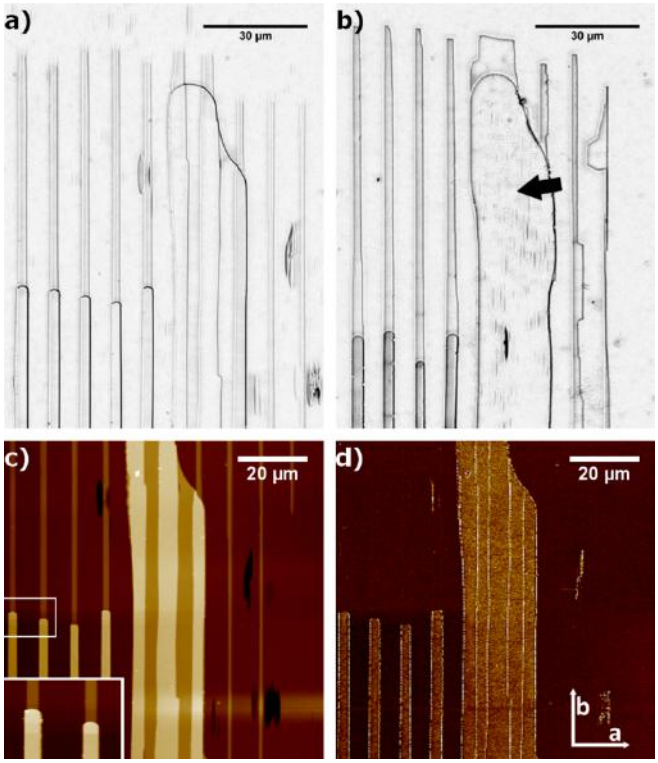

FIG. 6.9. Optical micrographs showing the etched domain structures on (a) the former c^-,and (b) c^+ faces; (c) AFM topography and (d) and PFM response of the etched structured shown in (a). The inset in figure 6.9(c) shows a higher magnification scan (18 x 12 μm^2) of the area marked by a white box in the figure.

The DW motion is anisotropic along the different crystallographic axes, and depends on whether the domains extend throughout the crystal thickness or merge in the bulk. In the case of domains extending throughout the crystal thickness, backswitching occurs along the *b*-axis. In figure 6.9, the average motion along the *b*-axis is 68 µm on the former c^- face and 90 µm on the former c^+ face, from the initial wall position to the final position. In contrast, DW motion along the *a*-axis is radically different: expansion by 0.4 µm on the former c^- face and contraction by 0.06 µm on the former c^+ face. Domains that were originally in a head-to-head configuration merge into larger domains, as in the case of the domain marked by an arrow in figure 6.9, and their contraction along the *b*-axis is substantially less than that of individual domains.

These observations can be explained in terms of energy-preferred DW orientation. During the annealing process, redistribution of bulk charges, out-diffusion of ions and/or reorientation of defect dipoles may create an internal field sufficient to move domain walls. The walls will move in ways that minimize their energy and/or overcome the activation energy for backswitching [11]. Any DW that deviates from 180° angle to the *c*-axis will be charged, and, therefore, it will have larger DW energy (Ew). It is known that DWs parallel to the (100) plane are energetically favorable, since these planes do not cut through the crystallographic helical chains [12]. Thus along the *a*-axis, the DW movement always occurs in a way that minimizes the angle with the

(100) plane. For domains that are originally in a head-to-head configuration, this results in domain merging with straighter walls.

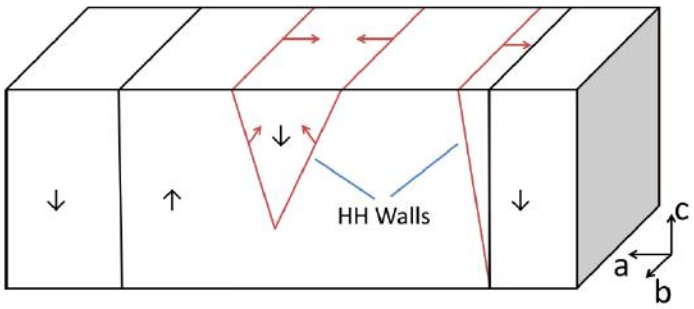

Figure 6.10: Metastable HH domain walls and their motion at high temperature

On the other hand, there is no evidence that minimization of the angle with the (010) plane is driving the process, indicating that the energy penalty for DWs at an angle with this plane is not severe. Nevertheless, contraction along the *b*-direction can be as much as tens of μm. This can be understood by taking into account that the DW velocity along the *b*-axis during electric filed poling is approximately 30 times larger than that along the *a*-axis, showing that the energy barrier for DW motion is lower along *b*-direction [13]. The fact that more DW displacement is observed on the former c^+ face can be attributed to the fact that domain nucleation in KTP isomorphs preferentially occurs on the c^- face [13] and thus backswitching starts from the c^- ends of the switched domains. It is worth noting that a difference in the DWs stability along their *X*- and *Y*-directions has also been reported for near-stoichiometric lithium tantalate (SLT) [11, 14] and near-stoichiometric lithium niobate (SLN) [15] where it was attributed to the fact that *Y*-walls have lower energy in these materials [16]. Similar to SLT, domains that exhibit sharp and rough edges (as the two rightmost domains of figure 6.9b) have high wall energy. Such walls are therefore very mobile, resulting in larger contraction (118 μm and 138 μm average displacement on the c^- and c^+ faces, respectively) or smoothening of the angles, as in the merged domain in figure 6.9. Reshaping of domains due to the higher propagation speed of rough walls was previously shown in lithium tantalate [17], where it was explained through the competition between the growth of steps and the formation of new steps at the domain wall.

Annealing Time

To study the effect of the annealing time several PPRKTP crystals with 9 μm period were annealed between 3 and 24 hours at 730°C. The average DW displacement along the *b*-axis on the former c^+ faces as a function of the annealing time is shown in figure 6.11. As expected, the DW displacement increases with time. However, the rate of contraction decreases as the annealing time increases, as seen clearly for annealing times over 9 hours. This can be understood by taking into account that the DWs are generally rougher and therefore more mobile at the start of the thermal process. As time passes the wall energy is reduced, causing a corresponding

reduction in the wall mobility as the wall reaches a metastable state. The higher average speed obtained for short annealing times is therefore due to the motion of rough walls with high energy, while the lower speeds observed at longer annealing time is the result of slow, metastable walls.

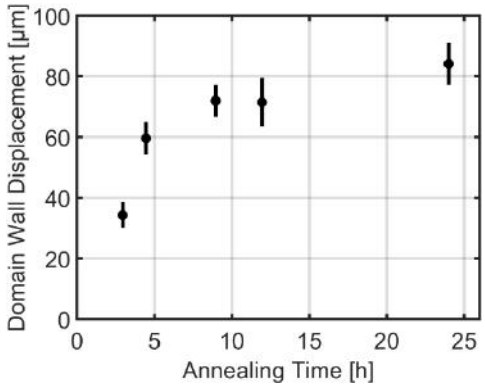

Figure. 6.11. Dependence of the DW displacement along the b-axis on the annealing time.

Remarkably, large merged domains, independently of whether the merging happens during electric field poling or during the thermal process, do not contract much even after 24h annealing.

Grating Period

In order to study the impact of the domain size on the thermal stability, several PPRKTP samples with periods of 2 µm, 5 µm, 9 µm and 36.4 µm, as well as several self-assembled RKTP (SARKTP) [18] with average period 650 ±200 nm, were annealed for 4.5 h at 730 °C. Figure 6.12 shows the DW displacement along the *b*-axis, measured on the former c^+ face versus the grating period.

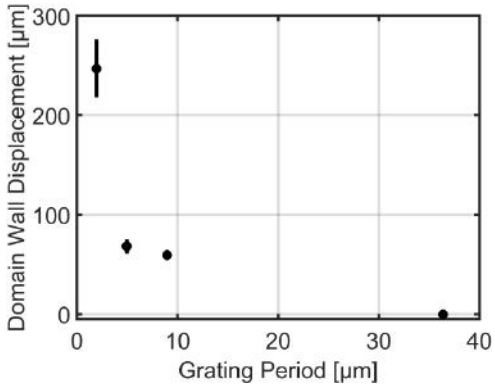

Figure. 6.12. Dependence of the DW displacement along b-axis on the domain-grating period

As can be seen, the DW displacement increases in a highly non-linear manner as the domain size decreases. In the crystal with Λ=36.4 µm we could only observe smoothening of the sharp edges at the domain ends. This is in good agreement with the observations of Masiello et al [9], in which they observed no DW motion in a PPRKTP crystal with similar periodicity below 800 °C. On the other hand, the DW displacement in the samples with Λ= 2 µm were 250 µm on average.

The SARKTP was completely backswitched to single-domain state and is not included in the graph. The amount of domain merging along the *a*-axis was also more severe in samples with short period, in many cases causing individual domains to merge into larger switched or backswitched areas. An example is seen in figure 6.13, showing a domain grating with a 2μm period having merged into a few larger domains.

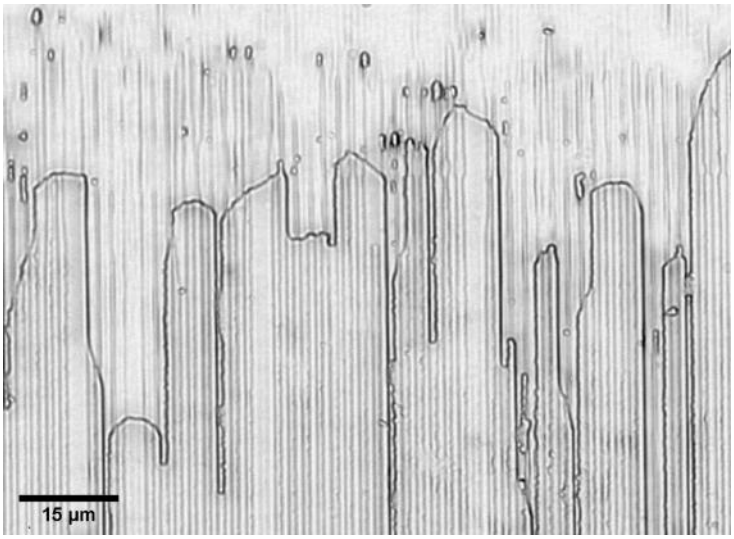

Figure 6.13: Domain merging

The increasing wall mobility with decreasing grating period can be understood by taking into account that narrow domains have a larger ratio of DW area to domain volume [19]. Therefore, these domains have higher E_w, and are less stable and backswitch more. Liu et al [11] observed that in SLT, the degree of backswitching increased when the width of the domains decreased. However, the degree of backswitching could be decreased in the same type of domains if the domains were forming a grating. On the other hand Kan et al [20] observed that in congruent $LiNbO_3$ domains with short inter-domain distance are less stable and found evidence of the existence of repulsive force, most probably originating from bound charges of the lateral DWs. In RKTP, due to the difficulties in fabricating short-period gratings, some DWs deviate from 180° having an angle in the (100) plane, which would give a large E_w. A plausible explanation would be that, with short DW inter-distance, DWs interact with each other. Depending on the amount and type of bound-charges, the interaction will give rise to either merging or backswitching. Nevertheless, further investigation is needed to understand what roles the domain size and the DW inter-distance play.

Edge-Cutting

It is clear that domain wall stability is an issue, even at temperatures a few hundred degrees below the Curie temperature. In order to enable thermal processing of domain gratings at these temperatures, some mechanism for stabilizing the gratings must be found. In SLT, thermally induced back-switching occurs at temperatures far below the Curie temperature. For this material

it was previously shown that the gratings can be stabilized by edge-cutting [14]. In order to test if the same stabilization method can be employed in KTP, a number of samples were cut, parallel to the [100]-plane, using a dicing saw. These edge cut-gratings were then annealed for varying periods of time from 3h to 12h. The result of annealing for 12h is shown in figure 6.14.

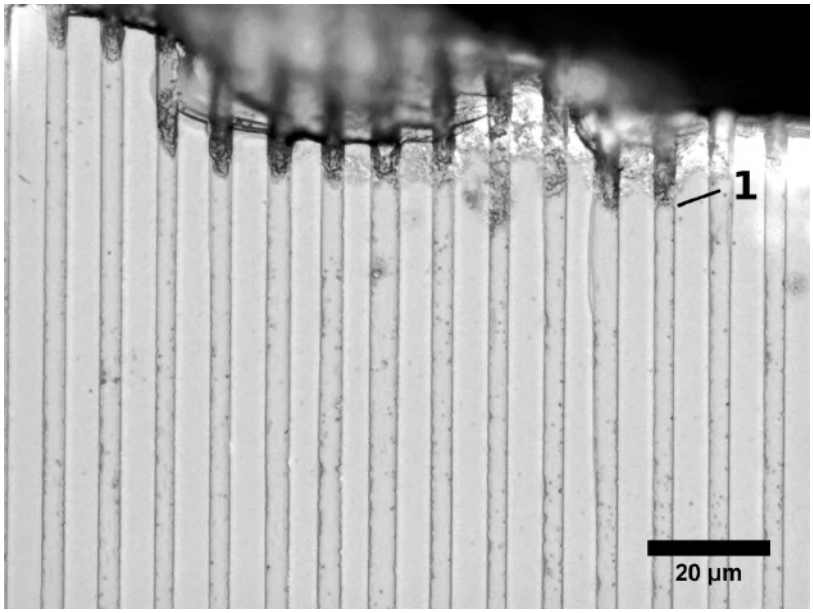

Figure 6.14: Edge-cut grating, annealed for 12 h

In all the gratings tried, the edge-cutting did indeed have a strong effect on the domain wall motion. No motion was observed at the grating edges that had been cut, while those domains that ended before the edges contracted. Due to the limited amount of contraction, the domain wall motion is difficult to appreciate in the image as the initial and final wall positions coincide. However, at some points were the original domain wall was rough, e.g. at the point marked "1" in the image, a smoothening of the wall can be seen, similar to previous observations. Liu et al [14], ascribed the effect of the edge-cutting to a removal of the starting points for domain wall motion. The same logic explains our observations in RKTP; in an edge-cut structure, all domain walls are in the stable [100]-orientation, and therefore very limited motion occurs.

References to Chapter 6

[1] G. Rosenman, Kh. Garb, A. Skliar, M. Oron, D. Eger, and M. Katz, " Domain broadening in quasi-phase-matched nonlinear optical devices", Appl. Phys. Lett. **73**, 865 (1998).

[2] V. Gopalan, Q.X. Jia, and T.E. Mitchell, "In situ video observation of 180° domain kinetics in congruent $LiNbO_3$ crystals," Appl. Phys. Lett., **75**(16) 2482 (1999).

[3] V. Gopalan and T.E. Mitchell, "In situ video observation of 180° domain switching in $LiTaO_3$ by electro-optic imaging microscopy," J. Appl. Phys. **85**, 2304 (1999).

[4] C. Canalias, V. Pasiskevicius, F. Laurell, S. Grilli, and P. Ferraro, "In situ visualization of domain kinetics in flux grown $KTiOPO_4$ by digital holography," J. Appl. Phys. **102,** 064105 (2007).

[5] A. Zukauskas, V. Pasiskevicius, and C. Canalias, "Second-harmonic generation in periodically poled bulk Rb-doped $KTiOPO_4$ below 400 nm at high peak-intensities," Opt. Express **21** (2), 1395 (2013).

[6] R.C. Miller and G. Weinreich, "Mechanism for the Sidewise Motion of 180° Domain Walls in Barium Titanate," Phys. Rev. **117**(6), 1460 (1960).

[7] V. Gopalan, S.S.A. Gerstl, A. Itagi, T.E. Mitchell, Q. X. Jia, T.E. Schlesinger, and D.D. Stancil, "Mobility of 180° domain walls in $LiTaO_3$ measured using real-time electro-optic imaging microscopy," J. Appl. Phys., **86**,1638 (1999) .

[8] C. Canalias, J. Hirohashi, V. Pasiskevicius, and F. Laurell, "Polarization-Switching Characteristics of Flux-Grown $KTiOPO_4$ and $RbTiOPO_4$ at Room Temperature", J. Appl. Phys., **97**, 124105 (2005).

[9] F. Masiello, T. A. Lafford, P. Pernot, J. Baruchel, D. S. Keeble, P. A. Thomas, A. Zukauskas, G. Strömqvist, F. Laurell, and C. Canalias, "Investigation by coherent X-ray section topography of ferroelectric domain behavior as a function of temperature in periodically poled Rb:KTP," J. Appl. Cryst. **44**, 462 (2011).

[10] V. D. Kugel, G. Rosenman, N. Angert, E. Yaschin, and M. Roth, "Domain Inversion in $KTiOPO_4$ Crystal Near the Curie Point", J. Appl. Phys. **76**, 4823 (1994).

[11] X. Liu, K. Kitamura, and K. Terabe, "Thermal Stability of $LiTaO_3$ Domains Engineered by Scanning Force Microscopy", Appl. Phys. Lett. **89**, 142906 (2006).

[12] J. D. Bierlein and F. Ahmed, "Observation and Poling of Ferroelectric Domains in $KTiOPO_4$", Appl. Phys. Lett. **51**, 1322 (1987).

[13] C. Canalias, J. Hirohashi, V. Pasiskevicius, and F. Laurell, “Polarization-Switching Characteristics of Flux-Grown $KTiOPO_4$ and $RbTiOPO_4$ at Room Temperature”, J. Appl. Phys., **97**, 124105 (2005).

[14] X. Liu, K. Kitamura, K. Terabe and S. Takekawa, “Stabilization of Periodically Poled Domain Structures in a Quasiphase-Matching Device Using Near-Stoichiometric $LiTaO_3$", J. Appl. Phys. **102**, 014101 (2007).

[15] X. Y. Liu, K. Kitamura, Y. M. Liu, F. S. Ohuchi, and J. Y. Li, “Thermal-Induced Domain Wall Motion of Tip-Inverted Micro/Nanodomains in Near-Stoichiometric $LiNbO_3$ Crystals”, J. Appl. Phys. **110**, 052009 (2011).

[16] D. Lee, H. Xu, V. Dierolf, V. Gopalan and S. R. Phillpot, “Shape of Ferroelectric Domains in $LiNbO_3$ and $LiTaO_3$ From Defect/Domain-Wall Interactions”, Appl. Phys. Lett **98**, 092903 (2011).

[17] V.Y. Shur, ”Kinetics of Ferroelectric Domains: Application of General Approach to $LiNbO_3$ and $LiTaO_3$", J. Mater. Sci. **41**, 199 (2006).

[18] A. Zukauskas, V. Pasiskevicius, and C. Canalias, “Quasi-periodic Self-assembled sub-micrometer ferroelectric bulk domain gratings in Rb-doped $KTiOPO_4$”, Appl. Phys. Lett. **103**, 252905 (2013).

[19] N. Odagawa and Y. Cho, “Wall Behavior of Nanodomains as a Function of Their Initial State”, Appl. Phys. Lett. **89**, 192906 (2006).

[20] Y. Kan, H. Bo, X. Lu, T. Xu, Y. Jin, X. Wu, F. Huang and J. Zhu, ”Decay Properties of Artificial Two-Domain Structures in $LiNbO_3$ Crystals Studied by Scanning Probe Microscope”, Appl. Phys. Lett. **97**, 202903 (2010).

7. Nanoscale Studies

7.1 Domain Wall Conductivity at Stationary Walls

As mentioned in chapter 4, polarization reversal in the KTP isomorphs is related to ionic motion along the polar axis. Therefore, studying the charge transport properties in these materials is interesting both from a fundamental and a device-optimization perspective. In particular, before the work described here, the charge transport properties of the domains and domain walls in KTP had not been studied on the nanoscale. As discussed in the previous chapters, the DW properties depend to a large extent on the wall angle to the crystal axes. In the first study, the transport properties of stable domain walls, parallel to the energetically favorable [100]-plane were investigated. For these experiments we used KTP crystals with high quality domain gratings. KTP was identified as the most interesting material for these studies due to its higher ionic conductivity; similar experiments on RKTP are expected to give similar results but with poorer signal to noise ratio. The crystals were thinned down to 100 μm in order to maximize the current-signal. Figure 7.1(a) shows the topography of a representative region of one of our samples. The 2-3 nm height difference between opposite domains results from shallow selective etching during the chemo-mechanical surface polishing. The corresponding PFM image is shown in figure 7.1(b). The dark and bright contrasts correspond to P_s pointing out ($P_s\uparrow$) and P_s pointing in ($P_s\downarrow$), respectively. Figure 7.1(c) displays the conductivity map of the same area, obtained with a sample bias of 10 V. A current profile, extracted along the dashed line of figure 7.1(c), is shown in figure 7.1(d).

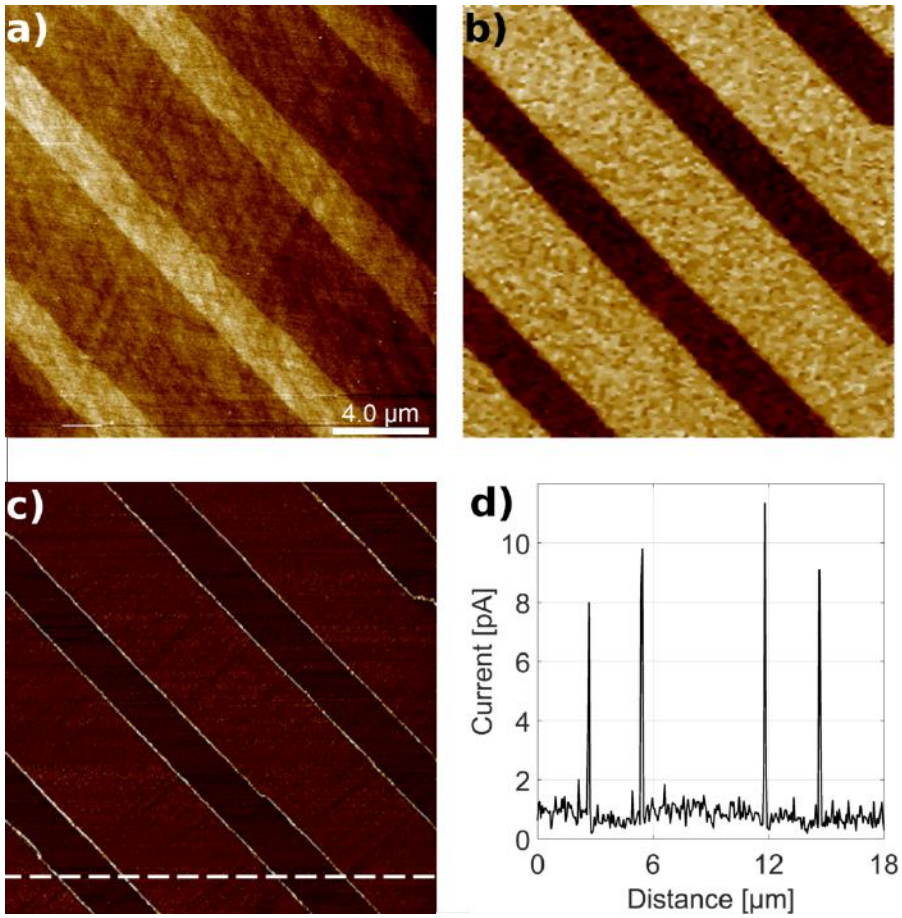

Figure.7.1 AFM-scans of a representative area, (a) Topography, (b) PFM, (c) Current map at 10 V bias, (d) current extracted along the line marked in figure 7.1(c)

The current increases significantly at the DWs, reaching four times the maximum value measured at the domains. This could be attributed to a larger concentration of vacancies around the DW, increasing the ionic mobility, together with the strain fields at the DW surroundings [1, 2]. Note that there is also conductivity contrast between domains of opposite P_s-orientation, the average current at the $P_s\uparrow$ and $P_s\downarrow$ domains being 0.6 pA and 0.9 pA respectively. This contrast is ascribed to a corresponding work function difference between opposite domains [3]. Shvebelman et al [4] attributed this band-gap difference to the selective accumulation of K ions and V_K' in the sub-surface layers near the $P_s\downarrow$ and $P_s\uparrow$ faces, respectively. Scanning with a varying bias reveals the Schottky-like barrier between the AFM-tip and the sample; the conductivity is low for negative bias and an order of magnitude higher for positive bias. An example of such a scan can be seen in figure 7.2. Figure 7.2(a) shows a current-map acquired with varying bias voltage, changing in steps of 2.5 V, from -10 V to +10 V. Figure. 7.2 (b) shows current-profiles extracted from different segments of figure 7.2(a). Figure 7.2 (c) shows the average current at the DWs and domains of opposite orientation as a function of the bias voltage. The current at negative bias is

almost an order of magnitude lower than for positive bias as a result of the Schottky-like barrier between the tip and the sample. Please note that the current-scale of the image is different from the one presented in figure 7.1 in order to accommodate the full range of voltages used, making the current (particularly at $P_s\downarrow$ domains) seem noisier.

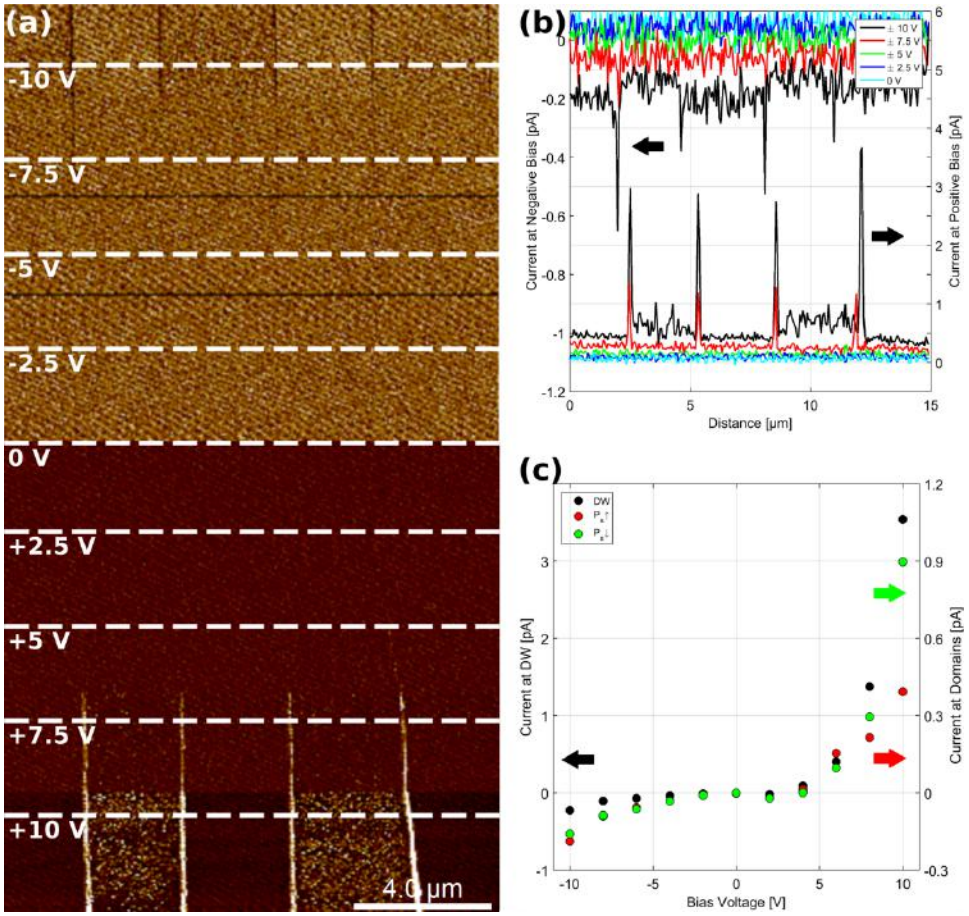

Fig 7.2 (a) Biased scan at varying voltage (-10 V to 10 V in steps of 2.5 V), (b) extracted current-profiles from figure a, (c) extracted average current at DWs and domains as a function of the bias.

In order to further investigate the local conductance of our crystals, current-voltage (IV) curves at different sweep-rates were acquired at the DWs and domains of opposite polarization. Figure 7.3 shows five consecutive IV-curves for (a) DW, (b) $P_s\uparrow$ (c) $P_s\downarrow$ domains. The curves were obtained by ramping the bias from -10 V to +10 V ("forward sweep") and then back from +10 V to -10 V ("backward sweep") at a rate of 1 V/s, while the tip was kept at a fixed position in the sample. The graphs have been compensated for the tip-sample capacitance and the offset-current using the methods suggested by Rommel et al [5]: the offset between the forward- and backward-sweeps was measured at low voltage over the full range of ramp-rates used at DWs and domains. These measurements were used to calculate the capacitance contribution to the current that was

found to be approximately 1 $pAV^{-1}s$, at both domains and at the walls.

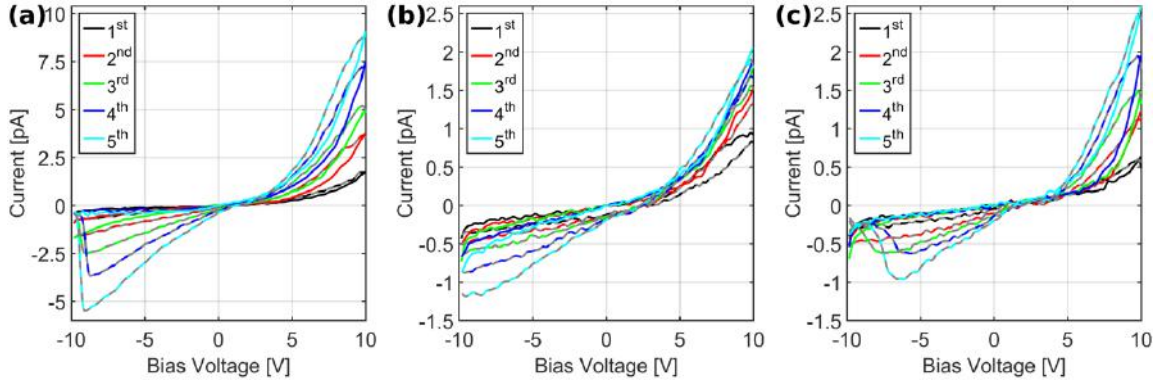

Figure. 7.3. Series of IV-curves acquired with a ramp-rate of 1.0 V/s at (a) DW, (b) P_s↑-domain, (c) P_s↓-domain. The grey dashes mark the backward sweeps.

As previously seen, the conductivity is substantially higher at the DW than at the domains. Both at the DW and the domains, the IV-curves show rectifying behavior for the forward sweeps: the current is very low while the bias is negative and increases exponentially when the bias becomes positive. In the positive branch of the backward sweep, the current is higher at any given voltage than at the corresponding voltage during the forward sweep, giving rise to loop-opening. Moreover, the conductivity shows activation/memristive-like behavior, increasing with the number of IV-curves. Note that at negative bias the current for the backward sweep is higher than in the forward one and also increases with the number of cycles. For P_s↓ and DW the negative current reaches its peak before the bias reaches -10 V, whereas for P_s↑ the peak occurs at -10V. For all three cases the current in the negative direction is mostly present in the backward sweep and after a certain number of cycles. This indicates that it is due to the partial relaxation of charges displaced during the positive bias. In these experiments, P_s↑ shows slightly higher conductivity at +10V for the first cycle than does P_s↓, contrary to what was observed in the biased scan of figure 7.1(c). At the 5th cycle, the current is again higher at P_s↓. This discrepancy could be explained by taking into account that while scanning, the surface-response, related to the energy-gap difference, is the dominating effect. On the other hand, during the IV-curves, the bulk displacement of ions is expected to play a greater role. The selective accumulation of ions and defects at the surfaces has an impact on the work-function at the surface and thus on the local conductivity [3]. As these species move in the applied field, their redistribution may modify the barrier-height, causing the memristive-like behavior and loop-opening. Macroscopic studies in $LiNbO_3$

[6] have previously revealed a similar behavior. Still, effects coming from surface contaminants or related to the quality of the tip-sample contact cannot be entirely ruled out.

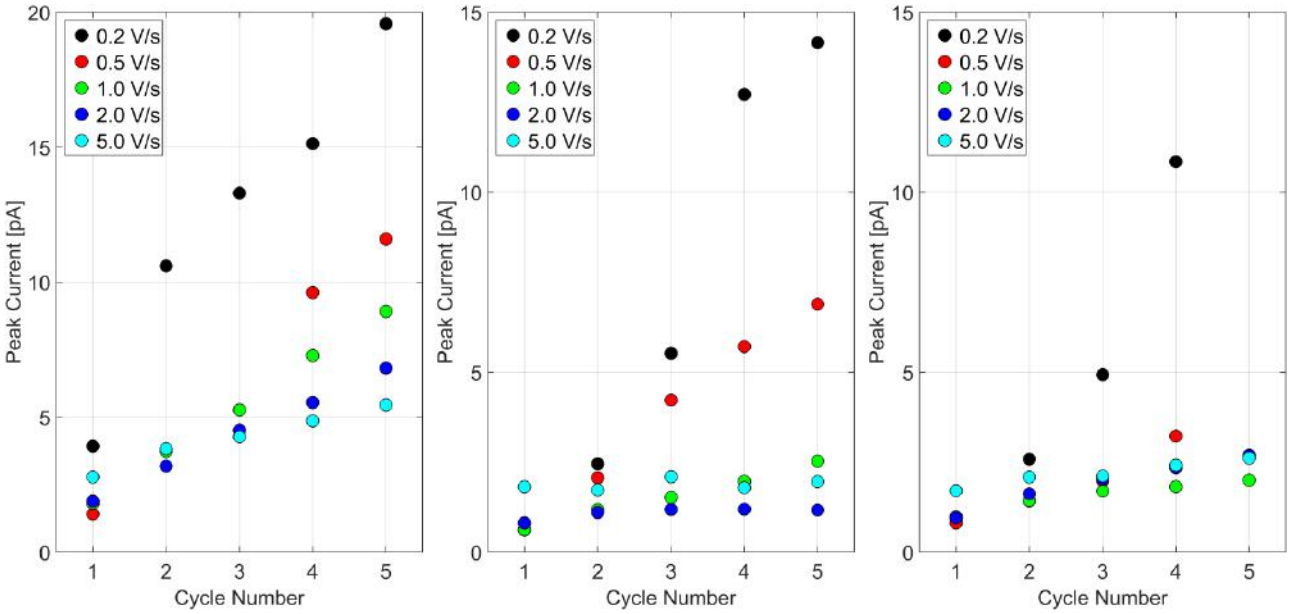

Figure. 7.4: Current at the peak bias versus cycle number for several series of five voltage-cycles each, acquired with varying ramp-rates at (a) DW, (b) $P_s\downarrow$ domains, and (c) $P_s\uparrow$ domains

Figure 7.4 shows the evolution of the current level at +10V for several series of five consecutive IV-curves, each series acquired at a different sweep-rate and in a different position, for (a) DW, (b) $P_s\downarrow$, and (c) $P_s\uparrow$. The fact that the current depends on the sweep-rate clearly indicates that the conductivity is due to ionic movement, as expected for KTP. At the DWs, there is conductivity-activation at all sweep-rates, the final current increases substantially over the series of five cycles. For the domains, the activation-behavior is different: for the fastest ramps (5.0 V/s and 2.0 V/s), there is practically no current increase. For the slower ramps however, there is clear activation: the current increases by 4.5 times at 1.0 V/s and up to 20 times at 0.2 V/s. Note that the current tends to be higher at $P_s\uparrow$ for higher sweep-rates while $P_s\downarrow$ is more conductive for the lower rates. Interestingly, the effects of the activation are visible both in topography and in current maps acquired after a series of IV-curves. For the domains, no changes are visible after the cycles at high sweep-rates, whereas for lower sweep-rates, there are changes to the topography as well as charge accumulation. At the DWs the changes in topography and charge accumulation are observed for all sweep-rates, though the effects are more pronounced for the slower ramps. It is worth noting that both the charge accumulation and topographic changes prevail for at least 30 min after the cycles are acquired, pointing to irreversible surface modifications and charge displacement.

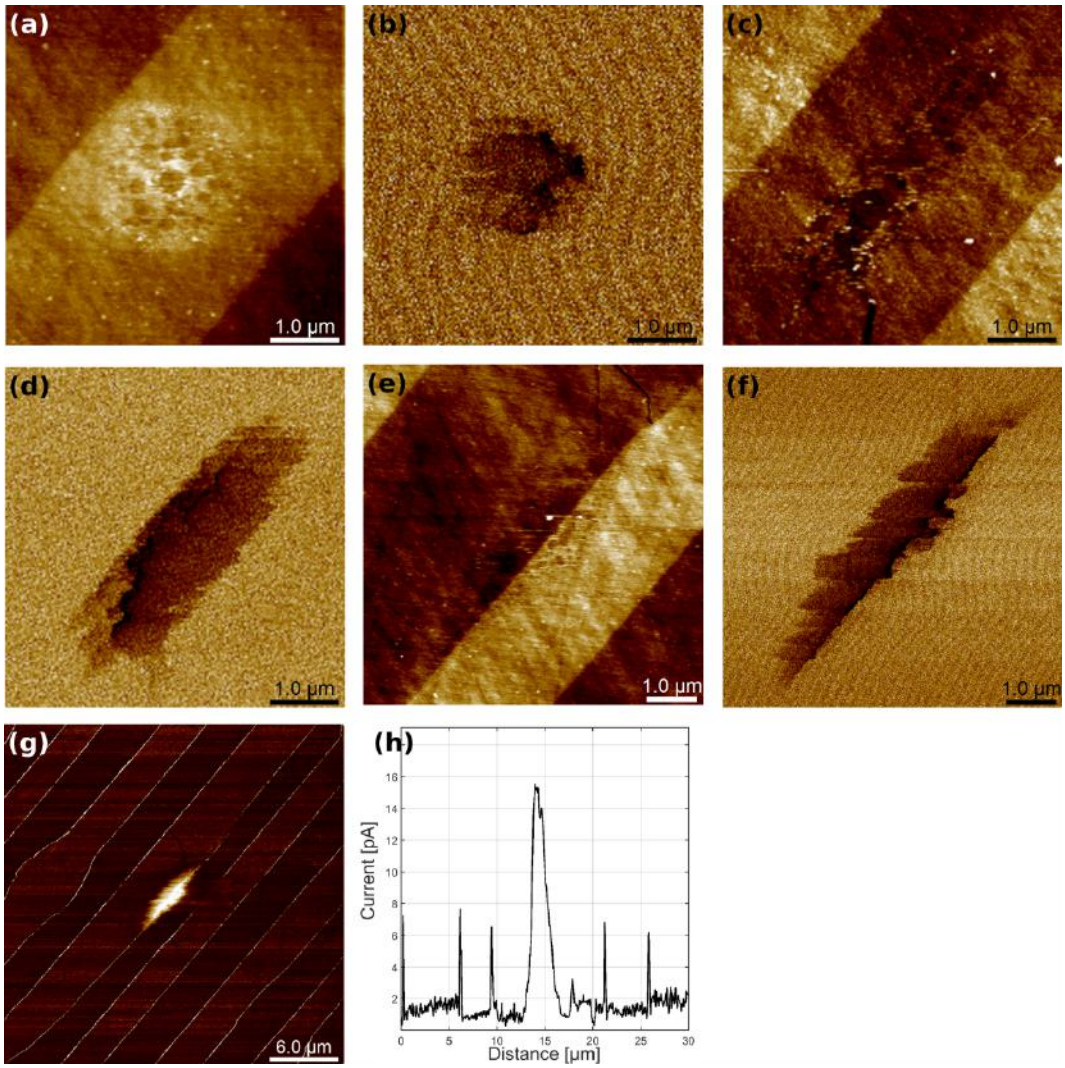

Figure 7.5. (a-f) Topography and current-scans at 0 V bias, acquired after recording IV-curves at (a, b) a P_s↑-domain, (c, d) a P_s↓-domain and (e, f) a DW. (g) current-map at +10 V bias acquired after (f) and (4h) a line extracted at the center of figure (g).

Figure 7.5 shows topographic images as well as current-maps at 0 V bias taken after five cycles at 0.5 V/s sweep-rate for (a, b) P_s↑, (c, d) P_s↓, and (e, f) DW. Here the conductivity images show the charge trapped at the surface that is picked up by the grounded tip. Although the tip was at a fixed point during the IV cycles, the affected area is orders of magnitude larger than the tip radius, extending by a few micrometers in each direction. Remarkably, the topographic changes (and the charge accumulation distribution) are different for the opposite domains, being elongated along the [010]-axis for P_s↓ and circular for P_s↑, both with a roughness of 1-2 nm and current levels of 1-1.5pA. For the DW the changes extend both onto the P_s↑ and the P_s↓ region over a larger area, with detected currents of 2-2.5 pA. The wall and modified region consistently show higher conductivity than the surroundings, as can be clearly seen in the current map of the same

region as in (e-f) at 10V taken afterwards (figure 7.5g) and the corresponding current profile extracted from the center of the scan (figure 7.5h). It should be pointed out that no wall movement could be detected by PFM.

These observations can be understood in the following way: at high sweep-rates, the displacement of ions in the domains is reversible and consequently no displaced charge or topographic changes can be detected afterwards. This translates into similar IV-curves for each cycle. For 1 V/s and lower sweep-rates at the domains, and for all sweep-rates at the DWs, there is conductivity activation and memristive-like behavior which indicates permanent displacement of ions and vacancies, most probably in combination with electrochemical reactions at the tip-sample interface [7]. The greater topography modification and charge-accumulation at the DW, for all the ramp-rates employed, can be understood as a consequence of the local increase in carrier mobility. This increase, together with the high strain and associated electric fields [2], present at the DW can be expected to alter the local electrochemistry at the walls, causing the differences observed. Although further investigation is required to fully understand the difference in morphology between the changes in $P_s\uparrow$ and $P_s\downarrow$ domains, it can be ascribed to the interplay between the different sub-surface layers (i.e., K^+ enrichment at $P_s\downarrow$ and vacancy accumulation at $P_s\uparrow$), the preferential movement of the K^+ in the $P_s\downarrow$ direction [8] and the different reactivity with the water meniscus at the tip-sample interface [7].

7.2 Domain Wall Conductivity at Moving Domain Walls

In order to investigate the conductive characteristics of charged domain walls, not contained in the [100]-plane, a second TUNA-based experiment was performed. The experimental procedure was the same as described in the previous section; this time however, KTP samples containing charged domain walls were selected.

First, we studied a single head-to-head (HH) domain wall. Our as-purchased crystal had several charged walls oriented along the [010]-axis at 4.5° to the [001]-axis. Figure 7.6a displays a PFM-scan on the polar face, showing the initial wall position, and the sketch in the inset illustrates the relative position of the wall and the tip. Figure 7.6b shows a current map of the same location where the applied bias is increased in steps of 1 V from 4 V to 10 V, as indicated in the figure. Between each voltage step, a few lines were scanned with zero bias in order to let the wall relax. As expected from our previous results, there is a conductivity increase at the DW, where the current is around four times higher than in the surrounding domains for all bias values.

Above a threshold of 7 V the current signal at the DW broadens. As the PFM image (figure 7.6c) acquired after the biased scan confirms, the current broadening corresponds to domain wall motion meaning that the current-maps can be seen as stroboscopic images of the wall movement in KTP. Note that the width of the high conductive region correlates well with the amount of DW motion. The motion is always in the direction that lowers the wall angle to the [001]-axis, and gradually increases along the direction of the slow scan-axis within each segment of constant voltage. At 6 V bias, the width of the current remains within noise-level of 60 nm, equivalent to two pixels, with no appreciable DW motion. At 10 V bias the width of the DW-current gradually increases from around 100 nm at the start of the biased segment to 300 nm over a distance of 2 μm along the DW. Note that the width of DW-current corresponds well to the amount of DW displacement, and that although the signal broadens, the current level remains constant for each section of constant voltage.

The gradually increasing DW motion within each voltage segment can be attributed to incomplete relaxation of the wall between 2 subsequent scan lines. During each scan-line the wall becomes unpinned and thus more mobile. If in the subsequent scan-line, the tip reaches the wall before it is fully relaxed, the wall will be more mobile resulting in greater displacement. Furthermore, local wall bending changes the angle of interaction between the scanning tip and the DW. The interaction-time increases since the fast scan-axis will locally be along the wall (as illustrated in the inset of 7.6c). The two effects give rise to a self-enforcing cycle where the displacement in one scan-line causes an even greater displacement in the subsequent one. The interaction-time is also affected by the scan-parameters; in particular the resolution, the scan-size and the scan-rate together determine the effective time that each point is affected by the tip bias. In all the data presented here these parameters have been maintained constant.

We then scanned a different section of the same DW with a constant bias of 10 V and same scan rate and image size as previously. The current-map is shown in figure 7.6d. The wall motion increases gradually along the slow scan axis. However, it saturates after approximately 5 µm, at a displacement of 600 nm. This saturation could be attributed to the maximum wall motion that can be achieved in a single scan with the specific parameters used here for this specific wall.

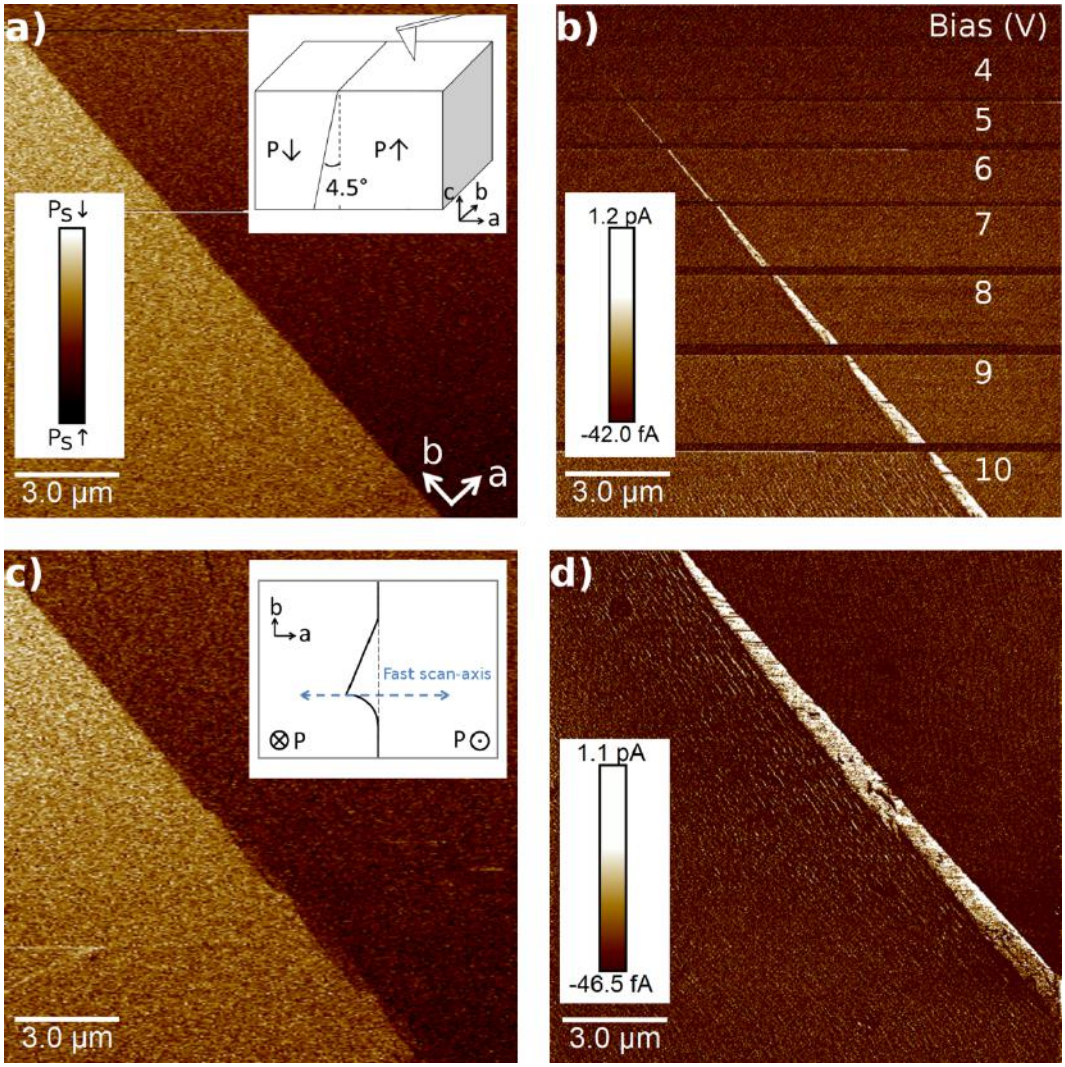

Figure 7.6*: (a) PFM of the initial wall position; the inset shows an illustration of the wall orientation with respect the scanning tip, (b) Biased scan with gradually increasing voltage, (c) PFM of the final wall position; the inset shows the wall motion during scanning. (d) Bias scan at a different DW section with constant bias.*

Next, we studied a domain pattern with charged domain walls with different orientations. The crystal was periodically poled with a 2D electrode with a 6 µm period along both the [100]- and the [010]-axes, similar to what was previously reported in reference [9]. However, for the sample

used here the periodic poling resulted in partial domain-merging, especially along the [010]-axis, presenting a large number of metastable walls. The isolated domain shown in the center of figure 7.7 is the result of three domains on the patterned face merging in the crystal bulk to form a single domain on the non-patterned face as illustrated in figure 7.7(a), with HH walls. In a similar fashion, the two large domains on the sides are the result of more extensive merging of other individual domains, that now present relatively straight walls in the [001] direction . Figure 7.7(b) shows a conductivity-map, obtained at 10 V bias with the tip scanning downwards; figure 7.7(c) shows a subsequent conductivity-map acquired while the tip was scanning in the upwards direction. Figure 7.7(d) shows a PFM-scan acquired after the biased scans showing the total DW displacement. Here the dashed line indicates the initial DW position.

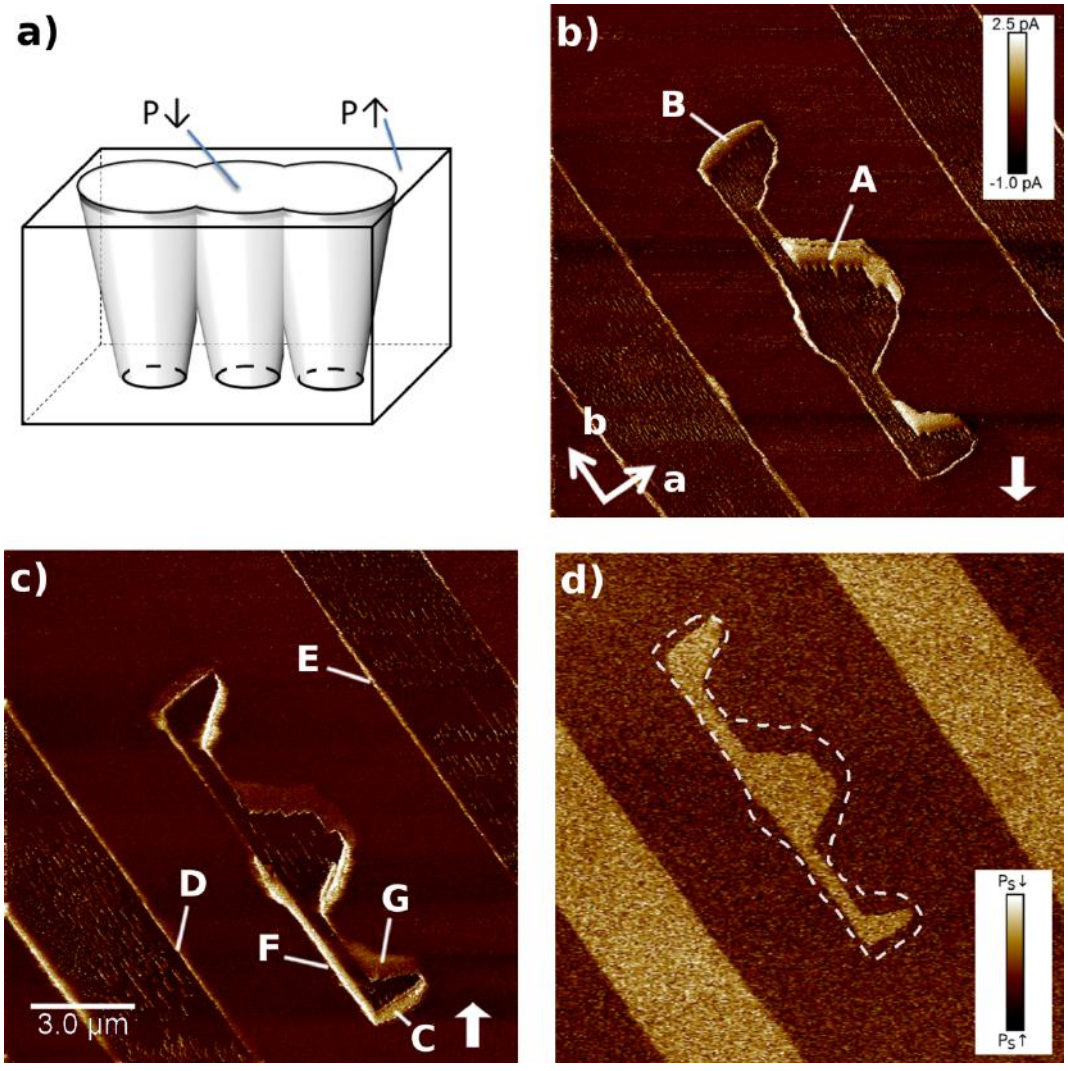

Figure 7.7: (a) Sketch of domain merging corresponding to the central domain in b-d; (b) Current-map at 10 V scanning downwards; (c) Subsequent current-map at 10 V scanning upwards; (d) PFM-scan showing the final domain structure in which the dashes show the original DW position.

As in the previous sample, the current signal broadens at several DW sections indicating wall displacement, as is confirmed in figure 7.7(d). Note however that the motion is not the same for all the DWs: the DWs that have small angles to the [001]-axis (i.e., DWS that are minimally charged) remain still, at least within measurement resolution. This can be clearly seen by on segments D and E that show no movement, except for the protuberance in DW at D that disappears. Note also that the scan-direction has a clear influence on which walls move during a particular scan, as is evident from the motion of the wall segments marked A, B and C in the two pictures: Scanning along their direction of motion makes the walls follow the slow scan axis resulting in large displacement, whereas when the scan is taken in the opposite direction these DWs remain still. Note also that the current levels do not differ much between moving walls and still walls, which indicates that the main contribution and dominant effect to the DWC in KTP is the accumulation ionic mobile species at the DW region, and that DW motion plays a minor role for the DW conductivity.

Note that our technique allows direct visualization of the domain growth steps [10] for the highly mobile walls, clearly visible at segments A and B. These steps appear preferentially aligned along the [010]-direction. This is due to the anisotropic crystal structure of KTP that facilitates domain formation along this direction [11, 12]. This highly mobile DW moves by up to 1μm during a single scan.

In this sense, these current maps can be seen as a stroboscopic image of the DW motion, since it allows tracking their motion using their conductivity. The fact that the high conductivity follows the moving walls differs from what was reported for mobile DWs in BFO, where enhanced conductivity occurred only at the original sites of displaced DWs and was attributed to a combination of defect-accumulation at the initial wall position and polarization-switching-controlled charge-injection.

Instead, in KTP the peak conductivity follows the DW as it moves. However, the wall also induces increased conductivity in the area it traverses (e.g. at point G). This increase could be ascribed to the previously reported conductivity-activation phenomenon, in which a prolonged exposure to a positive bias was shown to increase the conductivity. This was attributed to ionic accumulation at the sample surface which lowers the tunneling barrier. In the present case, the enhanced conductivity at the moving wall can be expected to facilitate the motion of K ions to the sample surface in the area where the DW travels. These ions either follow the DW, and other species are left behind, or just accumulate in the surface. In any case, there will be an accumulation of free carriers at the surface which, in turn, is expected to lower the tunneling barrier, explaining the conductive footprint.

7.3 Elasticity Modulation due to Polarization Reversal and Ionic Motion

It is clear from the previous discussion that ionic motion plays a key role for polarization switching in KTP isomorphs. To gain further insight into the relationship between ion displacement and polarization reversal, a set of experiments were made in collaboration with the Center for Nanophase Materials Sciences (CNMS) at the Oak Ridge Nation Laboratories, USA. The CNMS has a number of highly advanced novel techniques for studying material properties on the nanoscale. In the experiments presented here two such techniques, switching spectroscopy PFM (SS-PFM) using the band-excitation technique, and Time-Of-Flight Scanning Ion Mass-Spectroscopy (TOF-SIMS), explained in detail in chapter 5, were used to study the influence of bias-induced ionic motion on the elastic modulus in KTP and relate it to the domain-selective accumulation of K ions. For these experiments KTP samples with majority [100]-DWs were used and prepared as described in the previous sections.

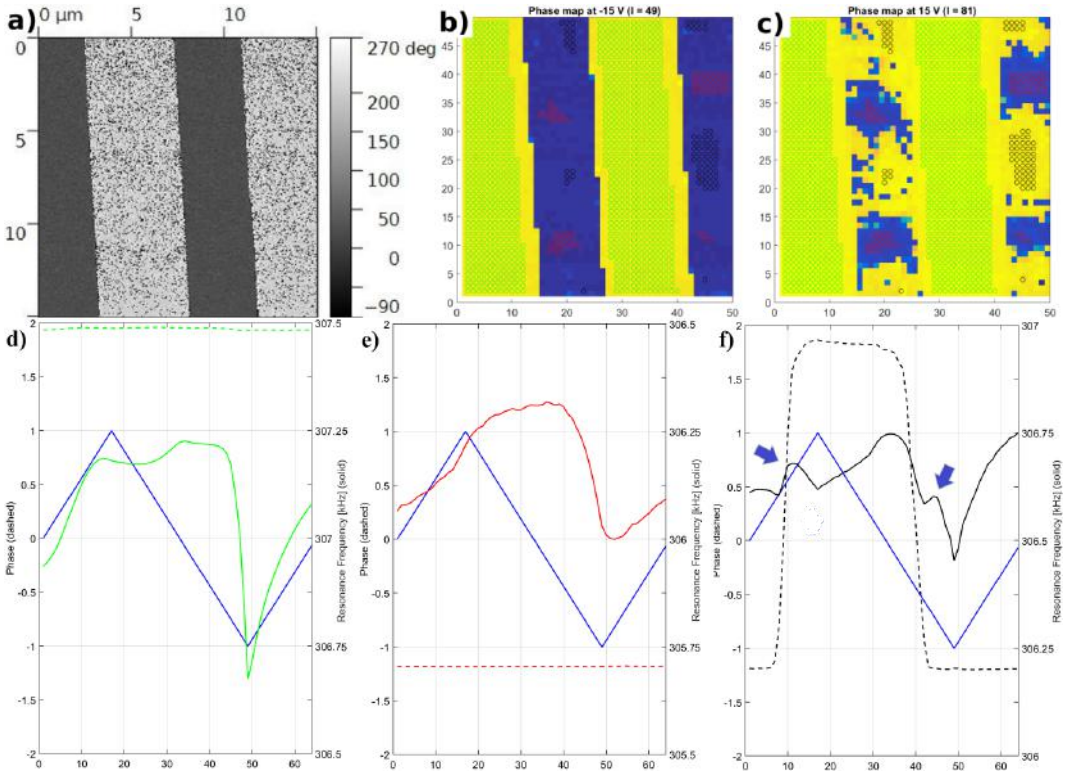

Figure 7.8: (a) PFM-phase of a representative region, (b) SS-PFM phase at peak negative bias, (c) SS-PFM phase at peak positive bias, (d-f), average phase (solid) and resonance frequency (dashed) in the final voltage cycle extracted from the points marked by colored circles at the $P_{s\downarrow}$ domains (d, green), non-switching parts of $P_{s\uparrow}$ (e, red), and switching $P_{s\uparrow}$ (f, black). The bias waveform is shown in all three figures (blue).

Figure 7.8(a) shows the PFM-phase of a representative 15x15 μm^2 region of one of our samples.. The dark and bright contrast corresponds to Ps pointing down ($P_{s\downarrow}$) and Ps pointing up ($P_{s\uparrow}$), respectively. Figures 7.8(b and c) show the SS-PFM phase registered at the peak negative and peak positive bias respectively. On the $P_{s\downarrow}$ domains, the phase remains constant throughout the series of waveforms indicating stable polarization orientation. Contrarily, the $P_{s\uparrow}$ domains can be divided into two areas with different characteristics. As it can be seen in from the phase-maps, some areas of the initial $P_{s\uparrow}$ domains are switched to $P_{s\downarrow}$ orientation at positive applied voltage. The resonance frequency and phase response averaged over the third voltage-cycle as well as the applied bias are shown in figures 7.8(d-f) for the three different areas. The response of the $P_{s\downarrow}$ extracted from the areas marked with green circles in figure 7.8 (b and c) are shown in figure 7.8(d). Similarly, values extracted from the non-switching parts of $P_{s\uparrow}$ (the areas marked by red circles) are shown in figure 7.8 (e); and those of the switching parts marked by black circles are shown in figure 7.8 (f). The resonance frequencies and phases are plotted as solid and dashed lines, respectively, and the bias waveform (in blue) has been added as visual aid. For both domains, the resonance frequency is modulated by the external bias; it increases slowly while the bias is positive and then drops as the bias becomes negative. These resonance frequency-shifts can be attributed to ionic motion in the crystal. The K ions are known to be loosely bound to the titanyl-phosphate structure and therefore can move under the action of external electric filed; as the ions move to and from the surface the ionic distribution changes, causing a local change of the elastic modulus. This leads to the shift of the resonance frequency observed experimentally (figure. 7.8(d-f)).

The resonance-frequency shift varies between different parts of the sample: At the $P_{s\downarrow}$ domains, the total frequency shift is around 550 Hz peak-to-peak; as the bias increases there is a gradual increase of the frequency followed by a plateau as the bias starts declining and then a sudden drop, close to the peak negative bias. In the non-switching $P_{s\uparrow}$ regions, the frequency shift is lower (280 kHz peak-to-peak) and the rate of changes is also lower in both the positive and the negative bias range. In the switching regions intermediate characteristics are observed, both in terms of overall frequency-shift and change–rate. The differences between $P_{s\uparrow}$ and $P_{s\downarrow}$ domains can be attributed to the previously discussed selective accumulation of K^+ ions and V_K^- vacancies at $P_{s\downarrow}$ and $P_{s\uparrow}$ domains respectively.

The K ions are expected to have a higher mobility than the vacancies thus explaining the relatively higher frequency-shifts occurring on $P_{s\downarrow}$. The fact that the frequency increases slowly during the full range of positive bias indicates a gradual accumulation of ions; the subsequent drop, occurring just before the negative bias peak, shows that the accumulated ions suddenly relax and deplete. The fine-structure in the resonance frequency, observed at the points marked

by blue arrows in figure 7.8 (f) coincides with the switching events. They can be understood as a consequence of the ionic redistribution that occurs during polarization-switching; in which the highly coordinated K site changes into the low correlated K site and vice versa[8]. As the crystal structure reconfigures, the titanyl-phosphate network must adapt to these changes and can thus be expected to loosen to allow the motion of the large K ions, temporarily increasing the ionic mobility. The polarization switching occurs only on parts of the original $P_{s\uparrow}$ face, which can be attributed to variations in the nucleation site density across the surface, most likely as a consequence of changes in the local defect-density. However, switching was never observed on the $P_{s\downarrow}$ domains during the experiment in sharp contrast to what is normally seen during switching with macroscopic electrodes. This discrepancy could be attributed to the effect of local screening due to the increased mobility of the K ions at the $P_{s\downarrow}$ domains observed in these measurements. Further investigation will be necessary to fully understand this observation.

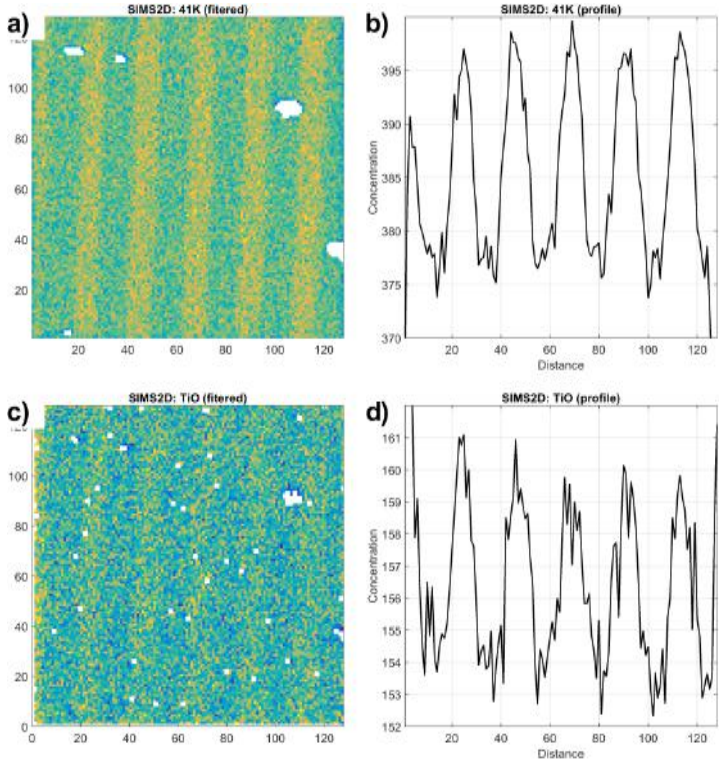

Figure 7.9: (a) K concentration map, (b) concentration profile extracted from (a) through vertical averaging, (c) TiO concentration map, (d) concentration profile extracted from (c)

To confirm the selective accumulation of ions and vacancies, we performed ToF-SIMS measurements on the surface of periodically polled KTP (figure 7.9). In the measurements we used the peak of the $^{41}K^{+}$ isotope to track K^{+} concentration on the sample surface, as original K+ signal was to strong and led to saturation of the mass detector (figure 7.9a,b). We also used the detection of TiO^{+} clusters as a signature of the O^{-} to detect concentration of the oxygen vacancies

(figure 7.9c,d). The white spots in both maps mask contaminated sample regions. ToF-SIMS measurements confirmed inhomogeneity of the K^+ ions and vacancies distribution across the sample surface. Figure 7.9(b) shows a concentration profile, obtained by averaging the concentration map of figure 7.9(a) along the vertical direction. The K^+ concentration was around 5 percent higher inside $P_{s\uparrow}$ domains in comparison with K^+ concentration inside $P_{s\downarrow}$ domains. Figures 7.9d show a similar profile for the concentration of TiO. A somewhat lower selectivity is observed; similarly the TiO^+ concentration was about 2 percent higher in the $P_{s\uparrow}$ domains than in $P_{s\downarrow}$ domains. As shown in the figure, there is indeed a higher concentration of K ions on the $P_{s\downarrow}$ domains, thus explaining the different elastic modulus modification observed for the different domain orientations. The selective accumulation of K/V_K^- is a consequence of the polarization-screening in KTP, known to be mainly due to the highly mobile K ions. The selectivity of the TiO may be attributed to O vacancies that are known to exist in KTP. While they are less mobile than the K ions, their selective distribution indicate that they are also part of the screening process.

In order to further explore the ion-selectivity, the sample was milled with Cs ions and the K+ and TiO+ concentrations were measured at several depths down to a maximum of 28 nm. Subsequently a PFM map was acquired, confirming that the domain structure was not damaged by the milling. The resulting concentrations as a function of the milling depth are shown in figure 7.10.

Figures 7.10 (a and d) show depth profiles of the concentration variation of K and TiO respectively over the full 28 nm milling depth. Figures 7.10 (b and c) show the concentration maps of K acquired at the surface and at the maximum depth respectively. Finally, figures 7.10 (e and f) show the corresponding data for TiO.

The selectivity gradually declines over the depth that was investigated as expected for screening charges, particularly for K that is known to be mobile. However, it should be noted that the selectivity was not completely gone at the maximum depth of 28 nm, in good agreement with previous estimates of the screening depth [4].

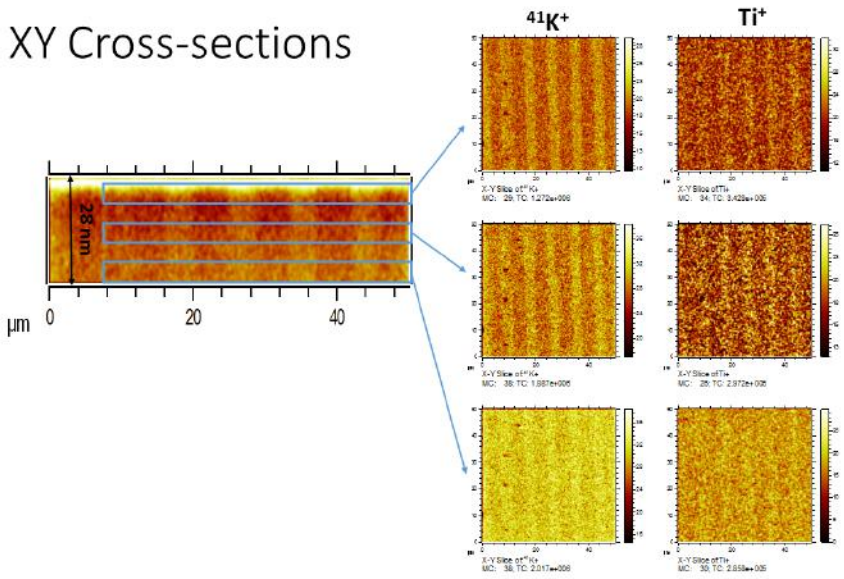

Figure 7.10: (a) Depth profiles of K+ and TiO, and domain-selectivity as a function of depth for (b) TiO, and (c) K^{41}

References to Chapter 7

[1] L. Goncalves-Ferreira, S.A.T. Redfern, E. Artacho, E. Salje, and W. T. Lee, "Trapping of oxygen vacancies in the twin walls of perovskite" Phys. Rev. B, **81**, 024109 (2010).

[2] R. K. Vasudevan, W. Wu, J. R. Guest, A. P. Baddorf, A. N. Morozovska, E. A. Eliseev, N. Balke, V. Nagarajan, P. Maksymovych, and S. V. Kalinin, "Domain Wall Conduction and Polarization-Mediated Transport in Ferroelectrics", Adv. Funct. Mater., **23**, 2592 (2013).

[3] P. W. M. Blom, R. M. Wolf, J. F. M. Cillessen, and M. P. C. M. Krijn, "Ferroelectric Schottky Diode", Phys. Rev. Lett., 73, 2107 (1994).

[4] M. M. Shvebelman, A. G. Agronin, R. P. Urenski, Y. Rosenwaks, and G. I. Rosenman, "Kelvin Probe Force Microscopy of Periodic Ferroelectric Domain Structure in $KTiOPO_4$ Crystals", Nano Lett., **2**, 455 (2002).

[5]M. Rommel, J. D. Jambreck, M. Lemberger, A. J. Bauer, L. Frey, K. Murakami, C. Richter, and P. Weinzierl, "Influence of parasitic capacitances on conductive AFM I-V measurements and approaches for its reduction", J. Vac. Sci. Technol. B., **31**, 01A108 (2013).

[6] H. Li, Y. Xia, B. Xu, H. Guo, J. Yin and Z. Liu, "Memristive behaviors of $LiNbO_3$ ferroelectric diodes", Appl. Phys. Lett., **97**, 012902 (2010).

[7] S. V. Kalinin, S. Jesse, A. Tselev, A. P. Baddorf, and N. Balke, "The Role of Electrochemical Phenomena in Scanning Probe Microscopy of Ferroelectric Thin Films", ACS Nano, **5**, 5683 (2011).

[8] P. A. Thomas and A. M. Glazer, "Potassium titanyl phosphate, KTiOPO4. II. Structural interpretation of twinning, ion exchange and domain inversion", J. Appl. Crystallogr., **24**, 968 (1992).

[9] C. Canalias, M. Nordlöf, V. Pasiskevicius, F. Laurell, "A $KTiOPO_4$ nonlinear photonic crystal for blue second harmonic generation", Appl. Phys. Lett., **94**, 08112 (2009).

[10] C. Miller and G. Weinreich, "Mechanism for the Sidewise Motion of 180° Domain Walls in Barium Titanate", Phys. Rev. **117**, 1460 (1960).

[11] J. D., Bierlein, and F., Ahmed, "Observation and poling of ferroelectric domains in $KTiOPO_4$", Applied Physics Letters **51**, 1322 (1987).

[12] P. Pernot-Rejmankova, P. A. Thomas, P. Cloetens, T. Lyford, and J. Baruchel, "Structural matching of ferroelectric domains and associated distortion in potassium titanyl phosphate crystals," J. Phys.: Condens. Matter **15**, 1613 (2003).

8. Conclusions and Outlook

This work has presented studies on the dynamics, stability, and charge-transport properties of domains and domain walls in KTP and RKTP.

The dynamics of grating-formation in RKTP were studied using online second harmonic generation. It was demonstrated that the temporal evolution of the second harmonic reflects the domain dynamics. Using this technique it was shown that poling with single pulses can result sub-millisecond domain nucleation and growth. The poling quality resulting from triangular pulses was shown to be superior to square pulses.

The high temperature stability of domain walls in RKTP was investigated. By annealing periodic gratings at temperatures over 550° C domain wall motion was induced. The motion is highly anisotropic; along the *b*-axis, the displacement is on the order of several tens of microns, while along the *a*-axis, the result is either orders of magnitude slower motion or complete domain merging, depending on the initial wall configuration. The stability also depends on the period of the grating; complete backswitching was observed for sub-μm periods while in large-period gratings no motion was observed.

The local conductivity of domains and domain walls was studied in KTP, showing a fourfold increase at the domain walls. Memristive-like behavior, with gradually increasing conductivity during repeated voltage-cycling, was observed at domains and domain walls alike. However, the frequency-dependence was markedly different between these two cases: while at the walls the increase was observed for all ramp-rates employed, it was only seen during slow ramps at the domains. The phenomenon is related to topographic changes in the crystal, attributed to ionic motion and accumulation in the sub-surface layers.

It was also shown that charged domain walls in KTP could be displaced by a biased AFM-tip, and that the motion has no influence on their conductivity. Simultaneously acquired current-maps were used as stroboscopic images of the wall, allowing its motion to be tracked. This technique was used to investigate the dynamics of the walls on the nanoscale and its relation to the wall geometry and the relative motion between the tip and the walls.

Finally, by combining band-excitation PFM and time-of-flight ion mass spectrometry, the interplay between ionic redistribution, spontaneous polarization and polarization switching was studied in KTP. By measuring changes in the elastic modulus the ionic motion and polarization switching, induced by an external bias, could be tracked, and related to the polarity-selective accumulation of ions. Together, these results contribute to deepen the understanding of the properties and dynamics of domains and domain walls in KTP.

As shown by investigation of domain formation dynamics, the choice of electric field pulse parameters is of key importance for achieving good results. A promising continuation of this experiment would be to employ a feedback loop from the SH detection to the pulse generator, thus enabling automatic and tailored poling conditions for each individual crystal.

The results obtained on high temperature domain wall stability also provide some guidance for further development. The relationship between periodicity and stability will be of importance for

template growth of high-periodicity structures; to overcome this obstacle, continued research in this field should focus on finding means of engineering increased stability. Here the increased stability of domain walls extending to the sample edge is a potential way forward. However, the limits of this increased stability remain to be tested.

Finally, the presented investigations have only begun to show the interplay between ionic mobility, switching and conductivity enhancement at the domain walls. Further studies could show to what extent the wall conductivity is ionic and electronic and how it depends on the availability of mobile ions and defects, in particular at charged domain walls. This would be of utmost interest for understanding the fundamental mechanisms governing domain formation and enhanced domain wall conduction. Here KTP and its isomorphs are interesting candidates for continued research as they present a unique combination of ferroelectricity and ionic conductivity that can be engineered through doping of the material.

Further research should also focus on the distinct properties of the domain walls. These differ substantially from the crystal bulk, both in the case of charge transport and optical nonlinearity.

A deeper understanding of these characteristics, and how they can be controlled, could allow using them for new applications. It may even be possible to combine the ionic and photonic aspects of domain wall engineering in KTP for applications were both properties are useful such as sensor devices.